POLITECNICO DI MILANO
Facoltà di Ingegneria dei Processi Industriali
Corso di Laurea Magistrale in Ingegneria Nucleare

Wettability control through independent tuning of micro and nano scale features of self-assembled hierarchical material

Relatore:

Prof. C.E. Bottani

Correlatore:

Dott. Fabio Di Fonzo

Tesi di Laurea di:

Giacomo Baldassarre Settimo Bonvini
Matr. 765801

Anno Accademico 2013/2014

Contents

Estratto

Sempre più frequentemente le nanotecnologie vengono impiegate nei più svariati campi della scienza e della tecnica al fine di ottenere materiali funzionali con speciali proprietà. Una di queste è la superidrofobicità, ovvero la capacità di un materiale di repellere totalmente o quasi l'acqua e/o altri liquidi.

Prendendo spunto da molteplici esempi presenti in natura, come la foglia del fiore di Loto, scienziati ed ingegneri si sono accorti che una struttura gerarchica micro e nanometrica unita ad una bassa energia superficiale consentono di ottenere superfici superidrofobiche. Le applicazioni di tali superfici sono svariate, come dimostra il crescente numero di pubblicazioni scientifiche su questo tema. Vetri e vestiti autopulenti, sistemi di microfluidica e sensoristica biomedica e superfici anti-icing sono tra le principali applicazioni in cui tali superfici potrebbero trovare impiego.

La realizzazione delle superfici superidrofobiche oggetto di questa tesi avviene depositando TiO_2 mediante PLD (Deposizione a Laser Pulsato) al fine di ottenere strutture gerarchiche con elevato *roughness factor* e *surface ratio*. Il substrato prodotto, di per sé superidrofilico a causa dell'elevata energia superficiale, viene quindi sensitizzato immergendolo in una soluzione di acido perfluorononanoico in etanolo. A seconda della pressione di deposizione, dello spessore del film nanostrutturato, della concentrazione molare della soluzione e del tempo di immersione dei campioni, le morfologie (e quindi le performance) che si ottengono sono diverse.

La presente tesi mira ad ottenere il controllo del processo di fabbricazione, individuando i parametri che governano il comportamento delle superfici. Al fine di valutare la dipendenza delle proprietà superidrofobiche dalle caratteristiche strutturali e morfologiche delle superfici, è stata effettuata una caratterizzazione comprensiva di misure di angolo di contatto statico e dinamico e analisi morfologiche mediante immagini SEM e AFM e analisi XRD. Allo scopo di determinare anche le proprietà ottiche sono state effettuate anche analisi tramite spettrometria UV-Vis.

Abstract

Increasingly more frequently nanotechnologies are employed in several fields of science and technology in order to fabricate functional materials with specific properties. Superhydrophobicity is one of these properties: it is the capacity that a material has to repel water or other liquids completely or almost completely.

If we look at the numerous examples present in nature, such as the lotus leaf, scientists and engineers have realized that a hierarchic micro and nanometric structure together with a low surface energy allow obtaining superhydrophoic surfaces. Applications of such surfaces are several, as shown by the increasing number of scientific publication about this issue. Self-cleaning glasses and clothes, microfluidic systems and anti-icing surfaces are among the main applications where such surfaces could be employed.

Superhydrophobic surfaces considered in this thesis work are fabricated by Pulsed Laser Deposition (PLD) of TiO_2 in order to obtain hierarchic structures with high roughness factor and surface ratio. The substrate so produced, intrinsically superhydrofilic due to its high surface energy, is sensitised by being immersed in a solution of perfluorononanoic acid. According to the deposition pressure, the thickness of the nanostructured film, the molar concentration of the solution and the immersion time of the models, morphologies (and, consequently, performances) that can be obtain are different.

The present thesis aims to take control of the fabrication process, by determining the parameters that govern the behaviour of the surfaces. In order to estimate the dependence of superhydrophobic properties on structural and morphological characteristics of the surfaces have been performed surfaces analysis by means of SEM and AFM images and XRD spectra. Moreover, analyses through UV-Vis spectroscopy have been carried out to determine optical properties.

Chapter 1

Theoretical Background

1.1 Introduction

Many surfaces in nature are superhydrophobic. Several of these natural surfaces, including various plant leafs, bird feathers , and legs of water strider , have been investigated with remarkable attention. It has been discovered that water droplets on hydrophobic surfaces can exhibit a contact angle higher than 90°. More precisely, when contact angle is greater than 150° the surface is said superhydrophobic [1],[2]. In the case of lotus leaf, for example, contact angle's values higher than 160° has been observed. A drop of water deposited on such a surface adopts the shape of a nearly perfect sphere that rolls off easily, leaving no trace of humidity behind. This property turns into the possibility of create self-cleaning, anti-corrosion and anti-icing solid surface. Clearly, they could have wide applicability in several fields of science and engineering [3]. For example they could be used in such a system where icing is a critical problem, like airplanes, ships or refrigerators [4],[5]. Superhydrophobicity is achieved by the combination of two parameters: an intrinsic hydrophobicity of the material (wax and plastics are examples of hydrophobic materials) and surface roughness, or micro texture. Several works have also shown the importance of multi-scale roughness in achieving superhydrophobicity.

shows three examples of superhydrophobic surfaces, at micro-scale, from vegetable world: *lotus leaf*[6] *, taro leaf* and *india canna leaf* [7]. As is shown all the surfaces are covered with nano-sized objects like pillars or rods. A water drop that is deposited on such a rough hydrophobic surface, rests on the crests of the texture, thereby entrapping air underneath, leading to a composite liquid-substrate interface that consists partially of solid-liquid interfaces and

partially of liquid-gas. This promotes a spherical drop shape with a large contact angle and the wetting regime is heterogeneous, as it can be seen in Figure 1.2(a). Next to this superhydrophobic state, a drop on a superhydrophobic surface is known to exist also in an impregnated state (or homogeneous), with liquid penetrating into the grooves caused by the protrusions as illustrated in Figure 1.2(b). The starting point of wetting model is defined by Young's contact angle equation while superhydrophobic state and impregnated state are defined respectively by Wenzel and Cassie-Baxter models. Before focusing on these models, it is useful introduce preliminary concepts of Young's contact angle, surface tension and surface free energy.

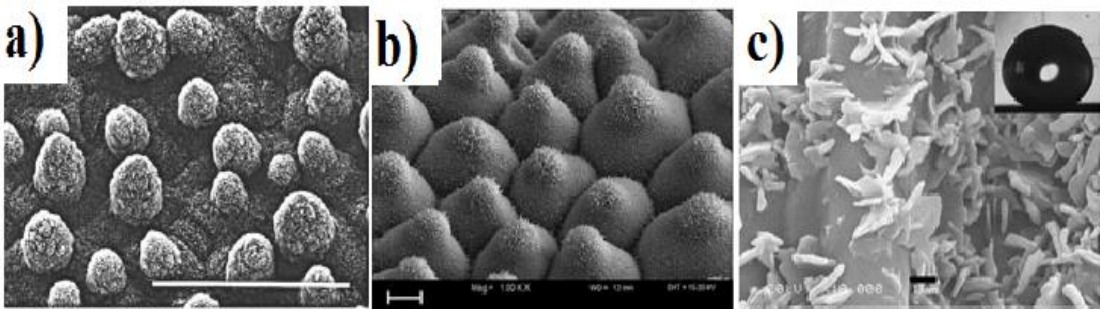

Figure 1.1 *a) Lotus leaf*[6] *. b) Taro leaf and c)India canna leaf* [7].

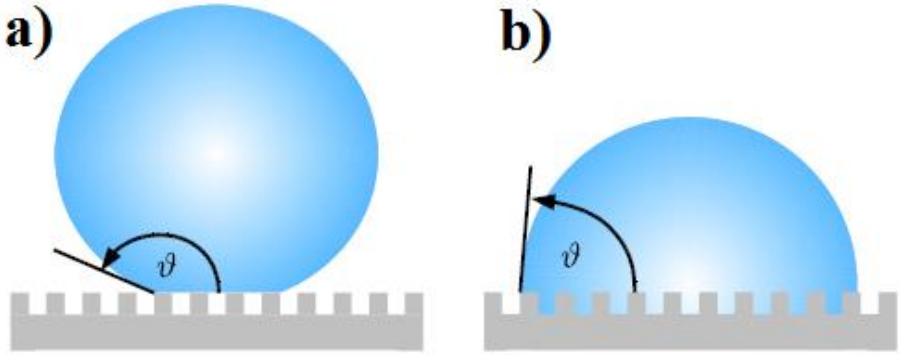

Figure 1.2 *(a) Heterogeneous state (b) Homogeneous state*

1.2 Wettability

1.2.1 Surface Tension and Surface Free Energy

In contrast to a gas, liquid is condensed matter. Therefore, liquid bulk molecules will experience forces, known as chemical bonds, equally isotropically. In contrast, at the surface each molecule misses half of its neighbors, thus it misses half of its bonds. To bring a molecule near the surface, an amount of energy approximately equal to half its binding energy is required. This additional energy caused by the higher energy is called surface tension, denoted by σ, and with the dimensions of energy per area units, that is, in the SI system, J/m^2 . Thermodynamically, the concepts of surface tension and surface free energy are different [8]. Surface tension represents the energy (per unit area) required to create new liquid surface while surface free energy takes into account the breakage of intermolecular bonds that occurs when a surface is created. However, when temperature and pressure are assumed constant, the two concepts are numerically equivalent to each other. Actually it is necessary also to assume that there is no adsorption at the interfaces as well. Moreover, since liquid will seek to minimize its surface area, any curved surface will tend to flatten. This results in an inwards oriented force. Considering a spherical, with radius R, we can write this force in terms of pressure [8]:

$$P = \frac{F}{S} = \frac{4\pi R\sigma}{4\pi R^2} = \frac{2\sigma}{R} \tag{1.1}$$

Thus, the surface tension results in an additional pressure inside the liquid, or more precisely, if we cross the curved interface from outward to inwards, the pressure increases by 2σ/R.

1.2.2 Young's Contact Angle

A sessile drop on an ideal rigid, homogeneous, flat and inert surface are considered. In this case, wetting mode is described by Young's Equation 1.2 [9]

$$\cos\vartheta = \frac{\sigma_{sg} - \sigma_{sl}}{\sigma_{lg}} \tag{1.2}$$

When drop contacts solid surface, three interfaces can be identified: liquid-solid, liquid-gas, gas-solid, as is shown in Figure 1.3.

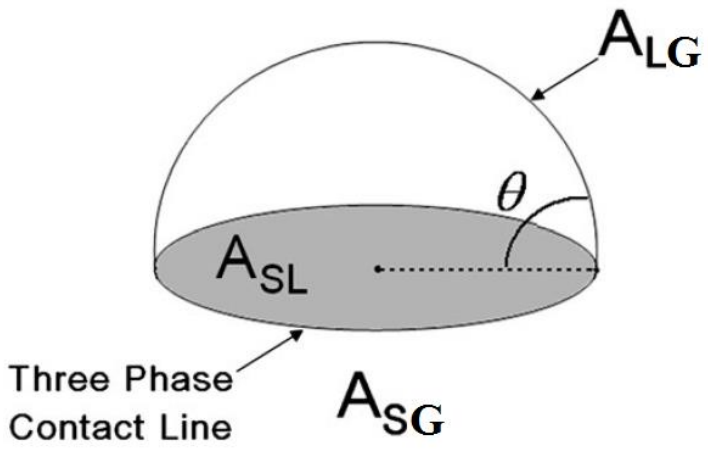

Figure 1.3 *A liquid drop showing contact angle è balanced by three interfaces.*

Each contact line is drawn by interface in order to minimize the corresponding surface area, balancing the surface tensions on the direction of potential motion so that there will yield a relation attributed to Young, as shown in Equation 1.2 where σ indicates surface tension and ϑ the contact angle, which is the angle where a liquid/gas interface meets a solid surface. In many cases it happens that the surface energy of the solid substrate, σ_{sg}, is rather high, as in many metals, while the surface energy of the liquid, σ_{lg}, is comparably low, as in most organic liquids. Moreover, since in many occasions σ_{sg} much higher than σ_{sl}, the right-hand-side of Young's equation would be larger than 1. This case is known as *total wetting* (sometimes expressed as 'the contact angle is zero'), and corresponds to the case when the surface energy of a dry substrate is larger than the total surface energy of a substrate covered with liquid, which comprises both a solid-liquid and a liquid-gas interface. In this case the liquid spreads completely over the substrate. Otherwise, if contact angle is sufficiently high, a deposited drop will not spread over the surface, rather it will arrest and adopt the shape of a spherical cap with Young's angle at its contact line.

1.2.3 Wenzel Model

Real surfaces usually are not smooth, they rather exhibit roughness. Therefore, Young equation [1] cannot explain the behaviour of real surfaces, which do not exhibit a regular profile. Wenzel then proposed an equation relating the contact angle to surface roughness and surface energies. It can be written as [10]:

$$r(\sigma_{sg} - \sigma_{sl}) = \sigma_{lg} \cos \vartheta^*_w \tag{1.3}$$

where θ^*_w is the apparent Wenzel contact angle, which represents the apparent contact angle affected by the roughness of solid surfaces. r corresponds to the "roughness factor", which is defined as the roughness area ratio of the actual surface with respect to the geometric surface (Figure 1.4).

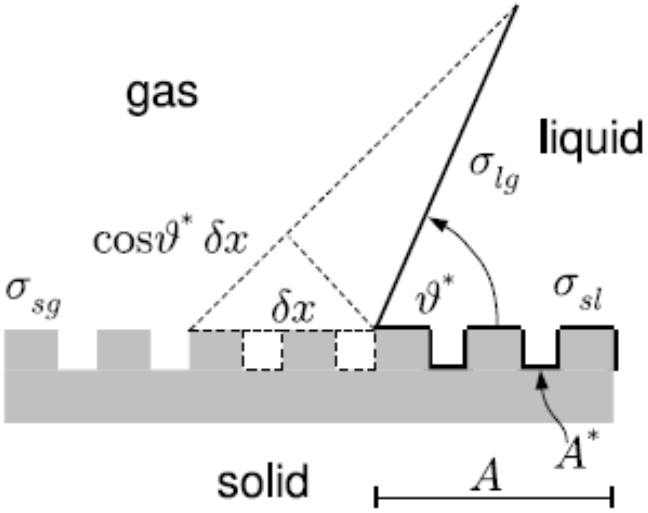

Figure 1.4 *The Wenzel model. The roughness r of a surface is defined as the ratio of the actual surface area A* over the apparent macroscopic surface area A*

Normally Wenzel equation is written as:

$$\cos \vartheta^*_w = r \cos \vartheta \tag{1.4}$$

where θ is the Young's angle. angle. Wenzel's relation predicts two types of behavior. If the surface is *hydrophilic* (θ< 90), the apparent contact angle is further decreased. In contrast, if the surface is *hydrophobic* (θ>90), the contact angle is increased. Therefore, the Wenzel equation states that the wettability can be improved by the surface roughness for a hydrophilic surface, but might get

worse for a hydrophobic one. Moreover, the Wenzel equation assumes the water will penetrate into the grooves caused by the surface roughness, and therefore the Wenzel. equation is related to the homogeneous wetting regime.

1.2.4 Cassie-Baxter Model

While the Wenzel equation is applicable to the homogeneous wetting regime, the Cassie–Baxter equation [11] corresponds to the heterogeneous wetting regime. This model postulates that the superhydrophobic nature of a rough surface is caused by microscopic pockets of air entrapped below the liquid droplet leading to a composite surface that consists partially of solid-liquid interfaces and partially of liquid-gas interfaces. In the heterogeneous state, the liquid only contacts the solid at the top of the protrusions on a fraction denoted as ϕ_s, which is the ratio of the total area of the solid–liquid interface with respect to the total area of solid–liquid and liquid–air interfaces in a plane geometrical area of unity parallel to the rough surface, as it can be seen in Figure 1.5.

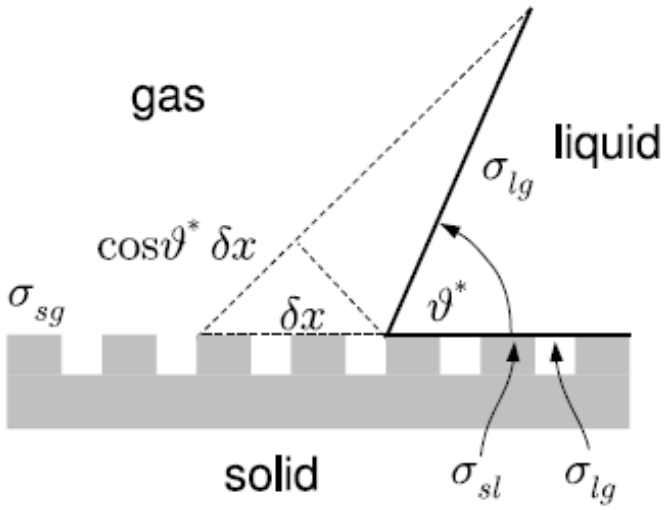

Figure 1.5 *The Cassie-Baxter model. The liquid is assumed to 'float' on top of the texture forming microscopic air pockets, leading to a composite surface that consist partially of solid-liquid interfaces, and partially of gas-liquid interfaces.*

The contact angle θ* of a “fakir” drop [12], [13]is caused by both the solid and the air, so it can be written:

$$\cos\vartheta^* = -1 + \phi^s(1 + \cos\vartheta) \tag{1.5}$$

Equation 1.5 can be modified considering the ratio of the actual wetted area to the projected area, r_f. This give will rise to the following form:

$$\cos\vartheta^*_{CB} = -1 + \phi^s + r_f\phi_s\cos\vartheta \tag{1.6}$$

In contrast to the Wenzel relation, the Cassie-Baxter equation allows for the possibility of θ*>90 with θ<90.

1.2.5 Hysteresis Contact Angle

To describe a superhydrophobic state the static contact angle as well as the hysteresis contact angle (CAH) [14],[5],[15], should be measured. CAH can be explained in two manner. Firstly, as shown in Figure 1.6(a) liquid drop is considered. Its volume can be increased adding water on the surface. In this case an advancing contact angle θ_A can be measured. Vice versa withdrawing water from a droplet on a surface, decreasing its volume, a receding contact angle θ_R smaller than θ_A is obtained. The second manner consists of considering a liquid droplet on a tilted surface, as in Figure 1.6(b).

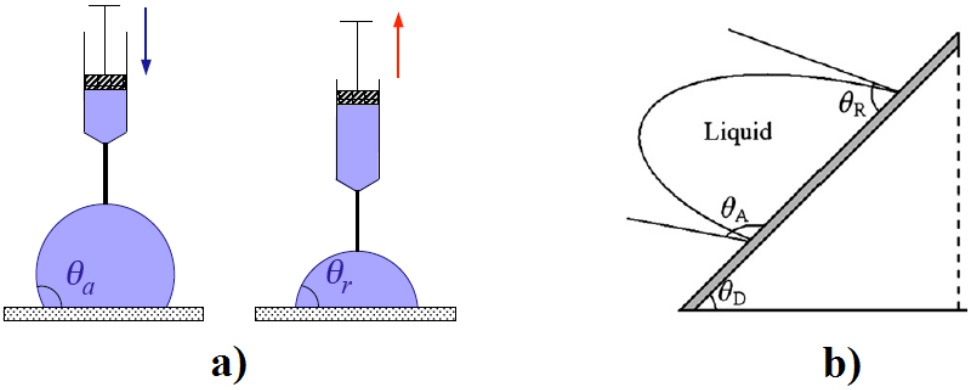

Figure 1.6 *a)An increasing volume of liquid with θ_A and a decreasing volume of liquid with θ_R: angle are different b)A liquid drop theoretically sliding on a declination of θ_D without acceleration. θ_A is the advancing angle, and θ_R is the receding angle.*

The liquid drop will advance at the lower side and recede at the upper side when the substrate is inclined at θ_D, which is the sliding angle. In order to let the liquid droplet slide off, the substrate must be tilted at/over the sliding angle. Here, the

liquid wets the substrate at the advancing point and dewets it at the receding point. Also in this case advancing contact angle is bigger than receding contact angle. This fact can be explained considering that the drop motion is given by an external force, for example internal pressure (Figure 1.6(a)) or gravity (Figure 1.6(b)) that pushes the drop itself to advance or recede. Due to this external force a strength state is established across the drop and this brings to a deformation and then different values for advancing and receding contact angles. The difference between advancing and receding contact angles is termed as the hysteresis contact angle CAH and it should be as small as possible. Indeed in this case a very stable superhydrophobic surface can be kept while sufficiently high CAH might lead to a change in wetting state. Moreover low hysteresis, means low liquid adhesion on the surface, which is one of the most important requirement in self-cleaning glass fabrication. Finally, hysteresis contact angle is of paramount importance in anti-icing devices fabrication. In fact, high hysteresis bring to high probability of liquid pinning and ice nucleation [5], [16], [17].

1.2.6 Competition between Wenzel and Cassie-Baxter Models

Depending on the wetting state, a drop exhibits different behaviors. In heterogeneous state, where the drop rests on top the texture like a fakir on his bed, the drop has very high mobility and it can easily roll off the surface. This leads to self-cleaning and liquid repellency. On the contrary, in homogeneous state the drop has low mobility, it is impregnated in the texture and so, it cannot easily roll off. Unfortunately whether or not the liquid droplet rests partially on the solid surface as well as the air respectively is still under investigation. Various thermodynamic arguments have been suggested to determine whether a drop on a superhydrophobic surface resides in the superhydrophobic or in the impregnated state [18]. Frequently the total surface energies of both states are compared [12],[19],[18] suggesting a critical Young angle whose cosine is defined by the following equation:

$$\cos \vartheta_c = -\frac{1-\phi^s}{r-\phi^s} \tag{1.7}$$

The impregnated state is established if ϑ<ϑc, whereas the superhydrophobic state is adopted if ϑ>ϑc. Because r>1> S, the critical Young angle is necessarily greater than 90.

Alternative arguments [20][21][22]recognize the metastability of the superhydrophobic state. For an irreversible transition from superhydrophobic state to an impregnated state two scenarios are possible, as shown in Figure 1.7. In *touchdown* scenario [12] (Figure 1.7(a)) liquid-gas interfaces collapse when they touch the texture. The touchdown condition depends on the particular geometry of the surface profile. For rectangular grooves of width *w* and depth *h*, touchdown is expected at a pressure drop ΔP over the interface expressed as

$$\boldsymbol{\Delta P} = \frac{2\sigma h}{h^2+\left(\frac{w}{2}\right)^2} \tag{1.8}$$

Sufficiently deep grooves prevent touch down at the floor of the texture. In such a case, collapse of the superhydrophobic state due to depinning of the microscopic contact lines was suggested.

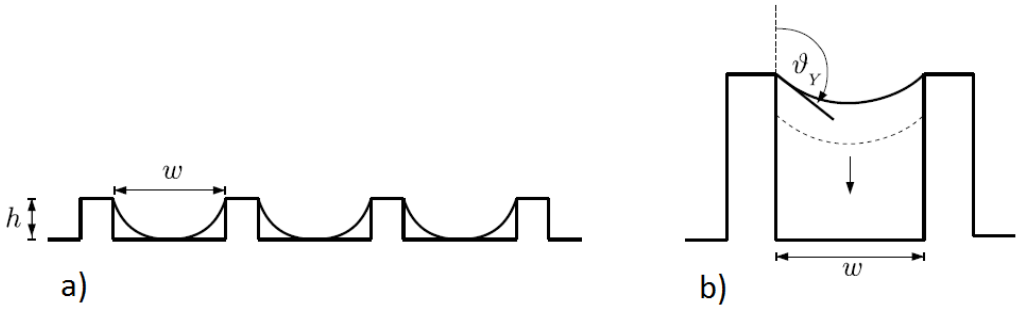

Figure 1.7 *a) Touchdown scenario. The liquid-gas interfaces are assumed to collapses when they touch the oor of the texture. b) Depinning scenario.The interfaces are assumed to depin when their angle with respect to the vertical wall exceeds Young's angle.*

In Figure 1.7(b) is schematized another possibility, the so called *depinning* scenario [12] . Here it si assumed that the contact angle at the sharp edges of the texture is limited by Young's angle. It is also postulated that the liquid -gas interfaces can adopt any angle larger than the Young angle with respect to the horizontal surface and smaller than the Young angle with respect to the vertical walls of the texture. In case of rectangular grooves, the collapse condition yields a critical pressure drop across the liquid-gas interface, this leads to the following equation:

$$\boldsymbol{\Delta P} = \frac{2\sigma \cos \vartheta}{\frac{w}{2}} \tag{1.9}$$

The competing models highlight the difficulties in evaluating a condition for the transition between the superhydrophobic and the impregnated state, or more generally, in describing which state a drop will adopt on a given superhydrophobic surfaces. Besides, experimental studies of the microscopic features of superhydrophobic surfaces have remained elusive.

1.3 Materials and techniques to produce superhydrophobic surfaces and coatings

Inspired by lotus leaf and other natural examples, researchers and companies around the world started working for developing technologies to produce surfaces with extremely low surface energies and also to control the morphology of the surface on a micro and nanometric scale. This idea of controlling surface micro and nano-structure opens up many possibilities for developing a variety of engineered surfaces. Techniques to produce superhydrophobic surfaces can be broadly classified into two categories: In the first a surface of low energy material is made rough while the second category consists of modifying a rough surface with a material of low surface energy.

1.3.1 Roughening the surface of low surface energy material

1.3.1.1 *Silicones.* Polydimethylsiloxane (PDMS) belongs to a group of organosilicon compounds, commonly known as silicones. Its viscoelastic behavior and hydrophobic properties makes it highly suitable for producing superhydrophobic surfaces. Various methods are practised to produce superhydrophobic surfaces using PDMS. For example it can be used a CO_2 laser or electrospinning technique[23]. CO_2 laser acts as an excitation source to introduce peroxide groups onto the PDMS surface. These peroxides are capable of initiating graft polymerization of 2-hydroxyethyl methacrylate (HEMA) onto the PDMS (Figure 1.8(b)). In Figure 1.8(a) it is shown a PDMS surface treated with a CO_2 pulsed laser.

Also electrospinning technique can be used to produce superhydrophobic membranes [24]. High voltage is used to create an electrically charged jet of polymer solution or melt, which dries or solidifies to leave a polymer fiber, as is shown in Figure 1.9(a). Electrospun fibers made of a PS-PDMS block blended with a PS (polystyrene) homopolymer reached high contact angles. The large contact angle is because of the combined effect of enrichement of the fiber surfaces by the PDMS component and the surface roughness due to the small diameter of the fibers (150–400 nm). In Figure 1.9(b) it can be seen a PS-PDMS/PS electrospun fiber mat and the droplets on it.

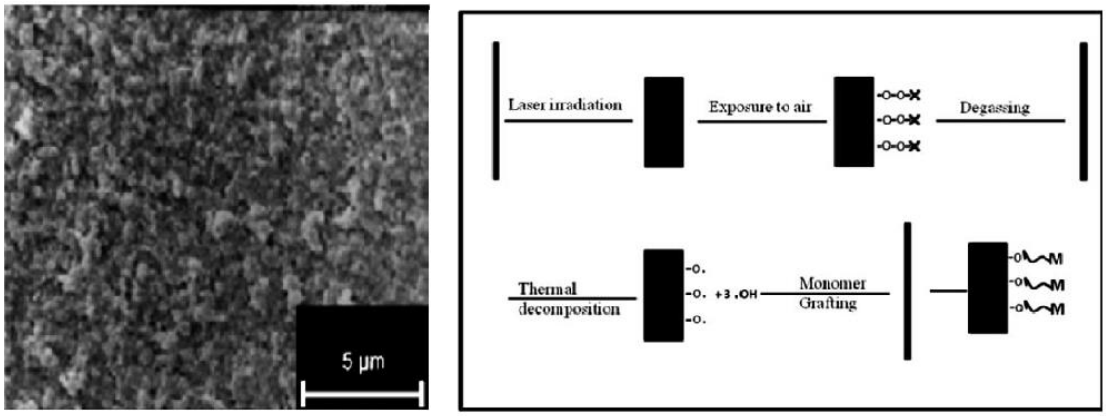

Figure 1.8 *a)A SEM image of a PDMS surface treated with a CO_2 pulsed laser*[23] *. (b) A schematic illustration of laser induced graft polymerization.*

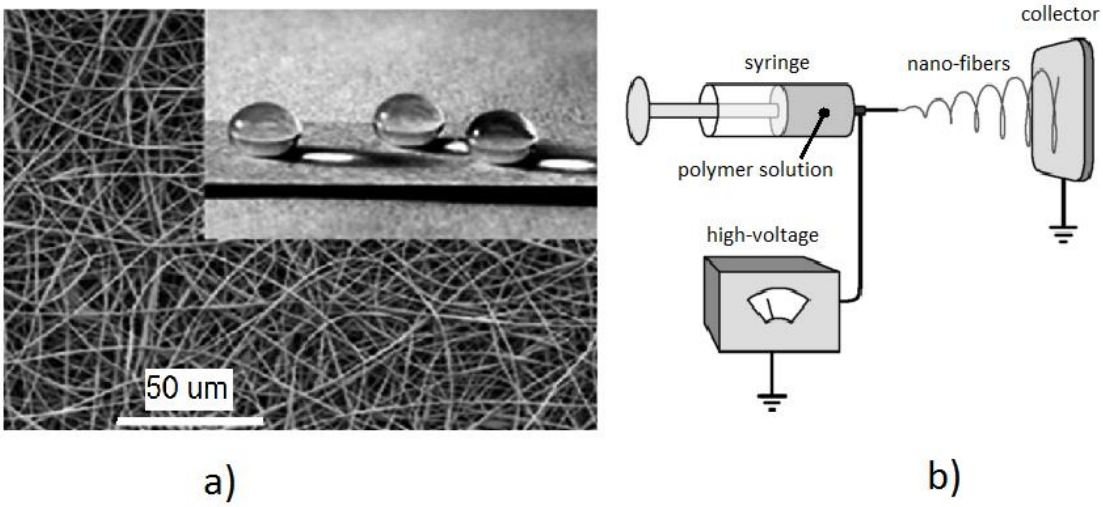

Figure 1.9 *a) A SEM image of a PS-PDMS/PS electrospun fiber*[25] *mat and the droplets on it. b) Schematic of the electrospinning setup*[25].

1.3.1.2 *Fluorocarbons.* Fluorinated polymers are attracting lots of interest these days because of their extremely low surface energies. Roughening these polymers will result in superhydrophobic surfaces. One of the most used polymer is Teflon (polytetrafluoroethylene) [26], whose superhydrophobic properties are primarily due to the high electronegativity of fluorine and, London dispersion forces of low intensity which characterize the fluorocarbons

themselves. In addition hydrophobicity is enhanced by the presence of fibrous crystals with large fractions of void space on the surface. Another way to produce a superhydrophobic surface with polymers consists of casting a polymer solution under humid conditions [26](Figure 1.10(a)). In this process, the fluorinated glass substrate was placed over the substrate holder. A metal blade was fixed perpendicular to the substrate and the gap between the blade and the substrate was adjusted to about 100 mm. Fluorinated copolymer solution was supplied between the blade and the substrate. Humid air was supplied to the solution surface with a controlled flow velocity. Superhydrophobicity is due to a honeycomb-like (Figure 1.10(a)) microporous transparent polymer film obtained in the process [26].

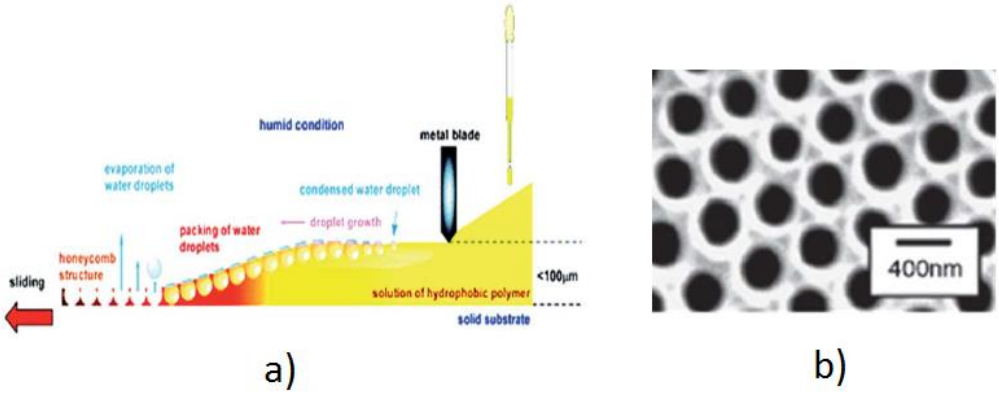

Figure 1.10 *a) A schematic illustration of honeycomb patterned film preparation* [26]*. b) The honeycomb-patterned film* [26]*.*

1.3.1.3 *Organic materials.* Several experiments have shown that also oragnic materials can be used to produce superhydrophobic surfaces. Lu et al. [27] have developed a simple and inexpensive method to produce a superhydrophobic coating using ‘‘low-density poly ethylene’’ (LDPE). In Figure 1.11(a) is shown the related nanostructure. Also dimethylformamide (DMF) sprayed with PS solution has been used, as Jiang et al in their work [28]. In this case electrostatic spinning and spraying produce a surface composed of fibers and porous microparticles, as shown in Figure 1.11(b).

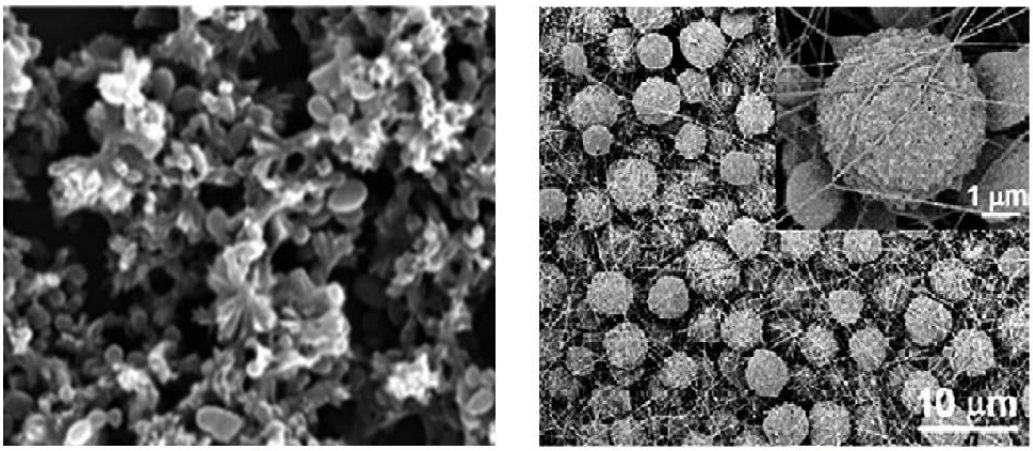

Figure 1.11 *a) A SEM image of the flower-like crystal structure of LDPE* [27] *b) A SEM image of the PS surface produced by electrostaticspinning and spraying*[28].

1.3.1.4 *Inorganic materials.* TiO_2 [29] and ZnO [30]are naturally hydrophilic but after a proper senthytization treatment they can exhibit superhydrophobic properties. Moreover when the superhydrophobic films were exposed to UV light their surface superhydrophobicity transformed into superhydrophilicity [29]. When the film is exposed to UV radiation, electron–hole pairs were produced resulting in the adsorption of hydroxyl group on the ZnO or TiO_2 surface. Consequently, the superhydrophobic property of the film is converted to superhydrophilic. However if UV irradiated film is stored in dark for a week it became superhydrophobic again . In Figure 1.12 TiO_2(a) and ZnO (b) films can be seen.

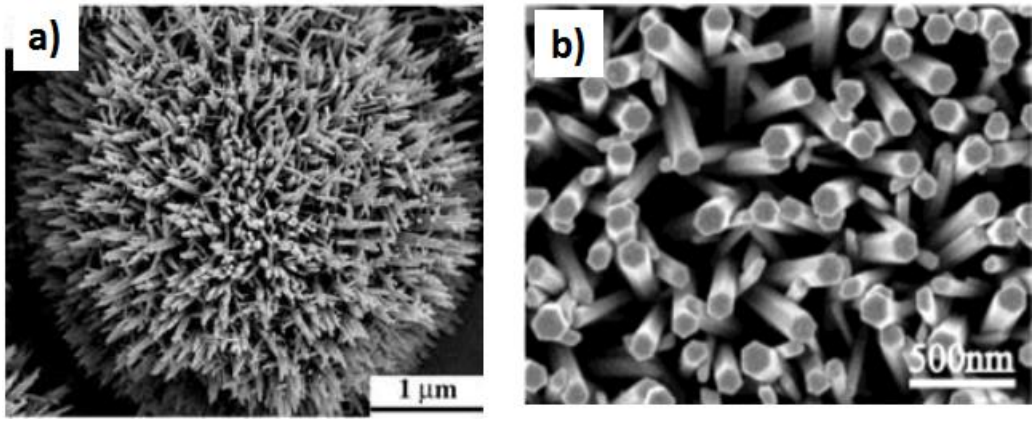

Figure 1.12 *a) TiO_2 nanorods film* [29]. *b) ZnO nanorods film* [30].

1.3.2 Making a rough surface and modifying it with material of low surface energy

1.3.2.1 *Wet chemical reaction and hydrothermal reaction.* Wet chemical reaction is a straightforward technique that can effectively control the dimensionality and morphology of the nanostructures produced, as nanorods, nanoparticles or mesoporous inorganics [31] [32]. This method is especially used to produce superhydrophobic films on metal substrates , like copper [33]. Generally a metal substrate is immersed in a solution (like n-tetradecanoic acid solution [33] or fluoroalkylsilane [34] which resulted in surface modification of the substrate, which then exhibited superhydrophobicity.

The hydrothermal reaction method allows to fabricate functional materials with different pattern and morphologies using a "bottom-up" route. These methods are very simple and flexible and for this reason they can be used to produce surfaces of reasonable shape and size.

1.3.2.2 Electrochemical deposition. It is a galvanic deposition process by which a film of solid metal is deposited from metallic salt solution onto an electrically conducting surface. This method is very interesting because objects of any size or shape may be coated (also 3D objects), as shown in Figure 1.13. For example, Jiang et al [35] employed electrochemical deposition method, inducing long chain fatty acids (HDFT) to produce micro and nanoscale hierarchical-structured copper mesh that exhibited superhydrophobicity. Thank to this process a metal "pond skater" is able to stand on superhydrophobic copper legs [35], as shown in Figure 1.13.

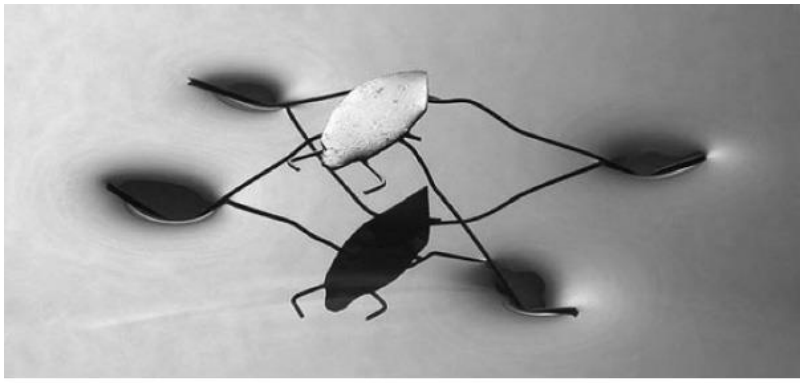

Figure 1.13 *A metallic model "pond skater" of copper legs treated with silver and HDFT* [35].

1.3.2.3 Lithography. Lithography is a conventional and well-established process for patterning various layers, such as dielectrics, conductors, or semiconductors,

on a surface[36],[37],[38]. Conventional lithography can be extended replacing light with other radiation beams to produce micro and nano-pattern surfaces. A radiation sensitive materials called resists are applied as a thin coating, typically spreading a solution over a substrate, with spin coating techniques. The photo resist-coated wafer is then heated up to drive out excess photoresist solvent. The resist film is subsequently exposed directly to a focused electron beam or to a shaped photon or X-ray beams. In the last two cases the shaping is provided by a photomask. After chemical changes occurred during light exposure, some of the photoresist is allowed to be removed. Hence exposed resist film is immersed in a developer solvent to generate three-dimensional relief images. The exposed resist film is then developed typically by immersion in a developer solvent to generate three-dimensional relief images. If resist film is such to be more soluble after exposure a positive-tone image of the mask is produced. Conversely, if resist film is such to be less soluble after exposure this leads to a generation of negative-tone image. The resist film must "resist" the etchant and protect the underlying substrate while the bared areas are being etched. The remaining resist film is finally stripped, leaving an image of the desired circuit in the substrate. The process is repeated many times to fabricate complex semiconductor devices. The process is shown in Figure 1.14.

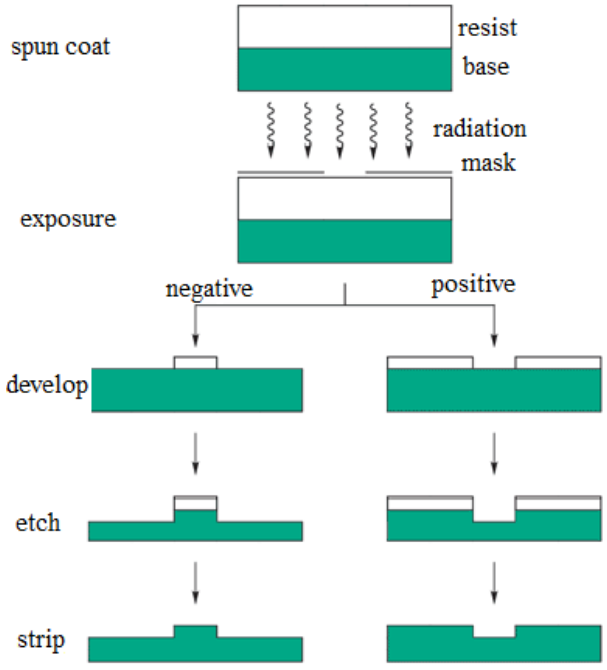

Figure 1.14 *Schematic representation of the lithographic process.*

Lithography techniques used in making superhydrophobic surfaces include, nanoimprint lithography, electron beam lithography, X-ray lithography, and colloidal lithography. It should be noted that these variants are not rigidly or definitely distinguished but rather several of them can be involved . Martines et al [39]employed the technique of electron beam lithography and plasma etching to produce a surface covered with nanopits and nanopillars, as shown in Figure 1.15. This surface exhibited superhydrophobic properties after treatment with octadecyltricholorosilane.

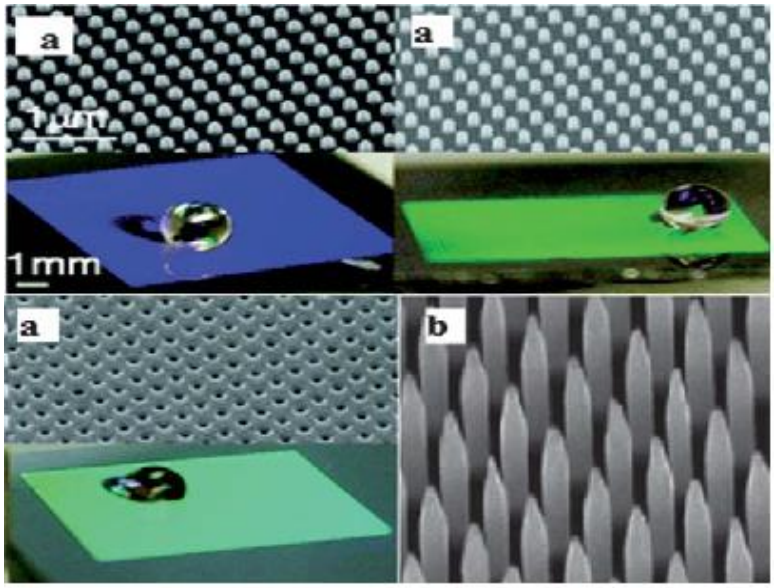

Figure 1.15 *The superhydrophobic surfaces produced by lithography techniques. (a) A SEM image of nanopits and nanopillars produced byelectron beam lithography and plasma etching*[39] *(b) A SEM image of the nanopillars after hydrophobization. The base diameter of the pillars is about 120 nm*[39].

1.3.2.4 Etching and chemical vapour deposition. Plasma etching processes and Chemical Vapor Deposition (CVD) have been extensively used with polymers to fabricate superhydrophobic surfaces with different morphologies, [40].

Plasma Etching consists of removing a thin layer of a sample surface using short pulses of a plasma (a partially ionised gas containing free electrons and radicals) while CVD is a synthesis method where the substrate is exposed to

one or more volatile precursors, which react or decompose on the surface to produce a deposit.

Engineered surfaces exhibiting hydrophilic and hydrophobic properties are synthesized by plasma-based. Garrod *et al.* [41] analyzed the stenocara beetle's back and replicated the surface by employing a micro-condensation process using plasma chemical patterns (Figure 1.16(a)). The micro textures are designed and constructed over Silicon surfaces and they exhibited superhydrophobic behavior with a contact angle of about 174° (Figure 1.16(b)) [42].

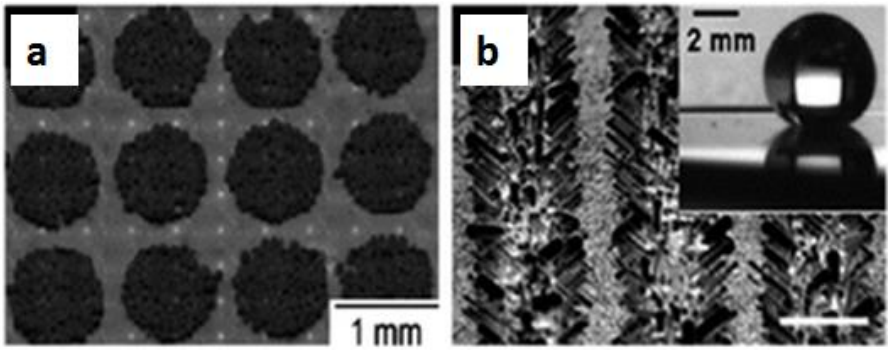

Figure 1.16 (a) *An optical image showing the pulsed plasma deposited poly(glycidyl methacrylate) array reacted with 50 μm amino-polystyrene microspheres* [41]*. (b) A SEM image of Si nanowires grown on the Si islands with Au cluster on the tips of the nanowires treated by plasma etching , the scale bar is 5 μm* [42]*.*

1.3.2.5 Sol–gel method. The sol–gel method [43] can be employed in the fabrication of superhydrophobic surfaces in all kinds of solid substrates [44], [15]. It involves a chemical solution deposition, during which the chemical solution or sol is utilized as a precursor on the selected substrate to form a gel-like network. Material of low surface energy and micro- or nanoparticles can be added into the network to create superhydrophobic surfaces. For its compatibility with glass, this type of method is particularly favored in creating transparent and superhydrophobic films on glass surfaces [15].

Shirtcliffe *et al.* [45] used different proportions of (organo triethoxysilane) methyltriethoxysilane (MTEOS) to produce sol–gel foams. These foams, when exposed to different temperatures, exhibited binary switching between superhydrophilicity and superhydrophobicity, as shown in Figure 1.17

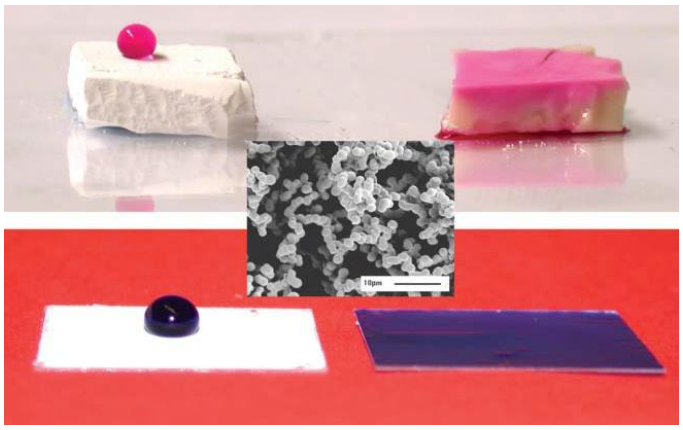

Figure 1.17 *Superhydrophobic surfaces produced by the sol–gel method. Top, phenolphthalein in water on MTEOS sol–gel foams heated to 390 °C (left) and 400 °C (right). Centre, a SEM image of an unheated sol–gel foam. Bottom, foam films on glass cover slips with (left)* [45].

1.3.2.6 Phase separation. Colloidal aggregation methods can also involve phase separation, which separates the solid phase from a metastable mixture of substances by changing surrounding conditions, for example of temperature and pressure, to fabricate patterned surface structures. In are reported SEM images of porous superhydrophobic poly (vinyl chloride) surfaces obtained with the different ethanol content in the PVC solution:

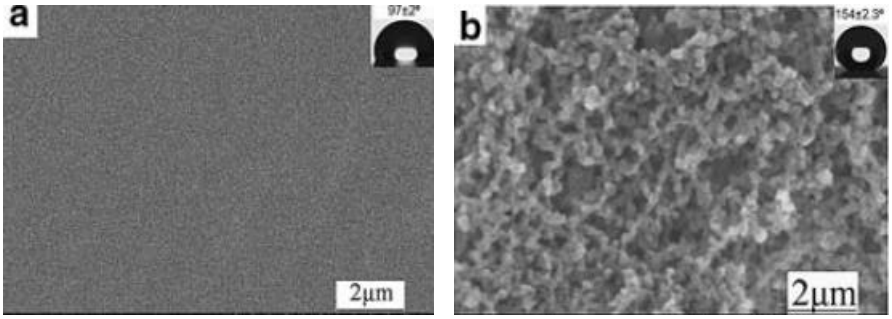

Figure 1.18 *SEM images of PVC surfaces obtained with the different ethanol content in the PVC solution: (a) 0% (v/v) (b) 50% (v/v)*

1.4 Aim of the work

Superhydrophobic surfaces find application in a wide range of fields. One of the most important is connected to anti-icing systems fabrication. Ice formation and accretion may hinder the operation of many systems critical to several infrastructures, including airplanes, power lines, windmills, ships, and telecommunications equipment. Often deicing protocol, such as spraying systems with glycol-based fluids or mechanical removal systems are used to mitigate complications due to icing by removing ice that has formed on a surface. Unfortunately such processes are suboptimal, however, because they require frequent application, may be expensive, and often have detrimental environmental consequences. Moreover, this kind of active systems aims just to remove ice after it forms, they are not able to prevent ice formation by design. Still now a surface able to do this has not been invented yet. An appealing and universal approach is to design surfaces to which ice minimally adheres, ideally such that the ice debonds under its own weight or due to natural factors such as wind. Superhydrophobic surfaces represent the most promising starting point to achieve this goal. In fact lot of studies indicate that ice adhesion reduces with increasing hydrophobicity of the surface [5], [17]. The state of the art of ice-phobic surfaces is represented by such a surfaces that exhibit an extremely low hysteresis contact angle [5], but also in this case they aren't totally ice formation free. Aizenberg *et al.* called these surfaces SLIPS (slippery liquid infused porous surfaces) and, as can be seen in Figure 1.19 they are prepared by infiltrating a porous/textured solid with a low-surface-energy , chemically inert liquid to form a smooth and homogenous lubricating film on surface.

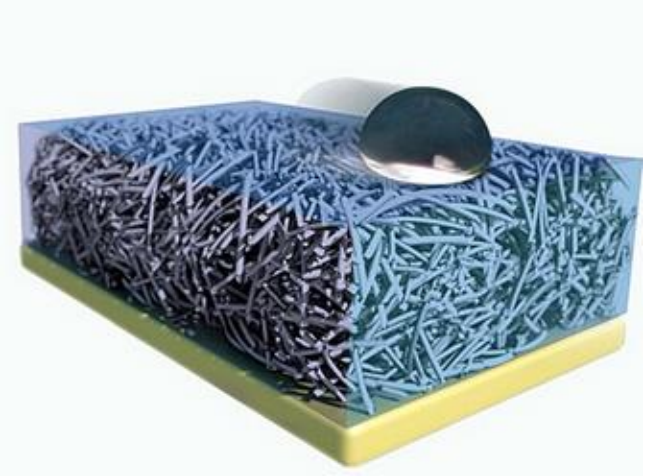

Figure 1.19 *Slippery Liquid Infused Porous Surfaces*

However, when the ambient temperature dramatically drops ice nucleation and the following growth are unavoidable. For these reasons the problem of ice nucleation and its growth still persist despite the many efforts made by several research centers, Universities and companies.

Another relevant field where superhydrophobic surfaces can find interesting application is the fabrication of biomedical nanosensors, as shown in a recent work [46]. In fact, the detection of a few molecules in a highly diluted solution is of paramount interest in fields including biomedicine, safety and eco-pollution in relation to rare and dangerous chemicals. One of the most promising devices in this for this kind of measurements are represented by plasmonic-based nanosensors [47]. However they are not able to detect molecules dissolved in femto or attomolar solutions because their mechanism, which is diffusion limited, is such that detection times become impractical at such concentrations. Di Fabrizio *et al.* demonstrated that by combining super-hydrophobic artificial surfaces and nanoplasmonic structures, that few molecules can be localized and detected even at attomolar (10^{-18} mol l^{-1}) concentration. Basically, when a drop of an extremely diluted solution is deposited on a textured, super-hydrophobic substrate and is allowed to evaporate, the drop will reduce in volume while maintaining its quasi-spherical shape (Figure 1.20 (a)). During evaporation, the solution therefore becomes more and more concentrated. At the end of the process, when the shape and concentration reach a condition of instability, the drop collapses and the solute deposits in a suspended confined region with an area of a few square micrometres (Figure 1.20 (b)).

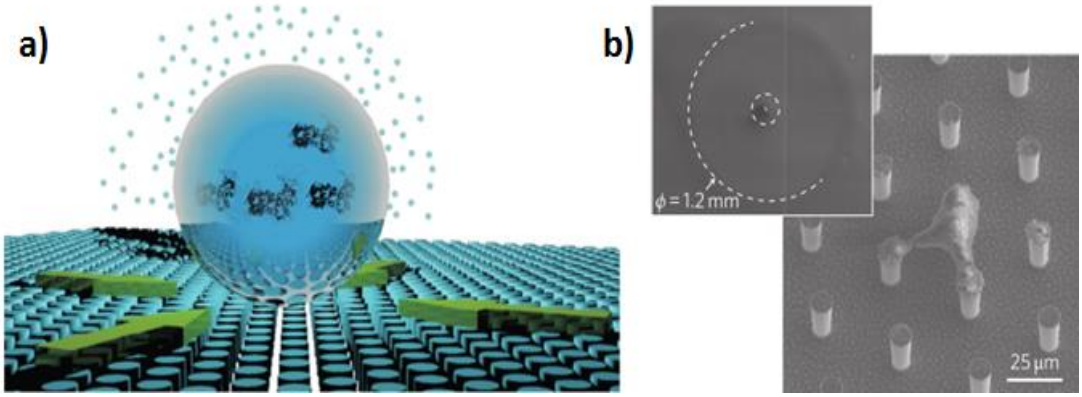

Figure 1.20 *(a) Sketch representing the high contact angle and evaporation process with no pinning of the drop and no solute left on the substrate during drop concentration (b) SEM images of the footprint diameter of the drop and the suspended deposition of the solute* [46].

As shown by these examples, it is easily understood why superhydrophobic surfaces are becoming more popular.

The aim of this work is to characterize the fabrication process of quasi-1D self-assembled TiO_2 nanostructured (obtained by Pulsed Laser Deposition) with independently tuneable multiscale features allowing fine control over its surface wettability. The controllability and the possibility to locally switch between superhydrophobic/superhydrophilic makes this technology a potential breakthrough in any field where the wettability plays a key role.

Chapter 2

Experimental Methods

2.1 Pulsed Laser Deposition

Pulsed-laser deposition (PLD) is one of the most promising techniques for the formation of complex-oxide heterostructures, superlattices, and well controlled interfaces. The technique of PLD, introduced in 1965 by Smith and Turner [48], is conceptually simple, as illustrated schematically in Figure 2.1. A pulsed-laser beam leads to a rapid removal of material from solid target and to the formation of an energetic plasma plume, which then condenses onto a substrate, allowing nanostructures growth.

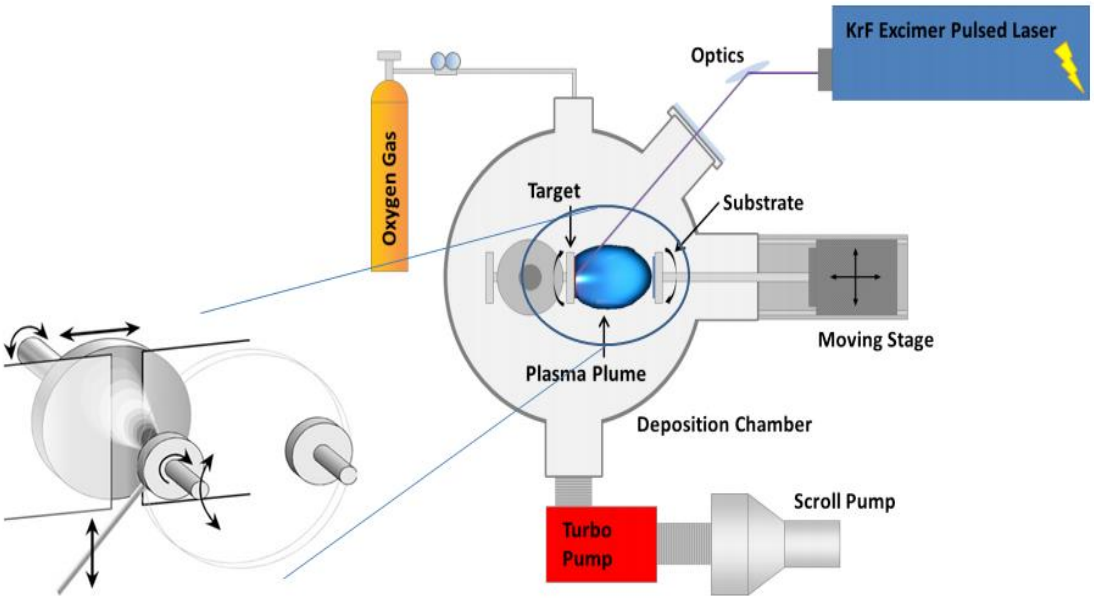

Figure 2.1 *Schematic diagram of a pulsed laser deposition apparatus*.

A set of optical components is used to focus and raster the laser beam over the target surface, which is generally mobilized in order to achieve uniform ablation.

The UV laser beam at 248 nm employed for this work is produced by a Coherent® excimer KrF laser, shooting pulses with a duration of 15 ns, 400 mJ of energy and a repetition rate of 20 Hz.

The decoupling of the vacuum hardware and the evaporation power source makes this technique so flexible that it is easily adaptable to different operational modes without constraints imposed by the use of internally powered evaporation sources. In contrast to the simplicity of the technique, the mechanisms in PLD—including ablation, plasma formation, and plume propagation, as well as nucleation and growth—are rather complex [49].

All the TiO_2 substrate employed in this study are deposited using a set of optimized parameters and conditions, meticulously derived on previous studies on titanium dioxide film growth [50], [51]: the deposition is performed in dynamic mode (the substrates holder rotates continuously at a speed of 48 rpm, giving an increased
homogeneity to the film), the oxygen background gas is kept at a stable pressure (10 20 40 and 60 Pa, according to the desired level of porosity) and the number

of laser pulses is calibrated for each deposition to achieve the intended thickness through an experimentally derived formula.

3.1.1 *Ablation and Plasma Formation.* In the process of laser ablation, the photons kinetic energy is converted first into electronic excitations and then into thermal, chemical, and mechanical energy [52]. This brings to a rapid removal of material from the surface. Heating rates as high as 10^{11} K s^{-1} and instantaneous gas pressures of 10–500 atm are observed at the target surface [53].

The photons-solid interaction mechanisms may depend on the laser wavelength. The most important effect of the laser's wavelength, whose lower limit is approximately 200 nm due to photons absorption by background gas molecules and optical elements, is its determination of the penetration depth.

The mechanism underlying the material removal from the target also depends on pulse length. For relatively long pulse durations, such as the tens of nanoseconds typical for excimer lasers, there is a strong interaction between the forming plume and the incident beam, leading to a further heating of the species. On the other hand, for femtosecond pulses, the ablation threshold energy can be even hundreds of times less than that for nanosecond pulses. The resulting plume is then more confined and dense.

Finally the laser fluence at the surface of the target has to exceed a certain threshold. Under a certain threshold no particulate is seen, while above, this parameter affects the size of the particulate and the density of the deposited film.

3.1.2 *Plume Propagation.* Plume propagation has been studied extensively using optical absorption and emission spectroscopy combined with ion probe measurements [53], [54], and does not need to be discussed in detail here.

When the laser radiation is absorbed by the target, photons energy is converted first in electronic excitation and then to mechanical energy to cause evaporation, ablation, excitation and plasma formation. Evaporated species form a plasma plume consisting of a mixture of energetic atoms, molecules, electrons, ions, clusters, small aggregates and particulate. Since the collisional mean free path inside the dense plume is very short, immediately after the laser ablation, the plume rapidly expands into the vacuum from the target surface to form a nozzle jet with hydrodynamic flow characteristics.

3.1.3 *Control of Stoichiometry.* The stoichiometric removal of material from a solid target is undoubtedly the single most important factor in the success of PLD. For a vast majority of ceramic targets, and for ablation rates that result in a dense plasma, the removal of material does indeed preserve stoichiometry. Stoichiometric removal of the material from the target, however, does not necessarily translate into the growth of stoichiometric materials, as not all

elements get incorporated at the same, some resputtering can occur [55] and volatile elements may re-evaporate from the growth surface.

For oxide materials, proper control of the oxygen content is of paramount importance. a metal oxide film can be obtained using both a metal or an oxide target. Superhydrophobic surfaces of this thesis work have been fabricated by deposition from a Lesker® Titanium Dioxide target (purity 99.99 %).

2.2 Contact angle measurements

2.2.1 Static Contact Angle

One of the most important parameter in the characterization of a superhydrophobic surface is static contact angle. As discussed in Chapter 1, the higher is the contact angle the lower is the wetted area.

Static contact angle measurements have been taken with an Optical Contact Angle Measuring Instrument (Model OCA15, Dataphysics Instruments GmbH, Filderstadt). As shown in Figure 2.2(a), samples are positioned on a support and illuminated by a light source with an electronic dosing system; water droplet is dispensed over the samples taking care not to over press and deform the droplet itself and avoiding measurement errors.

In order to be sure that no capillary effects arise, the volume of liquid droplets used in the measurements is 4 µl. The capillarity length of a water droplet is defined as [56]:

$$l = \left(\frac{\gamma}{\rho g}\right)^{\frac{1}{2}} \tag{2.1}$$

where γ is the surface tension of the fluid-fluid interface, ρ is the density of the fluid and g is the gravitational acceleration. In the case of water the capillary length is equal to 2.7 mm. Since the characteristic length scale (diameter) of the 4 µl water droplet is approximately equal to 1.97 mm and is less than the capillary length. This implies that the effect of gravity does not arise and the droplet assumes a spherical-cap shape.

In order to measure contact angle, a dedicated camera captures a picture of the droplet deposited on the sample Figure 2.2(a). With specific software analysis the droplet profile is automatically extracted by the analysis of grey level of image pixels and then contact angle is measured, as shown in Figure 2.2(b):

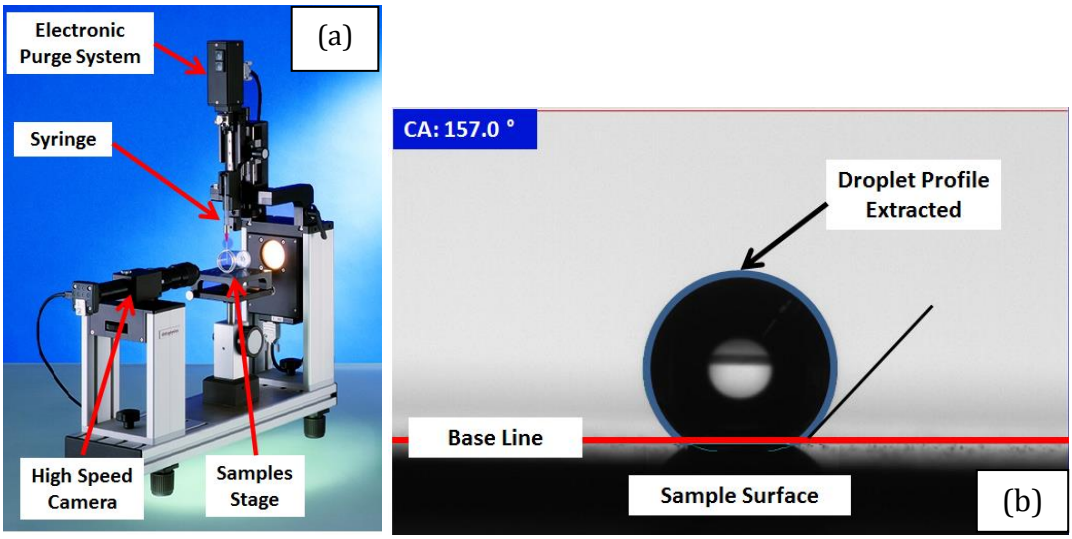

Figure 2.2 *(a)Contact angle measuring instrument OCA 15 - Dataphysics Set-up (b)Profile extraction and contact angle measurement.*

The drop shape is adapted to a fit of a mathematical model which is then used to calculate contact angle. Besides the droplet volume, also the fitting modes adopted to measure the contact angles can affect their values [57]: it was reported that ellipse fitting, circle fitting, tangent searching, and Laplace–Young fitting could cause various values of contact angles of similarly shaped droplets as shown in Figure 2.3.

In the *Circular* and *Ellipse fitting method* the drop contour is fitted to a segment of a circle and of an ellipse. The most complicated, but also the theoretically most exact method for calculating the contact angle is the *Young-Laplace fitting method*.

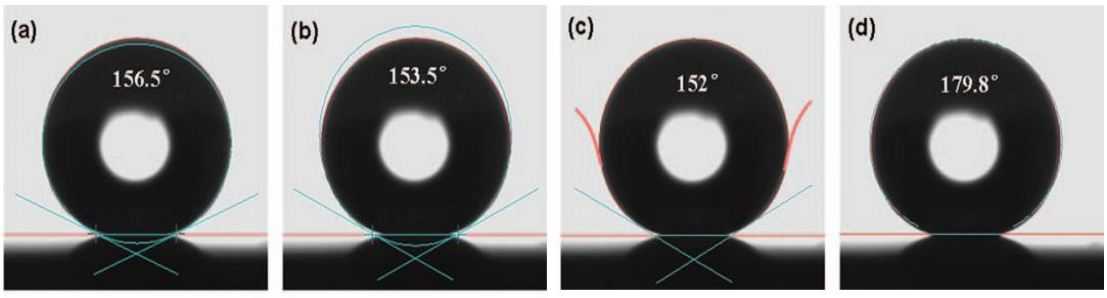

Figure 2.3 *Images of the same water droplet on a superhydrophobic surface under different fitting modes of the static contact angle: (a) ellipse fitting; (b) circle fitting; (c) tangent searching; (d) and Laplace–Young fitting* [57].

In this method the complete drop contour is evaluated; the contour fitting includes a correction which takes into account the fact that it is not just interfacial effects which produce the drop shape, but that the drop is also distorted by the weight of the liquid it contains. After the successful fitting of the *Young-Laplace* equation the contact angle is determined as the slope of the contour line at the 3-phase contact point.

Static contact angle have been measured by using *Young-Laplace fitting method*. Notice that if the drop was impossible to attach to the surface, contact angle was assumed to be 180°.

2.2.2 Dynamic contact angle and hysteresis contact angle

Besides static contact angle, in order to properly characterize wettability performance of superhydrophobic surfaces, also hysteresis and, if any, roll off have to be analyzed. Important to recall that hysteresis contact angle is giving important information about the surface interaction with liquid and it is a measure of the difference between advancing and receding contact angles while roll-off angle is a direct measure of the surface adhesion.

The classical way to make advancing and receding angle measurements is to tilt the sample until the drop just begins to roll off from the surface. At that time, the downhill contact angle is the advancing angle and the uphill angle the receding contact angle. This is the method has been adopted to do the measurements. The samples were measured at Italian Institute of Technology Headquarter in Genoa, by a goniometer contact angle (OCA 15Pro, Dataphysics Instruments GmbH, Filderstadt). As shown in Figure 2.4, both samples, camera and purge systems are tilted in order to allows the droplet to move and capture its entire dynamic history until it rolls off.

Since during the motion droplet profile is distorted and the symmetry is lost, none of the previous fitting method is suitable for dynamic contact angle measurements. The best fitting model used for this kind of measure is the

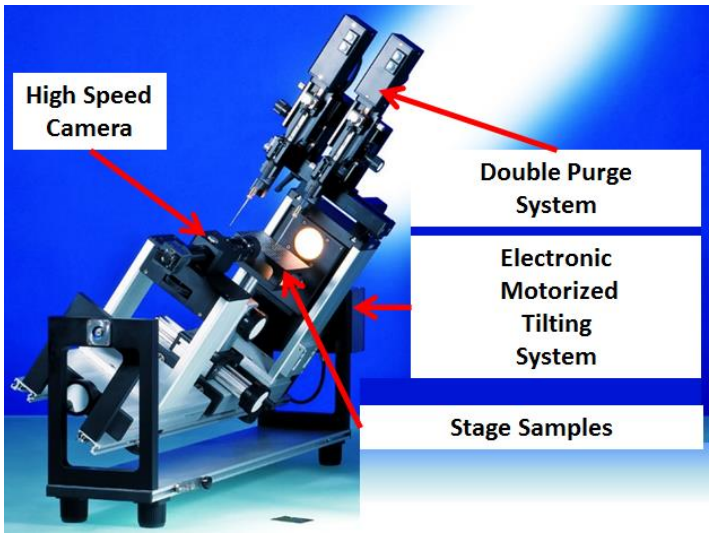

Figure 2.4 *Goniometer Contact Angle Instrument OCA 15Pro Dataphysics Set-Up*

Tangent Method, with whom the part of the profile of a sessile drop which lies near the baseline is adapted to fit a polynomial function of the type:

$$y = a + bx + cx^{0.5} + \frac{d}{\ln x} + \frac{e}{x^2} \tag{2.1}$$

It is worth remembering that advancing and receding contact angles are defined as the angle between drop profile and baseline in the moment just before the drop rolls off from sample surface.

2.3 Surface Characterization

2.3.1 Field Emission Scanning Electron Microscopy (FE-SEM)

The morphology of the TiO_2 layer is probed for its features on micro and nano scale with the use of a Zeiss® Supra 40 Field Emission Scanning Electron Microscope, shown in Figure 2.5. In contrast to classical Scanning Electron Microscopy (SEM) where the electron beam used for the microscopic inspection is produced from a tungsten filament by thermionic effect, in the Field Emission Scanning Microscopy (FE-SEM) the electron current is provided by a Field Emission Gun (FEG). Since electron emission is reached by placing the filament in a very high electrical potential gradient and not by thermionic effect, the

typical problems of classical Scanning Electron Microscopy (i.e. relative low brightness, evaporation of cathode material and thermal drift) are avoided.

Figure 2.5 *Zeiss® Supra 40 field emission scanning electron microscope (FE-SEM)*

The FE-SEM has two anodes for electrostatic focusing. A voltage (0 ~ 5 KV) between the field emission tip and the first anode, called the extraction voltage, controls the current emission (1 ~ 20 μA). An accelerating voltage (1 ~ 30KV) between the cathode and the second anode increases the beam kinetic energy and set the velocity at which the electrons move into the column. In order to prevent scattering and discharges inside the column, samples are placed in a high vacuum chamber (less than 10^{-7} Pa in the gun zone). This voltage combined with the beam diameter determines the resolution. As voltage increases, better point-to-point resolution can be reached. The focusing and refinement of electron beam are given by a lenses system and apertures. Since the higher is the number of electrons, the higher is the statistics and lower is the errors, SEM measurement need a high conductivity sample to be performed. Also for this reason, TiO_2 films have been deposited on Silicon substrates. The imaging mode employed is based on secondary electrons, the ones that are ejected from the sample due to inelastic scattering interactions with the incident electron beam.

The images obtained with Field Emission Scanning Electron Microscopy get direct information about thicknesses, morphologies and feature sizes with a maximum resolution of 5 nm.

2.3.2 Atomic Force Microscopy

The roughness factor has been measured by means of an Agilent Technologies®Atomic Force Microscopy (AFM), model 5500 ((a)). The AFM mechanism [58], shown in (b), is relatively simple: images are obtained by measurement of the force on a sharp tip (curvature radius from 10nm to 2 nm) created by the proximity to the surface of the sample. Typically, the deflection is measured using a laser spot reflected from the top surface of the cantilever into an array of photodiodes.

The AFM can be operated in a number of modes [59], depending on the application and the material composing the sample to be analyzed. In *contact* mode the force between the tip and the surface is kept constant during scanning by maintaining a constant deflection. In this case, the static tip deflection is used as a feedback signal. In the *tapping* mode, the cantilever is instead oscillated at either its resonant frequency by a small piezoelectric mounted in AFM tip holder. The amplitude of this oscillation is greater than 10 nm, typically 100 to 200 nm. The interaction of forces acting this oscillation to decrease as the tip gets closer to the sample. The height to maintain a set cantilever oscillation amplitude as the cantilever is scanned over the sample, is controlled by an electronic servo. The samples analyzed in this thesis work have been measured by AFM operating in *tapping mode*.

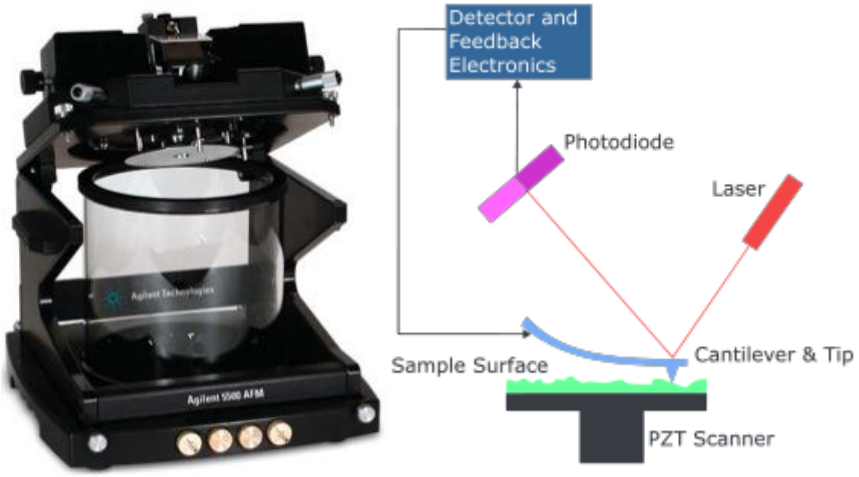

Figure 2.6 *(a)Agilent Technologies 5500 AFM (b)Atomic Force Microscopy mechanism*

2.3.3 UV-Vis Spectroscopy

The optical properties have been determined by means of a Perkin Elmer Lambda 1050 UV/Vis/NIR spectrophotometer with a 150 mm integrating sphere (Figure 2.7). The measurements are made with a wavelength range between 300 nm and 800 nm; the total transmittance and its diffuse value have been acquired. Thanks to the integrating sphere, that allows to filter-out the non-diffused part, also in the case of high scattering materials, a complete light collection is possible. With the sample placed in its proper slot outside the integrating chamber (a different slot is used depending on whether the measurement is a transmittance or reflectance one), light from the power source is filtered by a monochromator and is hence shined upon the sample with a single wavelength at a time, performing a rastering scan within the range of interest; the light transmitted of reflected by the sample is gathered in the integrating sphere and is entirely collected by the detector on the inside.

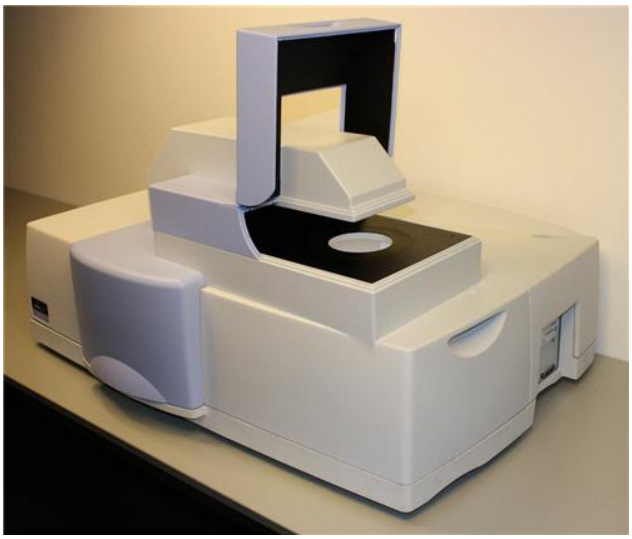

Figure 2.7 *Perkin Elmer Lambda 1050 UV/Vis/NIR system with a 150 mm*

2.3.4 X-Ray Diffraction

Besides AFM, in order to better characterize geometrical properties at nano-scale, also X-Ray Diffraction (XRD) analysis have been performed. Measurements were performed with a Rigaku SmartLab X-ray diffractometer (Figure 2.8) at Italian Institute of Technology Headquarter in Genoa.

Figure 2.8 *Rigaku SmartLab X-ray diffractometer*

X-ray di diffraction is based on the constructive interference between monochromatic X-rays and a crystalline sample; these X-rays are obtained with a cathode ray tube and filtered to produce monochromatic radiation are then collimated and directed toward the sample. The interaction of the incident ray with the sample produces constructive interference (and therefore a diffracted ray) only when Bragg's law is satisfied (2.1):

$$n\,\lambda = 2\,d\,\sin\theta \qquad (2.1)$$

where where n is an integer, λ is the incident wavelength, d is the spacing between the planes of the atomic lattice and θ is the angle between the incident angle and the scattering plane. The resulting diffracted X-rays are then detected and counted to achieve a visual display of the diffraction distribution. By vary the detection directions through a range of 2θ angles, all possible diffraction directions of the lattice are attained due to the random orientation of the powdered material. Since each mineral specimen has a unique set of d-spacing values, the pattern of di diffraction peaks is used as a fingerprint a material, with

the help of standard reference pattern to be used for comparison. As will be shown in Chapter 4, grain size is given by the Scherrer equation.

Chapter 3

Surfaces Fabrication and Process Optimization

3.1 Fabrication

As shown in Chapter 1, the fundamental requirements of superhydrophobic surfaces are a high roughness or micro or nanostructured surface relief and a low a low surface energy of material. The first requirement is fulfilled with fabrication of TiO_2 substrates with a forest-like morphology constituted by Anatase nano-trees by means of Pulsed Laser Deposition. Nano-trees surface exhibit high roughness factor but also high surface free energy and for this reasons substrates behave as superhydrophilic surfaces. In order to switch the behavior to superhydrophobic a sensitization process is needful. The aim of this process is to reduce the surface free energy of substrates, dipping them in a low energy molecule solution. From literature, several low energy materials have been used, n-tetradecanoic acid solution [60], poly(dimethysiloxane) vinyl terminated (PDMSVT) [31], perfluoroalkyl ethyl methacrylate (PPFEMA) [25] and perfluorooctane sulfonic acid (PFOSA) [61] are few examples.The molecule used in this work is SIGMA-ALDRICH® perfluorononanoic acid (PFNA) with chemical formula $C_9HF_{17}O_2$ (Figure 3.1) and purity of 97%. In Figure 3.1 is also reported the Raman spectra of PFNA powder.

Sensitization process consists of dipping samples into PFNA-Ethanol solution and rinsing them with ethanol to remove excess PFNA molecules. Finally, samples are left to dry in atmosphere. Process control parameters are dipping time and molar concentration of sensitizing solution. In order to understand the effects of these parameters on superhydrophobic performance and find the best conditions of sensitization, samples of different thickness and treated with different dipping time and molar concentrations have been measured. The results of are reported in the following paragraph.

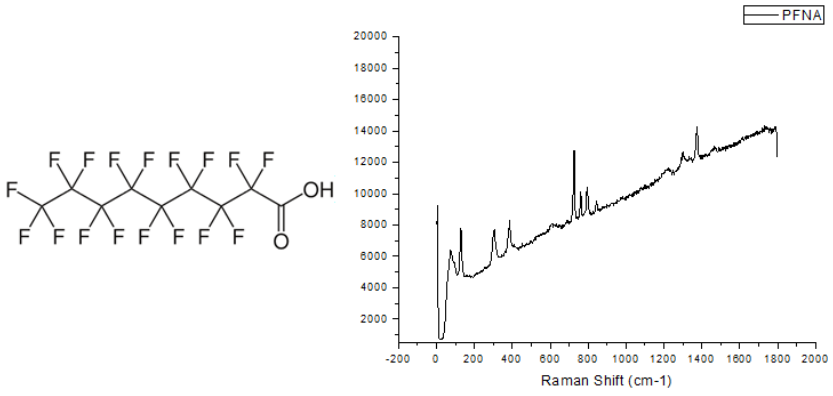

Figure 3.1 *Chemical structure and Raman spectra of PFNA*

3.2 Process Optimization

Since preliminary measurements show that for high deposition pressures contact angles were are very high and sometimes they are impossible to measure because the drop does not attach to the surface, the process optimization has been performed on samples fabricated at 10 Pa deposition pressure. In this way, it has been possible to appreciate all the effects of dipping time and molar concentration on contact angles.

3.2.1 Contact Angle VS Molar Concentration

In this first session the sensitization time is kept constant in order to understand the relationship between contact angles and molar concentration of the hydrophobic sensitizer. TiO_2 samples with different thicknesses (1, 2 and 3 μm) have been sensitized with a bath of 0.1M, 0.5M and 1M PFNA solution in Ethanol and chemical treatments have been performed with 2, 15 and 30 minutes dipping time. Keeping constant the sensitization time, contact angles variations underlined by plots in Figure 3.2, Figure 3.3 and Figure 3.4 are assumed to be due to different chemisorption of the hydrophobic molecule.

Figure 3.2 shows contact angles dependence from molar concentration exhibited after 2 minutes dipping time by samples 1μm, 2μm and 3μm thick. In this case, when the molar concentration is low – namely 0.1M - contact

angle values are similar for different thickness. This fact can be attributed to the low PFNA absorption. Indeed, even though the PFNA uptake is usually higher for thicker films having higher surface area, low dipping time is not favoring the molecule adsorption on the TiO2 surface. By increasing the concentration, even at low dipping time PFNA is able to better cover the thicker nanotrees. The contact angle values reach a maximum at 0.5M and then decrease when molar concentration is 1M. The latter phenomenon could be explained by the fact that the PFNA molecule agglomerates on the surface crating areas where pinning is possible. The trends described above are also underlined by gradient in the CA difference with increasing molar concentration. The strongest decrease effect at 1M PFNA concentration is observed on the thinner sample where agglomeration is more luckily to occur.

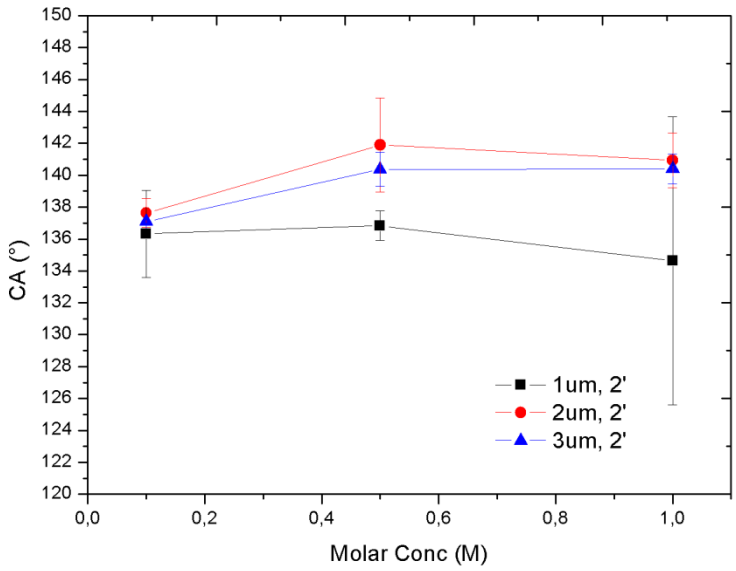

Figure 3.2 *CA plotted versus molar concentration after 2 minutes sensitization*

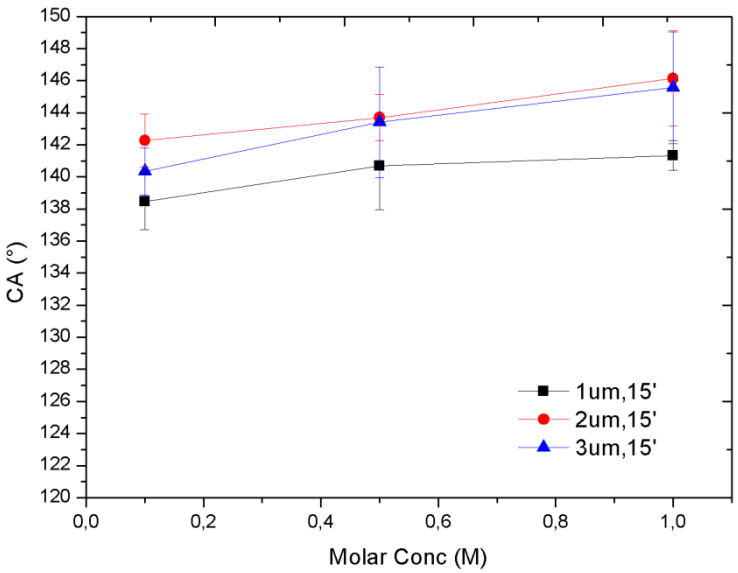

Figure 3.3 *CA plotted versus molar concentration after 15 minutes sensitization*

The same type of relationships are reported also for the case of 15 (Figure 3.3) and 30 (Figure 3.4) minutes sensitization time. As a general figure of merit it can be noticed that CA increases with sensitizer solution concentrations, however, since the sensitizer is left for chemisorption for longer time, a structural contribution given by island reorganization of the nanotrees start being present. This appears evident in the smaller gradient in CA difference with increasing concentration.

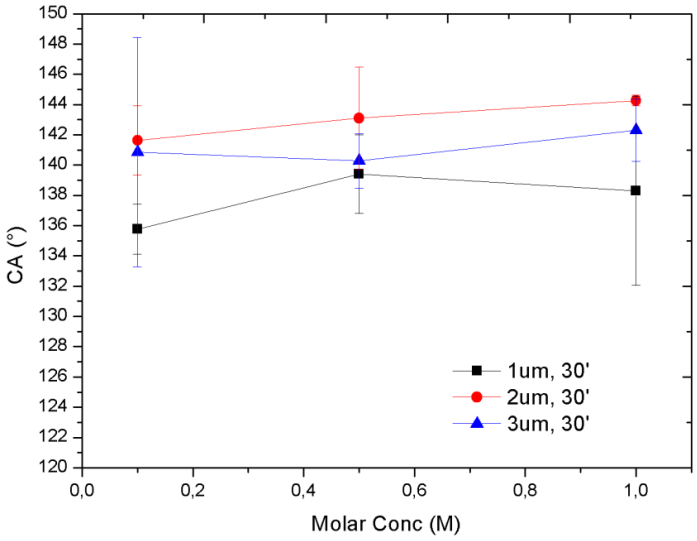

Figure 3.4 *CA plotted versus molar concentration after 30 minutes senstitization*

3.2.2 Contact Angle VS Dipping Time

In this session molar concentration of hydrophobic sensitizer is kept constant and the CA is plotted against sensitization time. Here being the CA is influenced in different proportion by both a structural change due to island reorganization of the surface and by an enhancement in molecule adsorption.

In Figure 3.5 samples are sensitized with 0.1M PFNA solution. For short sensitizations the surface results poorly sensitized and not collapsed in island. With longer sensitization both the phenomena start to affect the wettability and the CA increases.

When samples are sensitized with 0.5M and 1.0M PFNA solution (Figure 3.6 and Figure 3.7), the surfaces of all 1µm, 2µm and 3µm thick films result already sensitized after 2 minutes and the island organization (see Chapter 4) is not bringing significantly its contribution even after 30 minutes. The negative change in CA observable after 30 minutes is again probably due to the same PFNA agglomeration phenomenon mentioned in the previous session.

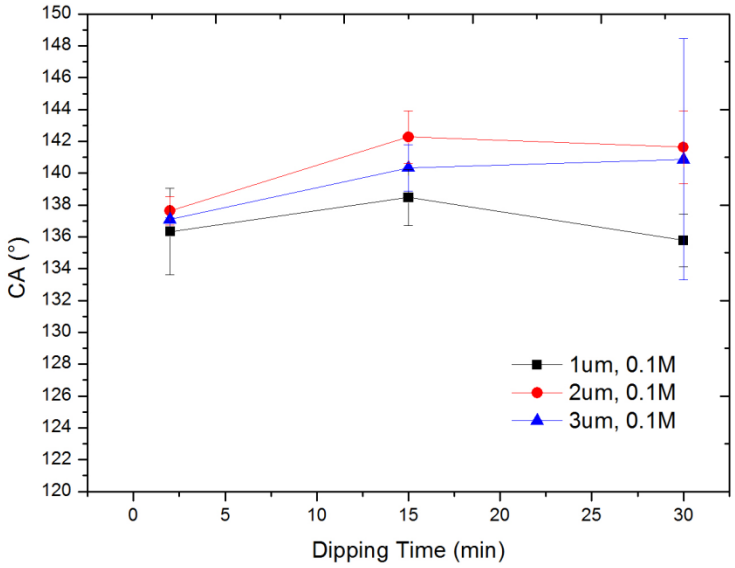

Figure 3.5 *CA plotted versus dipping time in a solution of 0.1M PFNA in Ethanol.*

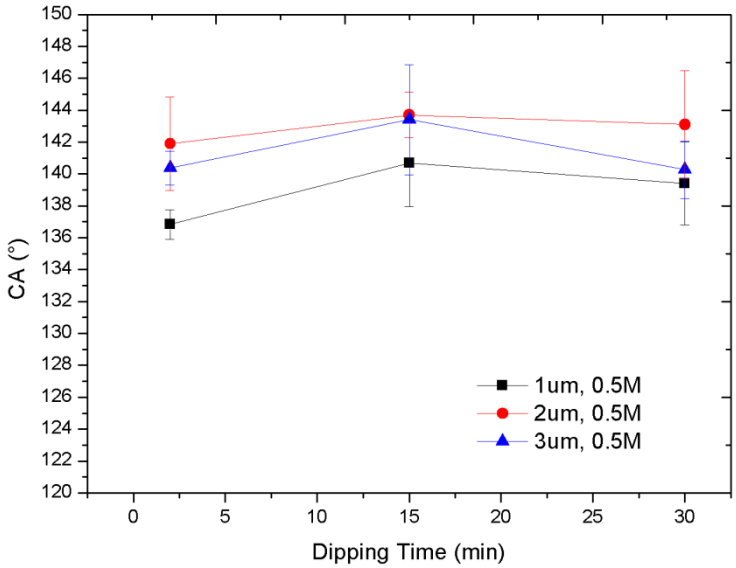

Figure 3.6 *CA plotted versus dipping time in a solution of 0.5M PFNA in Ethanol*

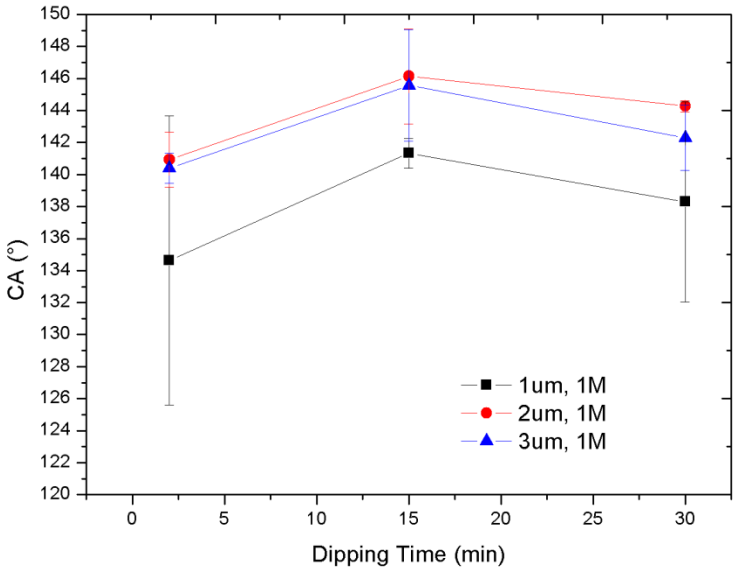

Figure 3.7 *CA plotted versus dipping time in a solution of 1M PFNA in Ethanol*

3.2.3 Nano-trees collapse and islands organization

Besides the reduction in surface energy, sensitization process also brings to another important effect. As previously shown by Fusi *et a* [51]*l.* a wetting process and subsequent drying induce a reorganization and bundling of titanium oxide nanostructured layer. Over a critical thickness (usually around 1μm), capillary forces acting during evaporation induce bundling of nanostructures and lead to a micrometer-size patterning with statistically uniform islands separated by channels or cracks that are as deep as the layer thickness.

These capillary forces may act at the base of nanostructured columns (at the weakest point of the nanostructures), or where liquid/vapor menisci are formed between the columns, but are not strong enough to lead to a complete surface organization [51]. Thus, the mechanism leading to the final pattern may be related to capillarity forces associated with the liquid/vapor menisci at the free ends of the columnar structures, which produce a torque acting on the nanostructured columns. Because of this torque, the material may fracture at his weakest point, i.e., at the column base. Columns are then displaced by capillary forces and by convective flows of the evaporating liquid , causing material shrinkage and formation of aggregates.

As demonstrated by Fusi *et al.*[51] and as in the characterization process explained in Chapter 3, island organization depends on several factors like sensitization solution surface tension, film thickness and porosity. Experiments have also shown a relation with timing of sensitization process. Indeed we observed that island organization occurs if surfaces are sufficiently long time immersed. Figure 3.8 shows the differences between surfaces sensitizing for 30s (a) and for 120s (b). A longer immersion time leads to a deeper liquid penetration in the porous nanostructure that means a stronger capillary force effect.

Data have shown that very high contact angles are gained when island organization of TiO_2 hierarchical nano-structures occurs. As shown in Figure 3.8, when sensitizing time is sufficiently high, TiO_2 nano-trees collapse occurs, and this leads to higher contact angle. In Figure 3.8 are also reported corresponding water droplet images. Surface that has been sensitized for 30s, exhibited low super-hydrophobicity with maximum water contact angle of 158.6°. Conversely, surface whose sensitization time was 120s exhibits high super-hydrophobicity with maximum water contact angle of 169°.

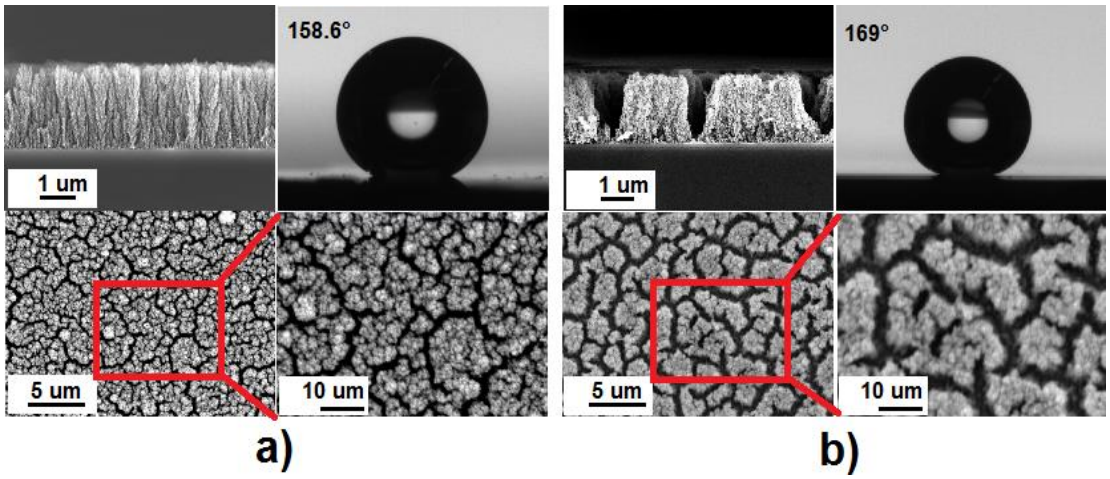

Figure 3.8 *(a) SEM images (side and top view) of 30s sensitized TiO_2 surface and corresponding water contact angle. (b) SEM images (side and top view) of 120s sensitized TiO_2 and corresponding water contact angle.*

This can be explained taking into account that island organization brings to the formation of cracks and channels where air gets entrapped. Higher is the percentage of air entrapped in the surface, lower is the surface free energy of sample and this brings to higher contact angles. This phenomenon will be thoroughly investigated and discussed later in this work.

3.2.4 Conclusions

Experiments have shown that very low molar concentration of PFNA solution gives always the lowest contact angles and this is explained by considering the fact that a very small number of molecules of PFNA are available for the sensitization.

The highest contact angles is reached in the case of 15 minutes dipping time and 1M PFNA solution. Under this conditions the average contact angle is 145.6° while the maximum value observed is 149.6°. Another set of parameter gives similar contact angles. In fact with a 30 minutes dipping time and 0.5M PFNA solution, the average contact angle is 143.1° while the maximum value observed is 146.7°. Moreover, for samples fabricated at higher pressures, islands organization effect on contact angle is so strong that it totally compensates the small differences observed in the two last sets of sensitizing parameters.

These considerations allow to choose between two set of parameters, minimizing fabrication costs without losing in performance. Hence the selected sensitizing parameters are 0.5M molar concentration and 30 minutes dipping

time. In addition, it is to notice that the higher is the dipping time the stronger is island organization, as shown in Figure 3.8. Then, 30 minutes of dipping time allows to saturate this effect .

Chapter 4

Characterization and Results

4.1 Superhydrophobic Surfaces Performance

The most important parameter has to be considered in order to analyze a superhydrophobic surface performance is undoubtedly the static contact angle. In fact it gives an idea of the static wetting behavior which characterizes a superhydrophobic surface. The higher is the contact angle, the higher is the performance. Secondarily, also wetting dynamic behavior has to be analyzed. For this reason, advancing and receding contact angles have to be measured. For this study the lower is the hysteresis contact angle, the higher is the performance.

4.1.1 Effect of deposition pressure

Studying of surface morphology in superhydrophobic surfaces is of paramount importance: as it has been shown in Chapter 1, superhydrophobic behavior can be achieved with different kind of morphologies but a double scale of roughness is required. Depending on the technique and material used in superhydrophobic surfaces fabrication, morphologies with different level of complexity (or roughness) are obtained. Since morphology is strictly correlated to roughness factor r and surface ratio ϕ_s defined in Chapter 1 [62][19][63], it plays a key role.

The main two factors influencing the morphological properties and features of TiO_2 hierarchical nano-trees by Pulsed Laser Deposition, object of this work, are pressure deposition (stiffness and rugosity) and laser pulses

number (thickness). In this section it is discussed the effect of pressure deposition. The higher is the number of pulses, the higher is the deposited film thickness. On the other hand, pressure deposition influences the porosity of TiO_2 film, as it can be seen in Figure 4.1 where have been reported SEM pictures of film deposited respectively at 1 Pa, 10 Pa, 20 Pa, 40 Pa and 50 Pa. At the lowest pressure, TiO_2 deposition results in a very compact layer and nano-trees are not observed. When pressure increase, film becomes more rough and TiO_2 substrates presents a forest-like morphology constituted by nano-trees. The nano-tree consist of a main body, growing perpendicular to the sample surface, from which stretch out numerous branches, themselves having their own ramifications.

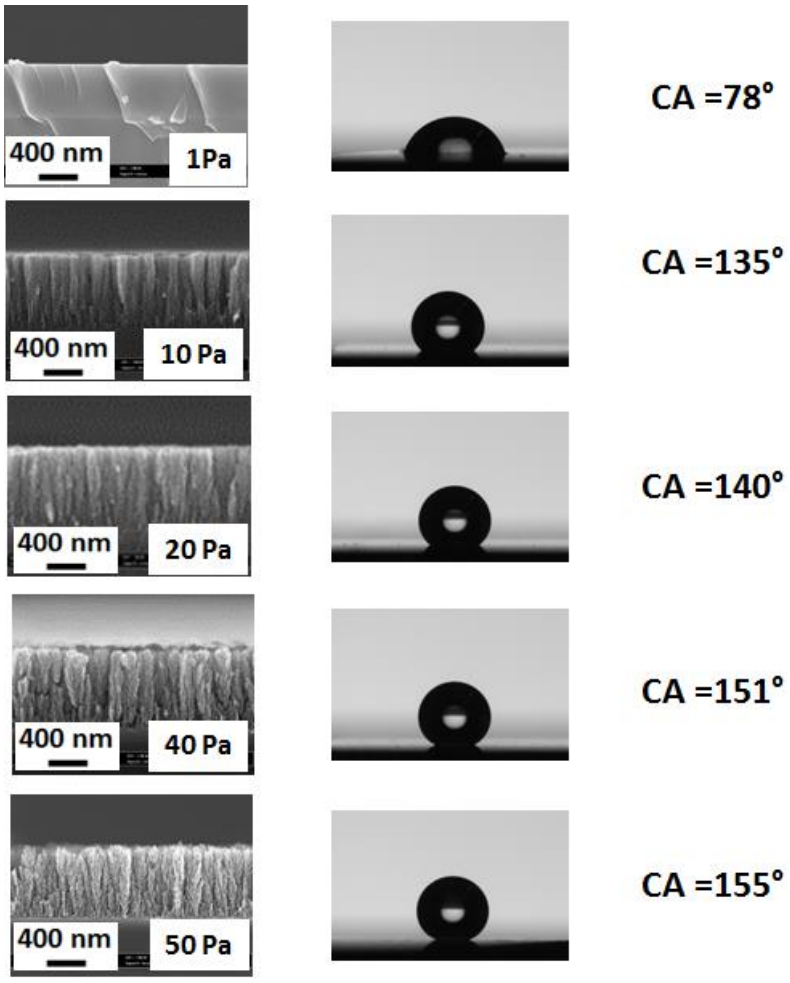

Figure 4.1 *SEM images of 1 μm thick films obtained with 1 Pa, 10 Pa, 20 Pa, 40 Pa and 50 Pa deposition and static contact angles.*

The roughness and porosity are two of the most important parameters that drive the wettability performance. In Figure 4.2, are reported contact angle values of samples swhon in Figure 4.1. In every case data highlight relation between contact angle and roughness. When the pressure increases, nano-structures level increases and this leads to higher contact angles.

For datailed analysis and further informations about TiO_2 nano-trees substrates morphology and their growth by Pulsed Laser Deposition the reader may refer to other works available in litterature [50][64].

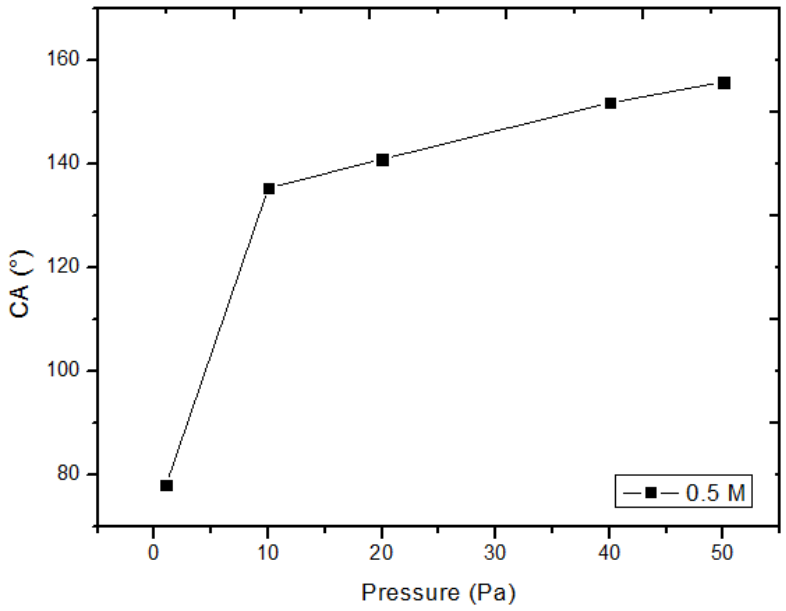

Figure 4.2 *Relation between contact angle and pressure for 1 μm thick film*

4.1.2 Static contact angles

After preliminary tests and measurements, reported in Chapter 3 and in previous section of this Chapter, it has been decided to perform contact angle measurements on samples fabricated at 10, 20, 40 and 60 Pa pressure deposition and film thicknesses ranging from 0.09 to 15 μm.

As can be seen in Figure 4.3, contact angles of samples deposited at 10 Pa exhibit a very weak dependence from thickness. Moreover, the measured values are always lower than 150° (they vary from 141.6° to 146.5°) and then, surfaces are not properly superhydrophobic, but rather hydrophobic, as indicated by literature [3].

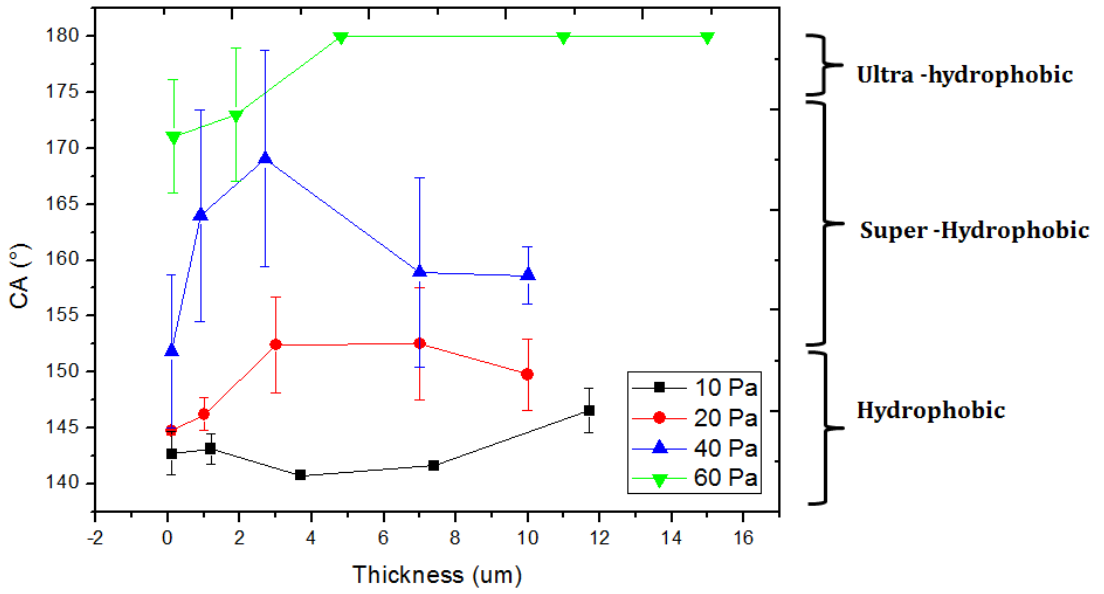

Figure 4.3 *Static contact angles as a function of thickness and deposition pressure*

Samples fabricated at 20 Pa deposition pressure exhibit higher contact angles but still close to superhydrophobic/hydrophobic discriminating value (150°). In this case the dependence from thickness is stronger than the dependence observed in 10 Pa series samples, as Figure 4.3 shows, but the variations are still restrained (they vary from 144.7° to 152.4°).These facts can be explained taking into account that nano-trees collapse and islands organization (see section 4.2.2) in 10 and 20 Pa samples are absent or not completely occurred, as will be shown later.

Taking now a look at 40 Pa samples series, Figure 4.3 shows a strong dependence of contact angle from thickness. In this case mean values vary from 147.1° to 169° while minimum and maximum observed values are respectively 144.2° and 179.8°. Again, island organization helps for results explanation. The highest contact angles are not observed until nano-trees collapse occurs, as will be shown later.

The best performances are given by the 60 Pa samples. In fact, also at the lower thicknesses (that are 0.15 and 1.9 μm) very high contact angles (maximum values observed during measuring are 174.8° for 0.15 μm sample and 179.8° for 1.9 μm)are observed. Samples with higher thicknesses exhibit contact angles of 180°. This means that even after several attempts, the liquid drop was not able to attach to the sample surface during the measurement. Also in this case, performance is improved when island organization is stronger (as will be shown in the following surface analysis) Neverthless, as already said, also 0.15 μm sample shows ultrahydrophobic behavior. The fact that very high contact angles

can be obtained also with very low thickness, as in the case of 60 Pa samples, is high relevance. The first reason is connected to the mechanical properties. In fact, a less thick film may exhibit a lower aspect ratio and then an higher resistance to fracture than the thicker ones [65]. The second reason is simple: a less thick film is faster to fabricate. Since the thickness film linearly depends on the laser pulses number, fabrication time and then the connected costs of 0.1 μm samples could be much smaller than those of thicker films. Finally, as will be shown later in optical analysis section, samples of very low thickness exhibit higher optical transmittance which is among of the most important requirements in self-cleaning glass design.

In conclusion, 10 Pa samples exhibit very low contact angles due to the absence of islands organization. On the other hand, this effect is saturated in 60 Pa samples and for this reason they exhibit the highest contact angles. Samples deposited at 20 Pa and 40 Pa exhibit an intermediate behavior and the dependence of contact angle from thickness is not well defined.

4.1.3 Hysteresis and roll-off contact angles

As discussed in Chapter 1, in order to charactierize a superhydrophobic surface not only the static behavior but also the dynamic has to be considered. One of the most used technique to do this consists of tilting the measuring surface, inducing drop motion and then measuring the advancing and receding contact angle as a function of tilting angle. The hysteresis contact angle is defined as the difference between the two angles an instant before the drop rolls off the surface and gives informations about the liquid adhesion on it. Since only 60 Pa samples of with 0.15, 1.9, 4.8, 11 and 15 μm exhibit roll off (Table 4.1), hysteresis contact angle data are available just for these samples as shown in Table 4.1.

	0.15 μm	**1.9 μm**	**4.8 μm**	**11 um**	**15 um**
10 Pa	*NO*	*NO*	*NO*	*NO*	*NO*
20 Pa	*NO*	*NO*	*NO*	*NO*	*NO*
40 Pa	*NO*	*NO*	*NO*	*NO*	*NO*
60 Pa	*NO*	*24°*	*17°*	*< 3°*	*< 3°*

Table 4.1 *Roll Off Angles for alle the measured samples*

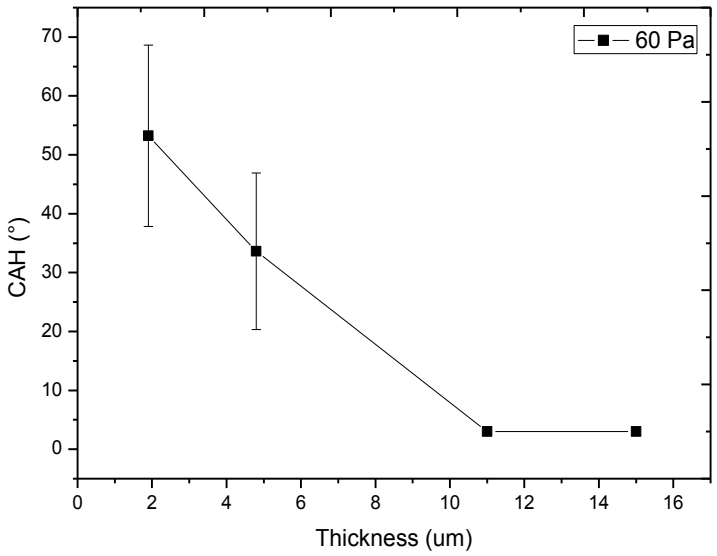

Figure 4.4 *Roll Off angles versus thickness, 60 Pa*

As shown in Figure 4.4, the higher is the thickness the lower is the hysteresis contact angle and then the liquid adhesion to the surface. This fact can be explained by considering
Figure 4.14, where are reported surface ratio (defined as the ratio of solid-liquid interface area over the total interface area) for all the samples. Since thicker samples exhibit lower surface ratios, as will be discussed later, a lower number of chemical bonds are established between liquid and surface and this means a less adherent drop. Due to very low adhesion, drop is kept in motion just by a very weak force and this bring to very low hysteresis and roll off angles. On the other hand, as reported in Table 4.1, the entire series of 10, 20 and 40 Pa and 0.15 μm 60 Pa do not exhibit roll off, even with a surface inclination of 180°. The high liquid adhesion observed in these cases is justified by higher surface ratio (from 0.85 to 0.99). The solid liquid is now bigger than those obtained in 60 Pa series and this brings to higher resistance to motion and then to higher hysteresis, as shown in where are reported water drops on 90° tilted samples (Figure 4.5(a)10 Pa 3.7 μm, Figure 4.5 (b)20 Pa 3 μm and Figure 4.5 (c)40 Pa 2.7 μm). Even if hysteresis contact angle definition implies that drop rolls off, figure shows big differences between left and right angles (which cannot be defined here as advancing and receding simply because the drop is not able to move), highlighting the strong liquid adhesion which characterize these surfaces.

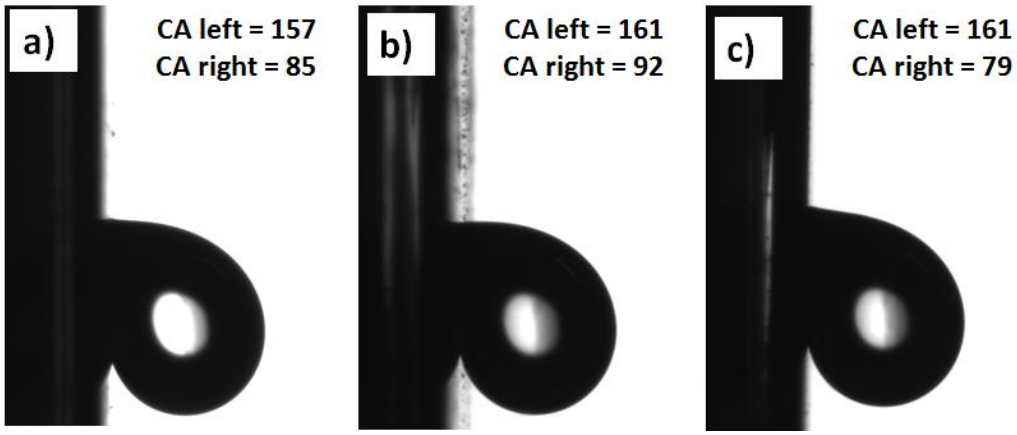

Figure 4.5 *Water drops on 90° tilted 10 Pa 3 μm (a), 20 Pa 3 μm (b) and 40 Pa 2.7 μm*

It is to be noticed that the requirement of high or low adhesion is matter of the application fields wherein the superhydrophobic surfaces have to be involved.
In self-cleaning glass and anti-icing devices design low adhesion is of primary importance. In the first case a liquid drop needs to be less adherent as possible in order that drops pick up the dirt and then easily roll off [66], [67]. In the second case, since pinning of a liquid to the exposed surface is the main reason for the formation of immobilized water droplets and their subsequent freezing on cooled solid substrates [68], anti-icing devices have to be fabricated according to the principle of minimization of hysteresis contact angle. Also surfaces with strong liquid adhesion (but superhydrophobic) can find some applications, for example in the biosensors field where they would be useful for many localized chemical or biological reactions, traced analysis, and in situ detection [69].

4.1.4 Wettability behavior with different liquids

Surface free energy (hereafter SFE) is a quantitative measure of the possible available site for chemical bonding formation. Various methods have been employed to measure SFE The most commonly used methods for SFE calculation during wettability investigation is involving the direct measurement of static contact angle. The wettability results given by different solvents are then fitted by different models depending on the surface properties. Zisman and Fox [70], Fowkes [71], Wu[72], Neumann's equation of state (EOS)[73], and Owens–Wendt–Rabel–Kaelble (OWRK)[74] are the models that can be found in

literature. On the basis of this approach we selected OWRK model being the one more suitable for superhydrophobic surfaces. The equation that relates contact angle with SFE is well known in literature:

$$\gamma_s - \gamma_{sl} = \gamma_l \cos\theta \tag{4. 1}$$

Where θ is the measured contact angle and γ_s is SFE while γ_{sl} and γ_l are the surface tensions at solid–liquid and liquid–vapour interface, respectively. Under the assumption that the relation formulated by Fowkes and co-workers that the SFE (γ_s) is equal to the sum between its dispersive and its polar component (i.e. respectively dipole-dipole forces and polar forces), that is:

$$\gamma_s = \gamma_s^P + \gamma_s^D \tag{4. 2}$$

Owens–Wendt–Rabel–Kaelble developed a standard model also known as Kaeble plot. With model is based on the following linear equation:

$$\frac{\gamma_l(1+\cos\theta)}{2\sqrt{\gamma_l^P}} = \sqrt{\gamma_s^D}\left(\sqrt{\frac{\gamma_l^D}{\gamma_l^P}}\right) + \sqrt{\gamma_s^P} \tag{4. 3}$$

By fitting the above equation and considering:

$$x = \sqrt{\frac{\gamma_l^D}{\gamma_l^P}} \tag{4. 4}$$

$$y = \frac{\gamma_l(1+\cos\theta)}{2\sqrt{\gamma_l^P}} \tag{4. 5}$$

It is possible to retrieve the polar and disperse components of the SFE as the quote and angular coefficient of the interpolating line. Moreover by performing CA measurements with solvent having different surface tension and different ratio between its polar and disperse component it is possible to create a bow-like plot where on the x-axis are found different disperse surface tension and on the y-axis their polar components. The curve in the graphs will design a map that will then predict the contact angles that a liquid with the selected components of surface tension will show on that surface. These curves are here calculated by mean of OWRK plot method [75], [76]for samples deposited at 60 Pa. Solvents with different surface tension and different surface tension components (polar and disperse) are employed to create a complete maps. Worth to note (see Table

4.2) that all the samples displayed high contact angles with all solvents demonstrating an amphiphobic behavior. Wetting envelope lines are reported below in Figure 4.6

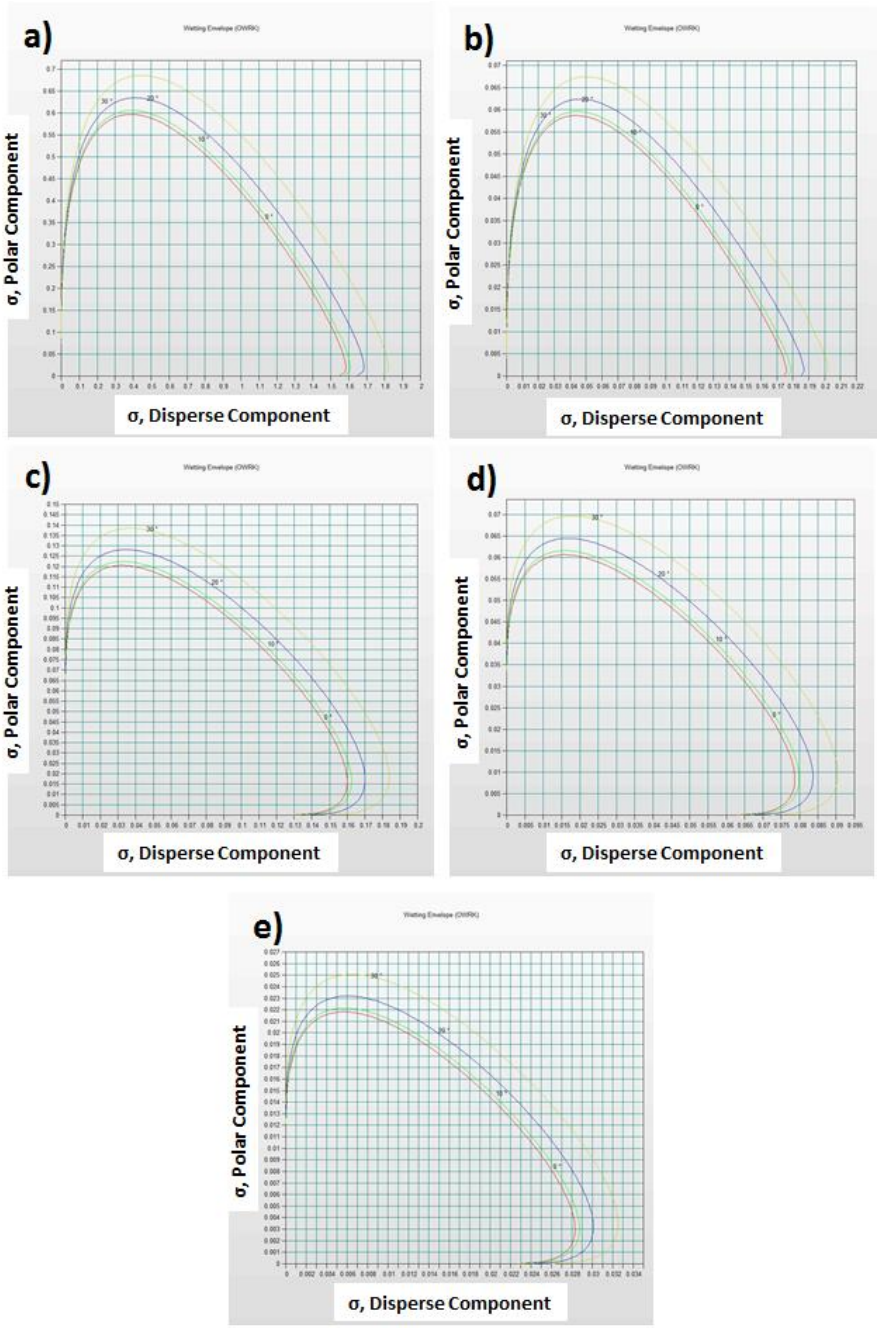

Figure 4.6 *Wetting envelopes for 60 Pa 0.15 µm , 1.9 µm, 4.8 µm, 11 µm and 15 µm*

Deposition Pressure – 60 Pa					
Thickness (μm)	0.15	1.9	4.8	11	15
Chlorobenzen	133.7°	148.7°	152.0°	155.0°	160.7°
Ethylen Glycol	139.9°	158.0°	168.2°	180.0°	180.0°
Ethylen Glycol in H_2O 80%	145.2°	158.8°	180.0°	180.0°	180.0°
Ethylen Glycol in H_2O 50%	154.2°	162.5°	180.0°	180.0°	180.0°
Ethylen Glycol in H_2O 20%	149.2°	164.2°	180.0°	180.0°	180.0°
Water	160.7°	163.3°	180.0°	180.0°	180.0°

Table 4.2 *Static contact angles for 60 Pa samples with different solvents*

4.2 Surface Analysis

4.2.1 10 Pa samples

As shown in the previous paragraphs, sample morphologies change depending on the deposition conditions (pressure and thickness). When islands organization occurs samples exhibit the highest contact angles while very compact films bring to the lowest contact angle. In Figure 4.7 reported SEM images (cross section and top view) of 10 Pa samples all thicknesses. As can be seen none of samples exhibit nano-trees collapse and island organization and this is the reason why the contact angles are very low.

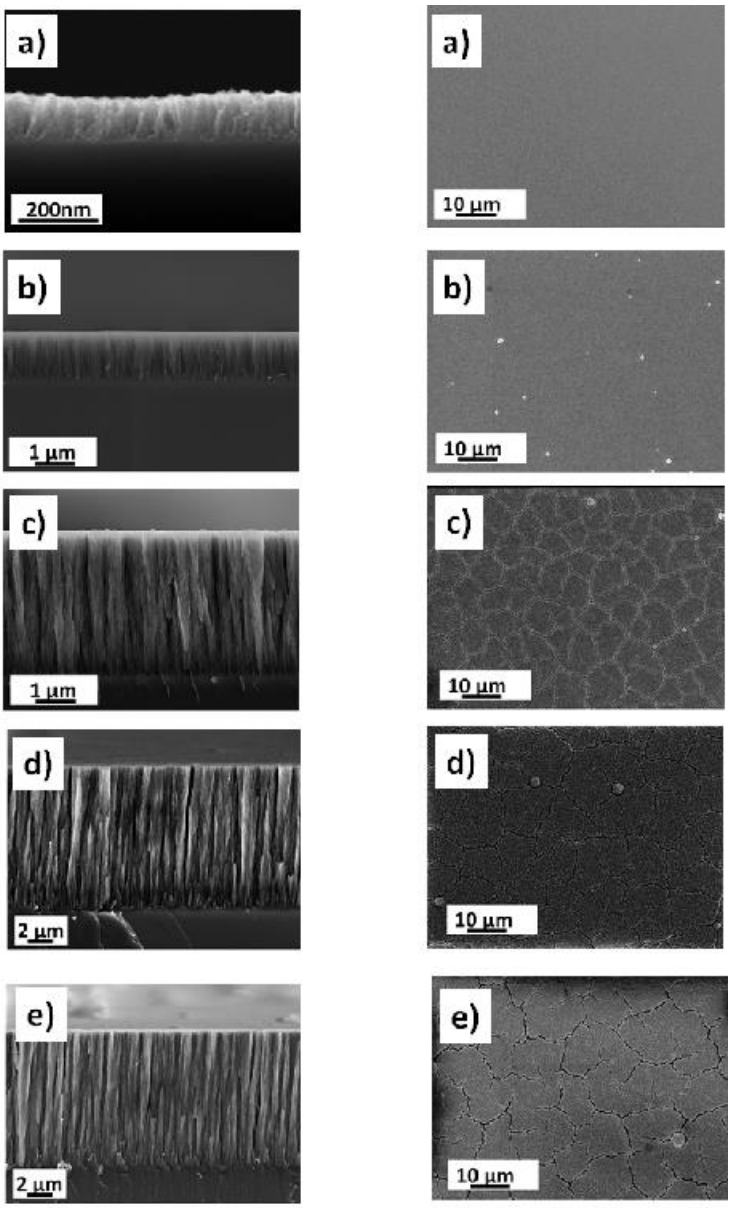

Figure 4.7 *SEM images (cross section and top view) of 10 Pa samples and 0.1 µm (a), 1 µm (b), 3 µm (c), 7 µm (d) and 10 µm (e)*

4.2.2 20 Pa samples

In the case of 20 Pa samples, as can be shown from Figure 4.8, the structures

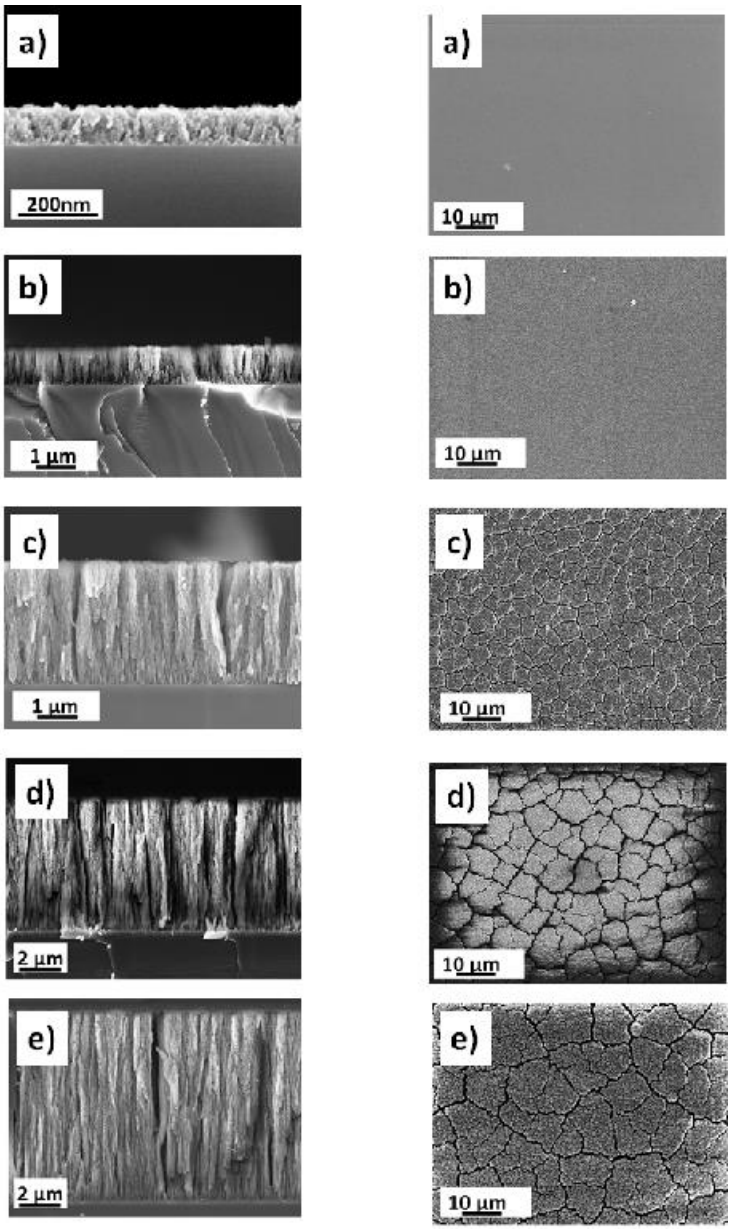

Figure 4.8 *SEM images (cross section and top view) of 20 Pa samples and 0.1 µm (a), 1 µm (b), 3 µm (c), 7 µm (d) and 10 µm (e)*

appear different and a weak collapse starts to be observed. This can be seen both from cross section and top view images. However the effect is very weak and for this reason contact angles are still low, as shown before.

4.2.3 40 Pa samples

As discussed in section 4.1.2 samples fabricated at 40 Pa pressure deposition exhibit superhydrophobic behavior. This fact can be now explained by considering Figure 4.9.

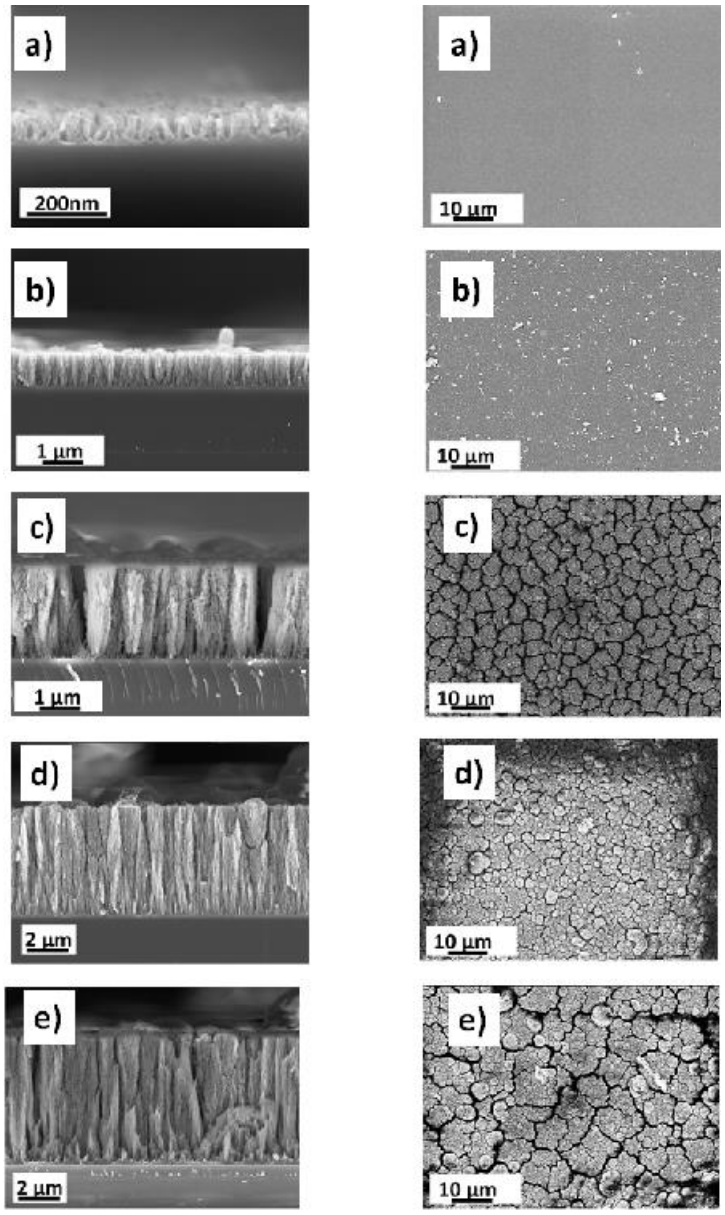

Figure 4.9 *SEM images (cross section and top view) of 40 Pa samples and 0.1 µm (a), 1 µm (b), 3 µm (c), 7 µm (d) and 10 µm (e)*

As can be seen in Figure 4.9 island organization is stronger than the previous samples. This means that the channels between the islands are wider and the islands are more easily recognizable.

4.2.4 60 Pa samples

Finally , in Figure 4.10 are reported the SEM images of 60 Pa samples.

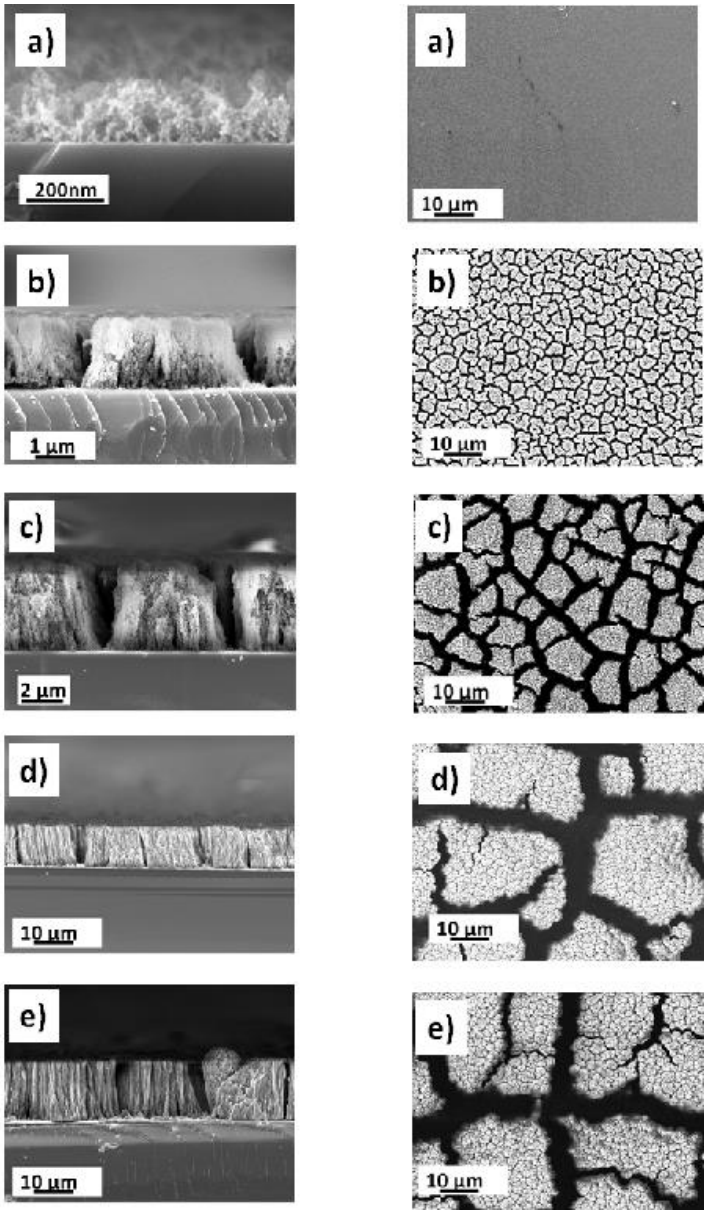

Figure 4.10 *SEM images (cross section and top view) of 60 Pa samples and 0.15 µm (a), 1.9 µm (b), 4.8 µm (c), 11 µm (d) and 15 µm (e).*

Except for the 0.15 μm thick sample, all the 60 Pa samples exhibit nano-trees collapse and island organization. In the case of 1.9 μm islands are not still completely recognizable, they in fact touch each others. By increasing the thickness, island organization is stronger and stronger. This means that islands are bigger and the channels among them are wider. The stronger collapse can be appreciated also from the cross section SEM images. In contrast with the samples fabricated at lower pressure deposition, 60 Pa samples show nano-structures which are more inflected than those seen before. Morevor, although static contact angles exhibit no significant differences, the hysteresis and roll-off angle decreases when island organization is stronger.

4.2.5 Comparison between low thickness samples

In order to better comprehend how the morphology influences the wettability performances, it is now made a comparison between samples of low thickness and different deposition pressure.

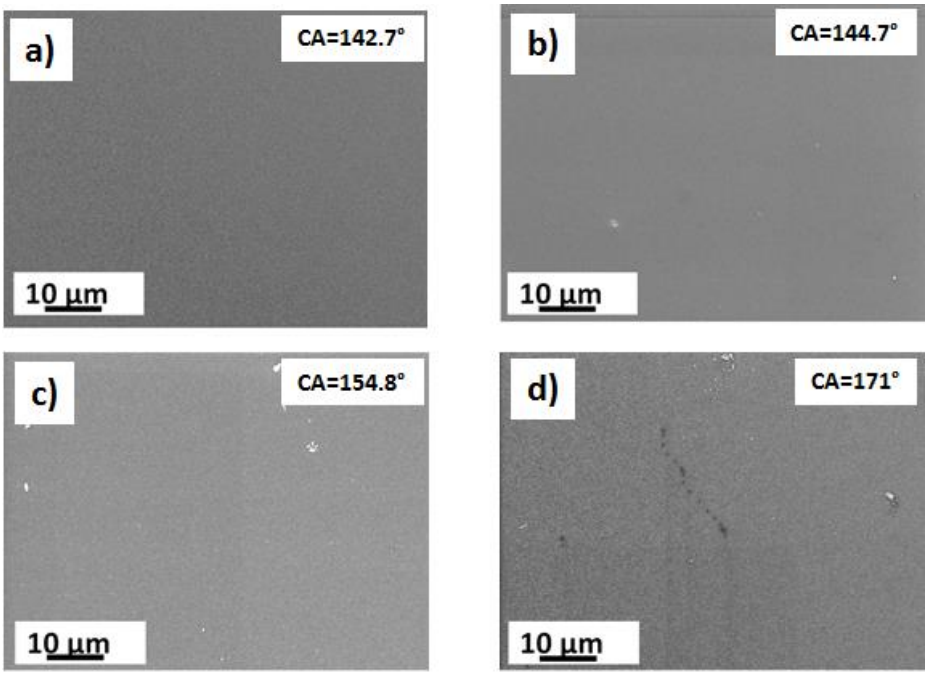

Figure 4.11 *SEM images (top view) of (a) 10 Pa and 0.1 μm (b) 20 Pa and 0.1 μm (c) 40 Pa and 0.09 μm (d) 60 Pa and 0.15 μm.*

Since the stiffness of very low thickness structure is very high nano-tree collapse does not occur and this brings to the lowest contact angles for each pressure series samples. Surfaces appear (SEM images top views available in Figure 4.7, Figure 4.8, Figure 4.9 and Figure 4.10) very compact and nano-trees are not

organized in islands. In any case 60 Pa 0.15 μm exhibit very high contact angle. Finally it turns out that the stronger is the pressure deposition the higher is the contact angle.

4.2.6 Comparison between intermediate thickness samples

Figure 4.12 shows the differences between samples of intermediate thicknesses and different deposition pressure. In this case island organization appears in all the samples but, as can be seen in Figure 4.12, only 60 Pa sample exhibit well defined features and wide channels between them while for the lower pressures island get in touch with each others. This fact turns out in an increase of contact angle when the pressure deposition increases, which is the same trend observed at lower thickness (Figure 4.11).

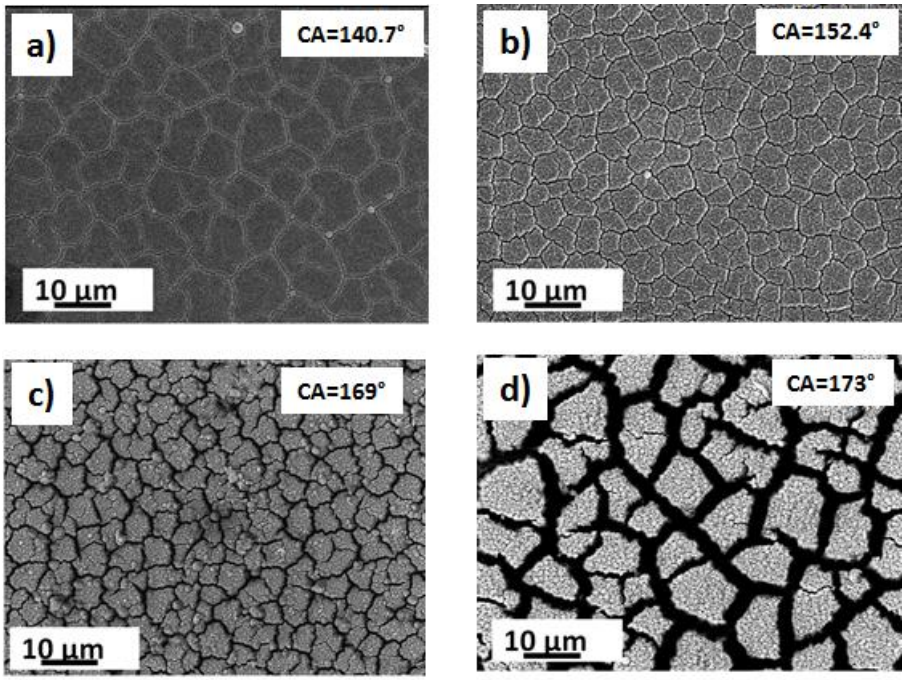

Figure 4.12 *SEM images (top view) of (a) 10 Pa and 3.7 μm (b) 20 Pa and 3 μm (c) 40 Pa and 2.7 μm (d) 60 Pa and 4.8 μm.*

4.2.6 Comparison between high thickness samples

Finally, also samples of high thicknesses are compared, as shown in Figure 4.13. First of all has to be noticed that the size of islands are bigger than those formed in sample of intermediate thickness. Moreover, also in this case, island

organization is stronger by increasing the pressure deposition and this brings, again, to higher contact angles.

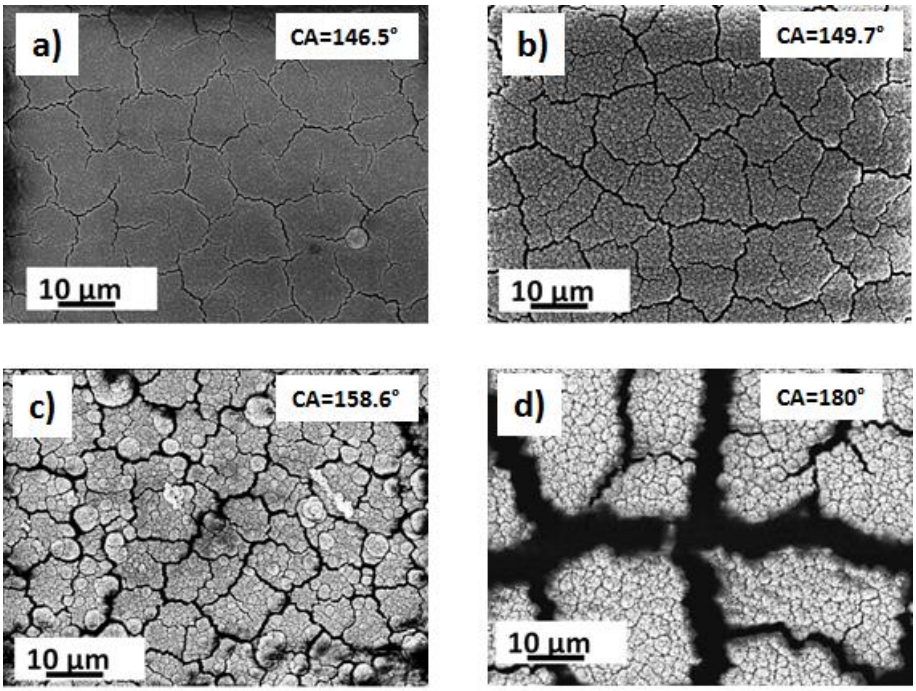

Figure 4.13 *SEM images (top view) of (a) 10 Pa and 11.7 µm (b) 20 Pa and 10 µm (c) 40 Pa and 7 µm (d) 60 Pa and 15 µm.*

4.2.7 Surface Ratio

In order to quantify the island organization is useful to consider the surface ratio, defined as the fraction of the solid-liquid interface at the drop-surface contact base [19]. The surface ratios have been calculated (see Chapter 2) for all the samples considered, the results are summarized in Figure 4.14**.**

Data show that for very low thicknesses (0.1 µm), deposited films are very compact and the collapse and the following islands organization do not occur at all the deposition pressures. This can be explained considering the fact that for TiO_2 nano-trees with very small height , the stiffness is high and they are not flexible. For samples deposited at 10 Pa, films are very compact and the collapse does not occur also when the highest nano-trees should exhibit the lowest stiffness (that is in the case of 10 µm thick sample), as shown in the SEM images of Figure 4.15 , both in the cross section and top view.

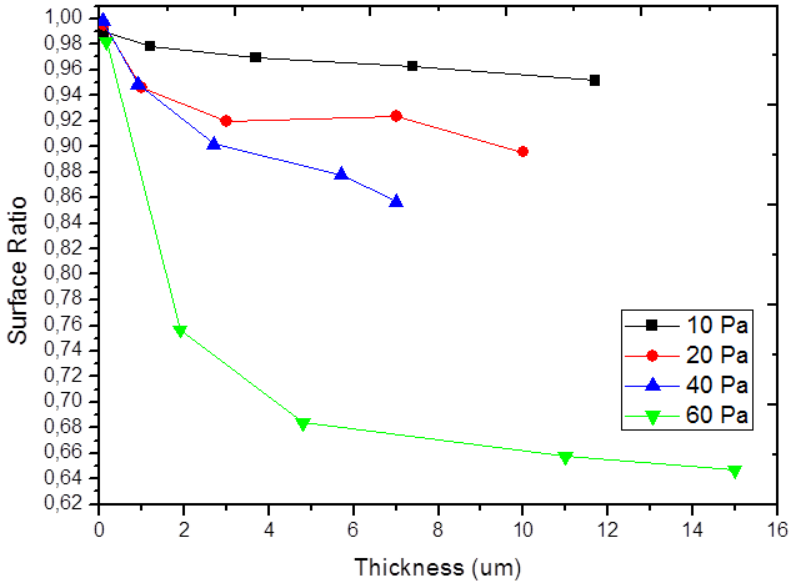

Figure 4.14 *Surface Ratio for all the pressure deposition and thicknesses*

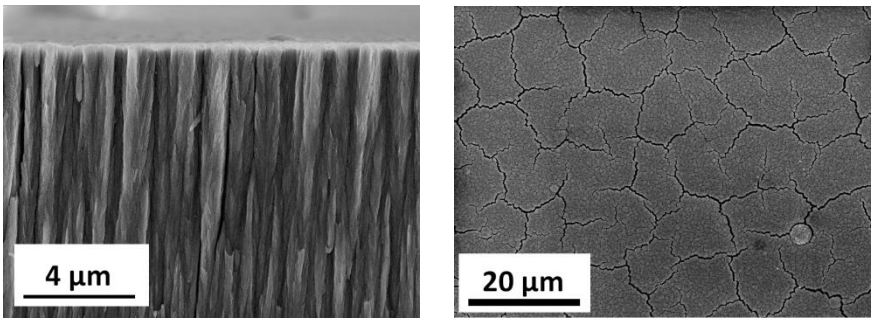

Figure 4.15 *SEM images (cross section and top view) of TiO2 film, 10 Pa and thickness 10 um*

As it can been seen both from and Figure 4.15, surface ratio is very high also at the highest thickness. The values in fact vary from 0.98 to 0.95.For 20 and 40 Pa samples, surface ratios are different for thickness higher than 1 µm but in general island organization is not pronounced also for higher thicknesses (7,10 µm), as shown in Figure 4.16 .

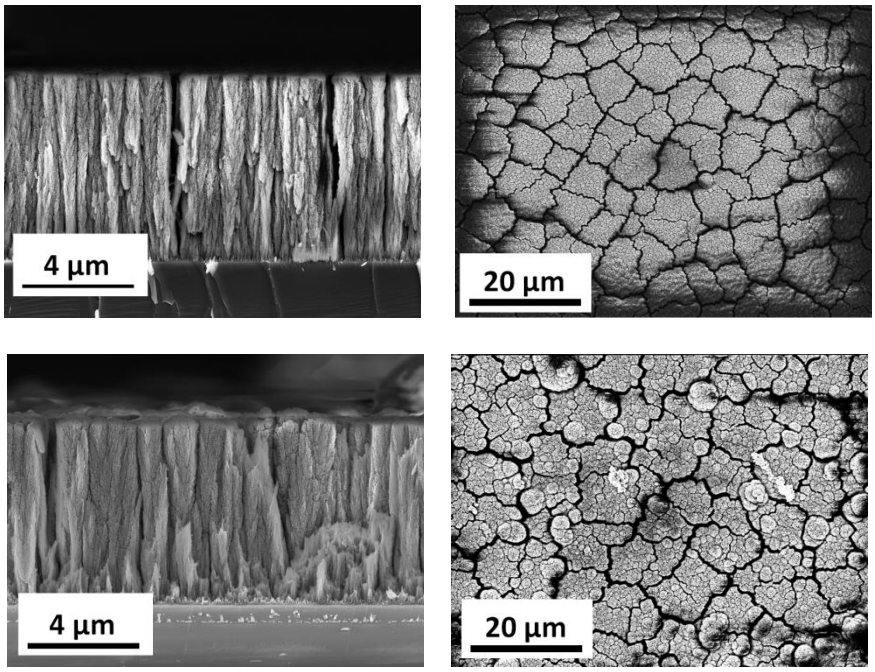

Figure 4.16 *SEM images (top view and cross section) of 20 Pa and thickness 7 µm (above), 40 Pa and thickness 7.4 µm (below).*

Although the top view images shows islands reasonably well defined, cross section images highlith that actually the nano-trees collapse is not clear. For this reason surface ratio decreases but is only about 0.85. The surface ratio values for 20 and 40 Pa in fact vary from 0.99 to 0.85.

In order to gain the best wettability performance, that means static contact angles higher than 175° and roll-off angle lower than 3°, surface ratio values have to be lower. This happens in the case of 60 Pa samples where surface ratio value is 0.65 for 15 µm thick film. Since the nano-trees stifnesses are now very low, the nanostructures collapse occurs very easiliy also in 1 µm thick film, as it is shown in Figure 4.17. As previously shown in Figure 4.10, the islands size increases with thickness and at the same time channels and cracks formed formed during the drying process become wider, as shown in Figure 4.17.

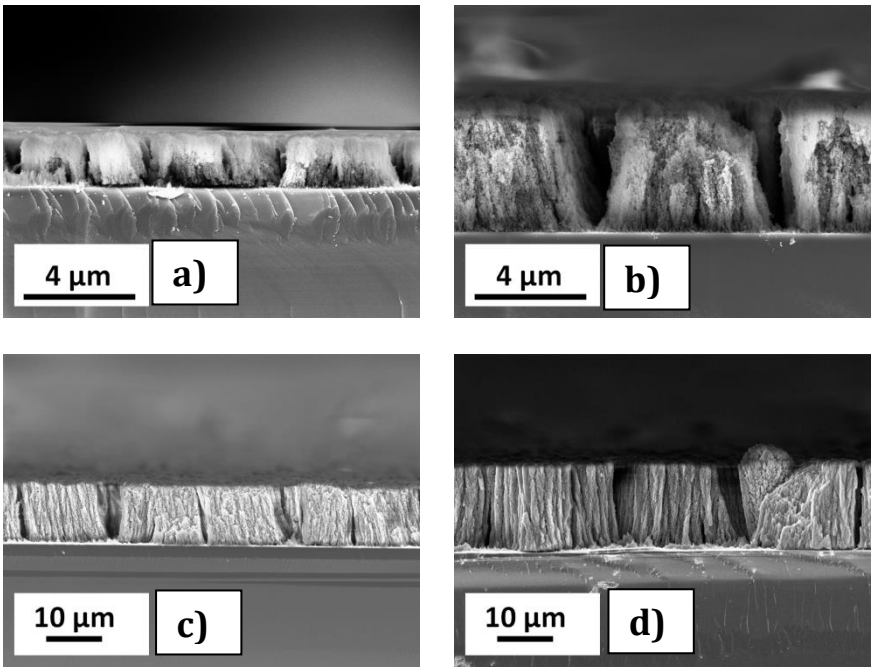

Figure 4.17 *SEM images (cross section) of TiO2 PLD film (60 Pa, thickness (a)1.9, (b)4.8, (c)11 and (d)15 µm)*

4.2.8 Nano-roughness

As previously discussed, the superhydrophobic behavior is given by two factors: low surface energy and dual or multiple scale of roughness [62]. As shown in previous sections, surface ratio explains much of the dependences between contact angles (both static and dynamic) and surfaces morphology but in order to take into account the effects given by the nano-scale, also nano-roughness measurements have been performed. The measurements have been done on same thickness (3 µm) samples fabricated at different pressures (10, 20, 40 and 60 Pa). Also the most performing sample (60 Pa, 15 um) was analyzed.

In Figure 4.18 are reported AFM images (500 nm x 500 nm) from which roughness values have been obtained while in Figure 4.19 are reported the results. As it can be seen both from the AFM images and plot of R_{rms} the higher is the deposition pressure, the higher is the nano-roughness and this is in accordance with static contact angle values (Figure 4.3). Moreover Figure 4.19 shows that R_{rms} depends also from the AFM image area (and then from the side length of square area analyzed, which is the parameter reported in the plot) from which roughness was obtained and this can been explained by considering

the fact that increasing the observation area the geometrical features that distinguish one sample from the others can be appreciated.

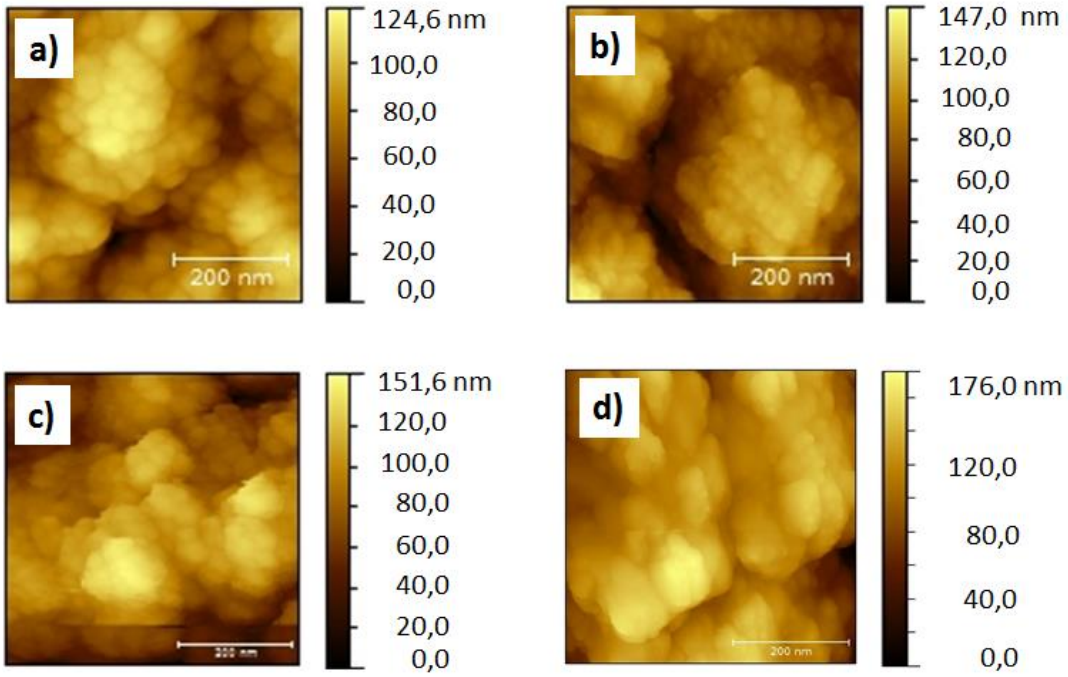

Figure 4.18 *AFM images of 10 Pa, 3 um (a), 20 Pa, 3 um(b), 40 Pa 3um(c) and 60 Pa 3 um (d).*

Figure 4.19 shows that at the lowest surface area (which means 10000 nm^2, or 100 nm side length) 10, 20 and 40 Pa do not exhibit significant differences and the values are very low (4.84±1.33 nm for 10 Pa 3 µm, 6.31±1.70 nm for 20 Pa 3 µm, 6.41±1.74 nm for 40 Pa 3µm and 9.31±4.56 nm for 60 Pa 3 µm). By increasing the scale of AFM image both mean values and standard deviations increase and significant differences between samples can be now appreciated. At 500nm (which means a square image area of 250000 nm^2) the R_{rms} values are 16.66 ±2.01 nm for 10 Pa 3µm , 25.75±9.16 nm for 20 Pa 3 µm, 28.225±12.67 nm for 40 Pa 3µm and 33.78±21.94 nm for 60 Pa 3 µm).

As can be seen at these scales, samples fabricated at different pressure deposition exhibit different nano-roughness, more precisely the higher is the pressure deposition the higher is the nano-roughness (as also shown in Figure 4.18). Actually the differences become appreciable at scales higher than 400 nm but also in these cases values are similar. Moreover 10 Pa 3 µm exhibit a weak increase of R_{rms} also at higher scales and this is probably due to high compactness of substrate under this conditions. When substrates become more

porous, as in the case of e 20, 40 and 60 Pa the dependency of R_{rms} from AFM image area is more pronounced.

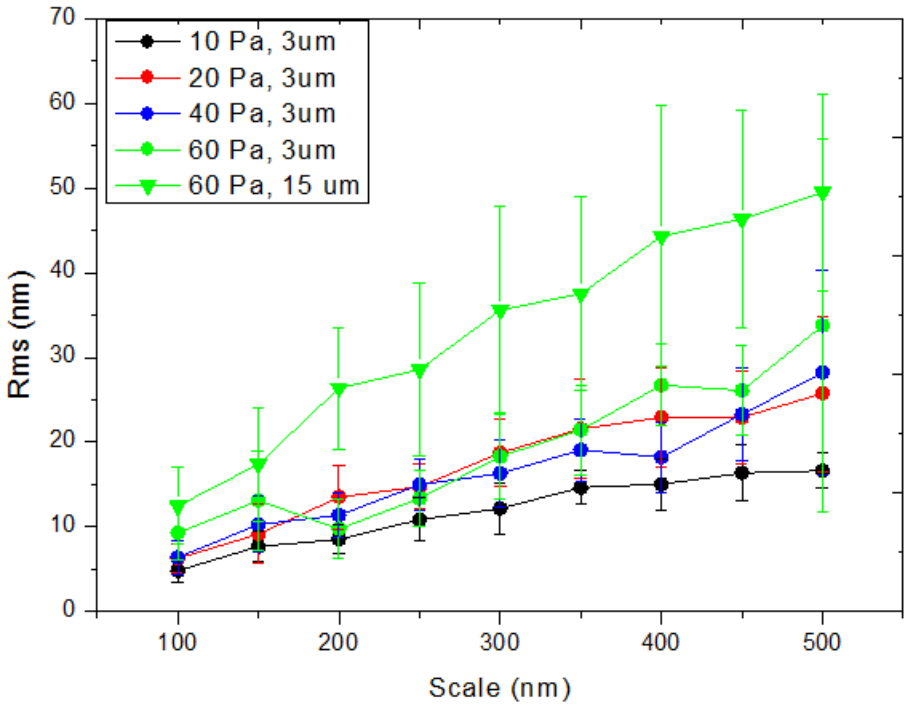

Figure 4.19 *Root Mean Square Roughness for 3 µm samples at different pressure deposition (10, 20, 40 and 60 Pa) and best performing sample (15 µm).*

In Figure 4.19 is also reported the R_{rms} for the most performant sample, which is the 60 Pa 15 µm according to the contact angle measurements (both static and dynamic). As can be seen 60 Pa 15 µm sample exhibit a much higher R_{rms} both than 10, 20 and 40 Pa samples and also than 60 Pa 3 µm. This fact can be observed over the entire range of AFM image area scales. More precisely, at the lowest surface area (which means 10000 nm^2 or 100 nm side length) R_{rms} value is 12.47±4.56nm while at the highest surface area (which means 250000 nm^2 or 500 nm side length) R_{rms} value is 49.47±11.58 nm. Figure 4.20 shows the nano-morphological differences between two samples at highest surface area measured. As it can be seen also from these images, the higher is the nano-roughness, the higher is the wettability performance. In fact, even if both 60 Pa 3 µm and 60 Pa 15 µm samples exhibit highest static contact angle, roll off angle are different. In the first case (3 µm) roll-off angle is 24° while in the second case (15 µm) roll-off angle is lower than 3°.

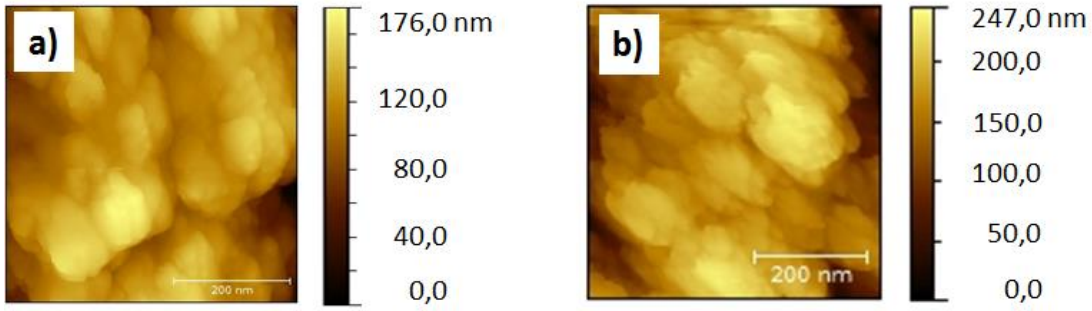

Figure 4.20 *AFM image comparison between 60 Pa 3um (a) and 60 Pa 15 um (b)*

Also standard deviation gives informations about the morphology, in fact the more heterogeneous is the surface the higher is standard deviation of roughness and this is in accordance whith what have been observed. In fact, when the pressure deposition is high, as previously discussed, the nanostructured film is more porous while at lower pressure the film is more compact and less heterogeneous. The highest standard deviations are actually exhibited by 60 Pa 15 μm and this is probably due to the effect of islands organization which is much stronger for higher thickness samples. In fact, due to islands organization, surface appears much less homogenous and this brings to higher standard deviations.

4.2.9 Grain size

In addition to nano-roughness by AFM image analysis, in order to better characterize the nano-scale morphology and to understand how it impacts on wettability behavior also the dependency of contact angle from the grain size effect has been investigated.

It is known in literature [77],[78] that by increasing annealing temperature it is possible to crystallize and in turn tune the grain size of films of TiO_2 deposited by PLD [79]. Higher temperatures lead to a larger grain size and therefore to a change in the surface roughness. The effect of the thermal treatment is studied on the wettability properties of a set of 3μm thick films deposited at a background pressure of 40Pa and sensitized with PFNA molecules solution. XRD analysis (whose spectra are reported in Figure 4.21) is used to gain insight of the grain size τ (defined as the dimension of the *leaves of the nanotrees*) through the peak analysis with Scherrer equation:

$$\tau = \frac{k\,\lambda}{\beta\,\cos\theta} \tag{4.6}$$

where *k* is a dimensionless shape factor, with a value close to unity, λ is the X-ray wavelength, β is the line broadening at half the maximum intensity (FWHM) and θ is the Bragg angle.

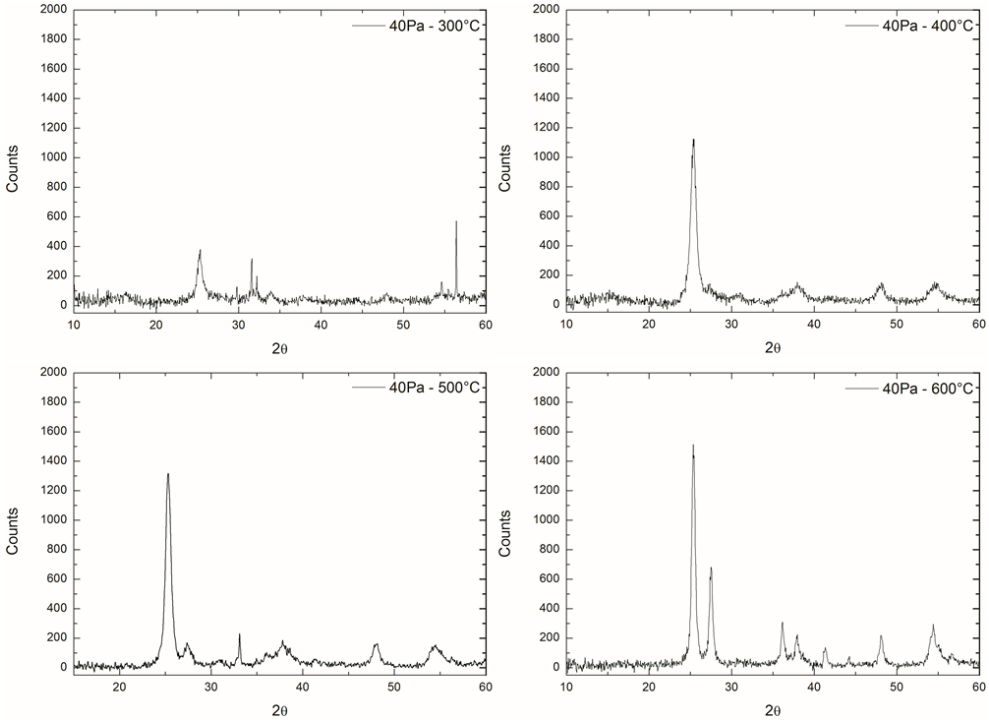

Figure 4.21 *XRD spectra for 40 Pa 3 um thick samples annealed at 300,400,500 and 600 °C*

In Figure 4.22 it is shown the dependency of contact angle with the grain size. By increasing the grain size the surface loses gradually its roughness and therefore reducing its hydrophobic behavior.

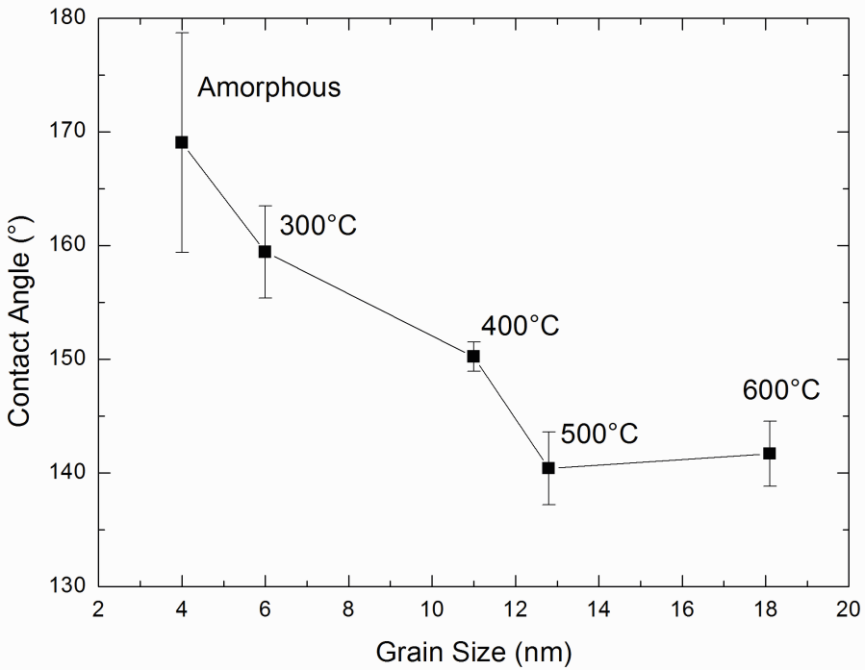

Figure 4.22 Dependency of contact angle with the grain size

4.3 Optical properties

Since one of the most appealing fields where superhydrophobic surfaces can find application is the self-cleaning glass industry, also optical analysis have been performed. In order to do this TiO_2 has been deposited not only over silicon substrates but also over glass slides. Figure 4.23 exhibit the total transmittance spectra for the 60 Pa samples, which are the most performing from the wettability point of view. As can be seen in Figure 4.23 total transmittance is strongly dependent from the film thickness; the higher is the thickness the lower is the total transmittance and this can be easily explained by considering the higher photons absorption in thicker films. Even if the highest wettability performance (CA=180°, CAH<3° and Roll-off angle <3°) is given by thicker films, the better optical properties (high transmittance) are given by the lower films, as shown in Figure 4.23. Total transmittance values vary from 91.14% at 800 nm to 94% at 530nm in the case of 60 Pa 0.15 μm and from 90% at 400 nm to 93.6% at 565 nm in the case of 60 Pa 1.9 μm.

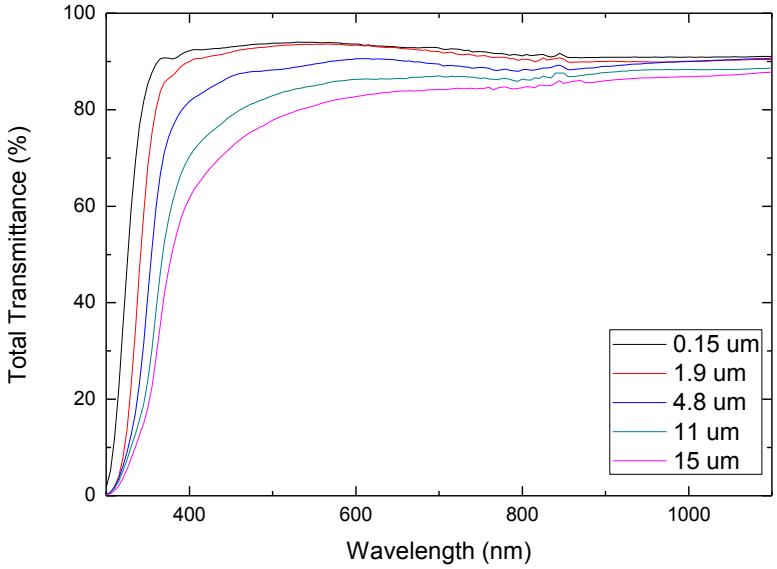

Figure 4.23 *Total transmittance spectra in the UV-Vis for 60 Pa samples*

Besides the total transmittance spectra, also diffused transmittance spectrum has been measured, as shown in Figure 4.24.

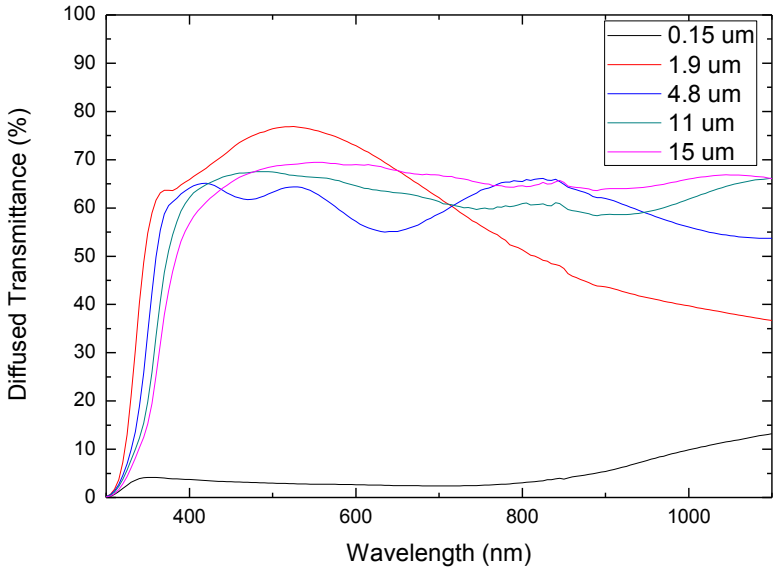

Figure 4.24 *Diffused transmittance spectra in the UV-Vis for 60 Pa samples*

Figure 4.24 shows that only 0.15 μm exhibits very low diffused transmittance (values vary from 2.39% at 700nm to 3.72% at 400nm). This means that even if the total transmittance is high also for thicker samples, only the 0.15 μm does not exhibit opacity, as shown in Figure 4.25(a). As it can be seen, are reported an untreated glass slide (on the left) and a superhydrophobic glass slide (on the right). As Figure 4.25(a) shows standard glass tends to absorb the water (the color blue is just given by a marker in order to facilitate the visualization) while the liquid drop (volume 24 μl) over the superhydrophobic surface tend to assume a spherical shape.

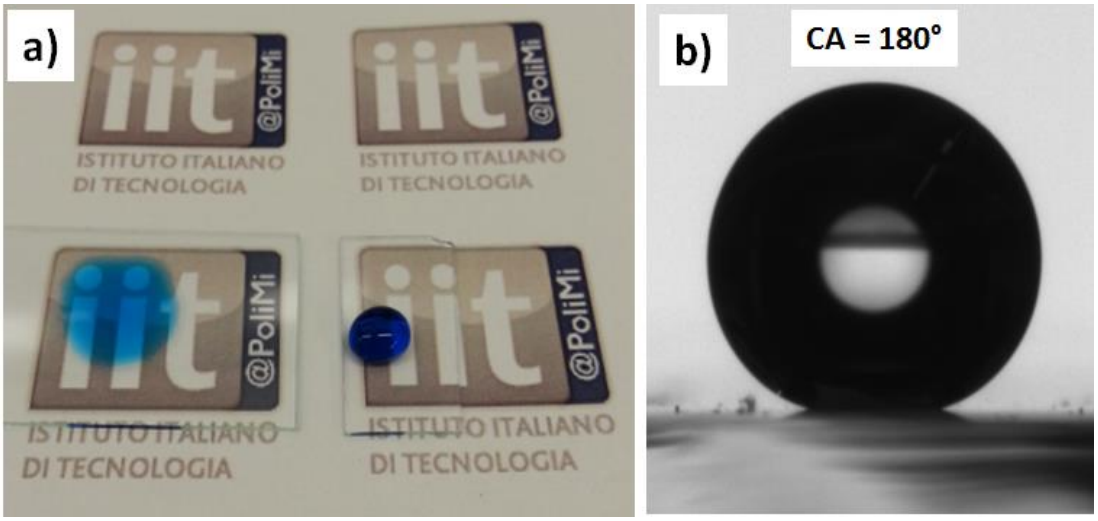

Figure 4.25 *(a) Differences between an untreated and a superhydrophobic glass (b) 4 ul droplet on superhydrophobic glass*

Figure 4.25(b) shows a 4 μl volume droplet over a glass coated by superhydrophobic film fabricated at 60 Pa deposition pressure a 0.15 μm thick. As shown, measurements exhibited a maximum contact angle of 180°.

Chapter 5

Conclusion and Outlook

5.1 Discussion

In the forties two important wettability models for real surfaces were developed. The first, developed by Cassie and Baxter in 1944 [11], explains the behavior of a liquid droplet which only contacts the solid surface at the top of its protrusions. The second, developed by Wenzel in 1949 [10], explains the behavior of a liquid droplet which is impregnated into the micro and nano grooves present at the surface. Both models predict that a real surface with a proper roughness could be extremely repellent to water or other liquids. They therefore mathematically described the behavior of superhydrophobic surfaces.
In the last two decades several studies have been published on superhydrophobic surfaces, simultaneously with the growth and development of nanotechnology. Firstly scientists and engineers started to study some bio-surfaces which exhibited superhydrophobic behavior and found out that all samples exhibited a dual scale (micron and nano) hierarchical structures [1], [38], [41].

In order to investigate the role of multiscale roughness in the so called "Lotus effect" also numerical analysis have been performed [18], [62]. Marmur *et al.* [62] have studied three 2D different types of surface topographies with up to four roughness scales, as shown in Figure 5.1. The surface considered were sinusoidal, flat-top pillars and triadic Koch curve which is a simple example of a fractal [80]. Even if for flat-top pillars surfaces the contact angle changes are not monotonous they found that sinusoidal and triadic Koch surfaces exhibit higher contact angles when the number of roughness scales increases, as shown in Figure 5.2 For these cases they also found that by increasing the number of roughness scales, Cassie-Baxter state becomes the stable state.
In the present work, the effect of different scales on the wettability behavior of synthetic surfaces have been studied. A detailed analysis of the micro-scale morphology by means of SEM images and a purposely developed imaging

processing software has been performed. On the other hand, the nano-scale revealed to be comprising many hierarchical subscales. A preliminary analysis by means of HRSEM, AFM and XRD has been undertaken, but a much more detailed study is necessary in order to reveal such a wealth of nested scales and their interplay in defining the wettability character of a surface.

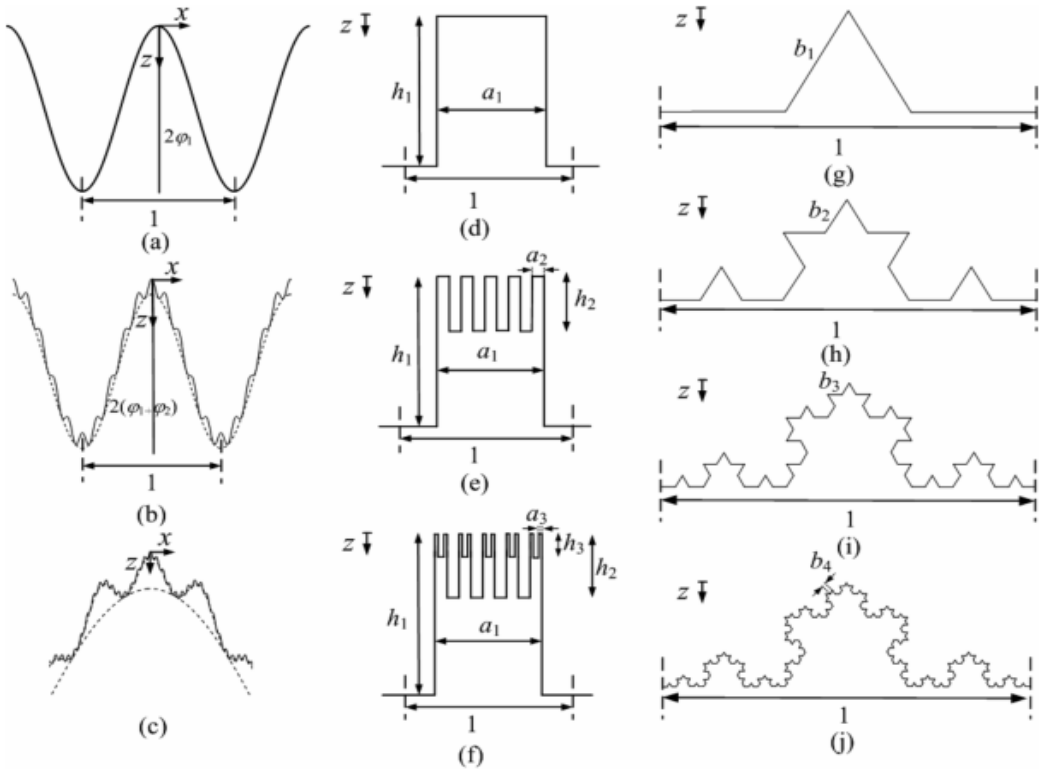

Figure 5.1 *Unit cells of solid two-dimensional surface topographies. Three levels of roughness scales of a sinusoidal surface topography are shown in a–c) (in (c) the picture is magnified compared with the others). Three levels of roughness scales of* [62]*flat-top pillars are shown in (d–f). Four levels of roughness scales for surfaces made of triadic Koch curves are presented in (g–j)*

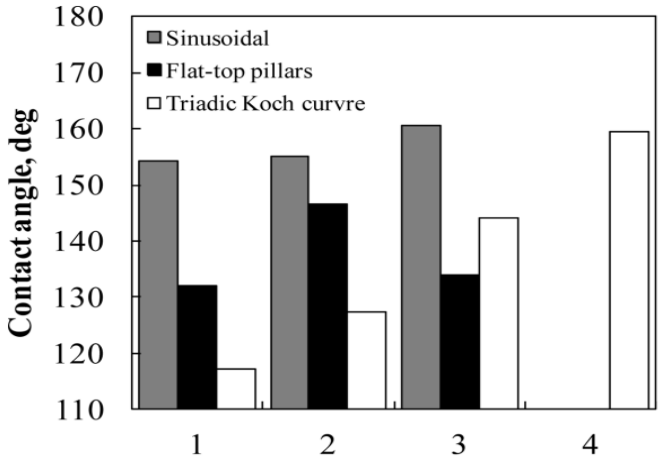

Figure 5.2 *Contact angles dependency from number of roughness scales for sinusoidal, flat-top pillars and triadic Coch surfaces*

The quantity which described the morphological feature considered at the micro scale is the surface ratio, defined as the ratio of solid-liquid interface area over the total interface area. In Appendix A details on how it was calculated are. By fixing the same scale for all the analyzed samples it has been possible to appreciate considerable differences in terms of surface ratio also between samples fabricated at the same pressure deposition as shown in Figure 5.3 where are reported SEM images (top view) of 60 Pa 0.15 μm and 60 Pa 15 μm with the corresponding surface ratio values.

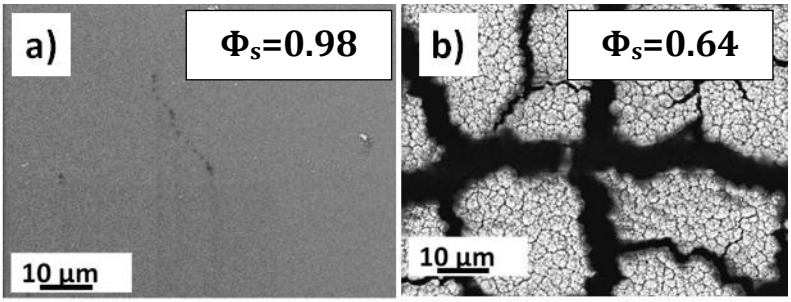

Figure 5.3 *SEM images (top view) of 60 Pa 0.15 μm (a) and 60 Pa 15 μm (b).*

In Figure 5.3, 60 Pa 0.15 μm appears homogeneous surface while 60 Pa 15 μm exhibit well defined islands with wide channels between them.

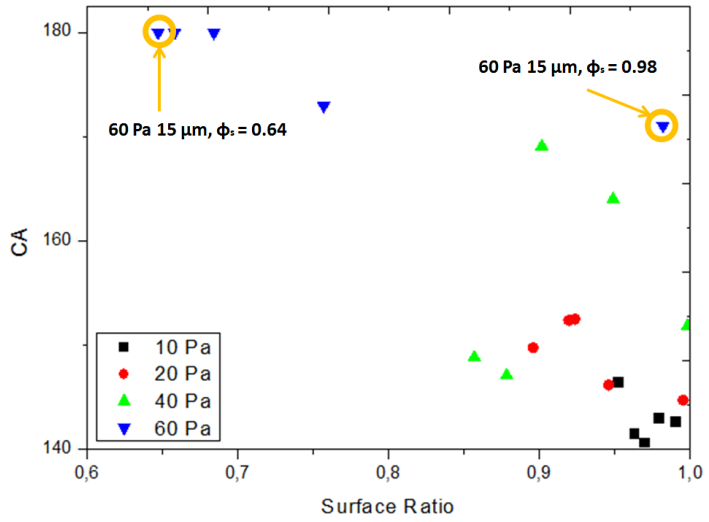

Figure 5.4 *Contact angles dependency from surface ratio for different pressure deposition*

Nevertheless, both samples exhibit very high contact angles (as shown in Figure 5.4, where have been also reported contact angles measurements for all the other samples). This means that surface ratio calculated just at the micro scale is not sufficient to describe the wetting behavior, as demonstrated by the trend not completely defined of Figure 5.4. This fact is evident by considering also the Cassie-Baxter equation:

$$\cos \vartheta^{*}_{CB} = -1 + \phi_s\left(1 + r_f \cos \vartheta\right) \tag{1.6}$$

and re-write it in respect of the surface ratio ϕ_s :

$$\phi_s = \frac{\cos \vartheta^{*}_{CB} + 1}{1 + r_f \cos \vartheta} \tag{5.1}$$

If measured contact angles and a roughness factor values are substituted in Equation 5.2, the resulting ϕ_s value is much different from those have been calculated. For example, by considering 60 Pa 0.15 µm sample which exhibits a measured contact angle of 171°, a Young contact angle of 85° and a typical roughness factor per unit thickness (defined as ratio of the actual wetted area to the projected area) of 60 μm^{-1} (as measured by Passoni *et al* in a recent work not already published), Equation 5.2 returns a ϕ_s of 0.0019 which is two orders of magnitude lower than the Φµm measured in this work, that is 0.98. Actually, even if the sample exhibits a surface ratio lower than one, this value is very high and for this reason the surface should be considered, at the micro scale, as

compact and without voids. If it is considered a more significant sample, for example 60 Pa 1.9 μm (with contact angle of 173°, Young contact angle of 85° and roughness factor of 760 μm^{-1}), Equation 5.1 gives a ϕ_s of 0.00011 which is totally different from a surface ratio of 0.75 measured in this work in Chapter 4.

We believe that this discrepancy is due to the fact that the nanoscale has a rich topography that significantly lowers the effective surface ratio "felt" by the liquid drop. As an example, Figure 5.5 shows SEM images of the sample grown at 60 Pa, 0.15 μm thick, at different scale of magnification. Even if at low magnification the sample appears compact and homogeneous, a closer look reveals that actually it exhibits lot of superficial voids and protrusions.

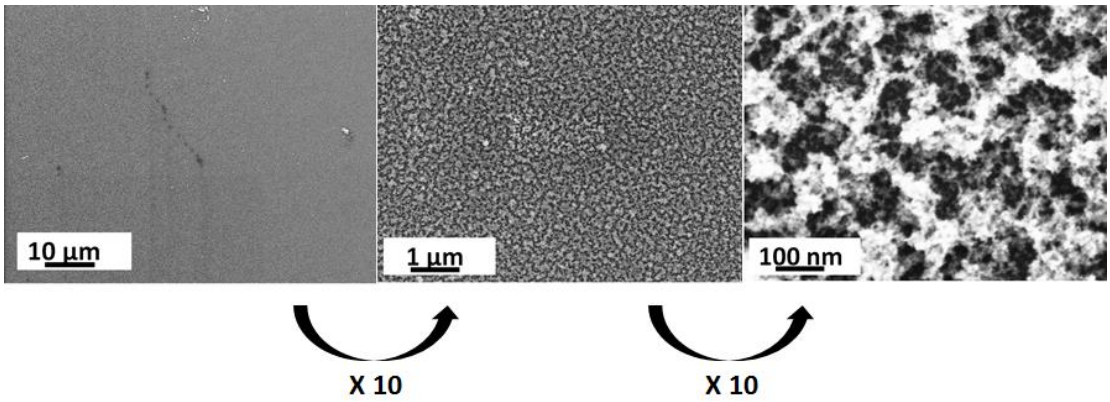

Figure 5.5 *SEM images (top view) of 60 Pa 0.15 μm at 5000X, 50000X and 500000X*

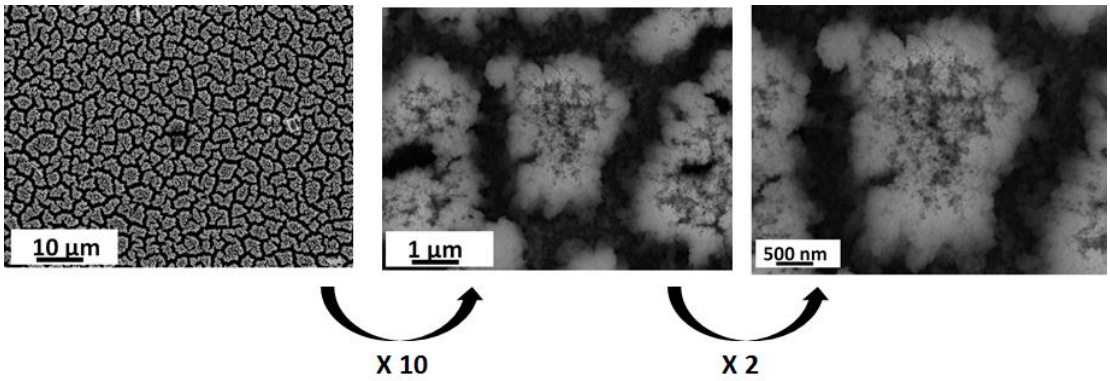

Figure 5.6 *SEM images (top view) of 60 Pa 1.9 μm at 5000X, 50000X and 100000X*

This effect can be obviously seen also for those samples that exhibit surface ratio considerably lower than one also at the smallest magnification scale, as in the

case of 60 Pa 1.9 μm (Figure 5.6). It has to be said that the physical origin of geometrical aspects at micro and nano scale are totally different. At the micro scale (studied by SEM images analysis) they are governed by islands while at the nano scale they depend on how the grains agglomerate with each others and on their size. Then, the real surface ratio may be defined by considering the contributions of both the roughness scales (micro and nano), as described in Equation 5.3:

$$\phi_h = \phi_{\mu m}\phi_{nm} \tag{5.2}$$

where ϕ_h indicates the real surface ratio, recalled *hierarchical surface ratio* while $\phi_{\mu m}$ (which is the same of those surface ratios calculated in the Chapter 4) and ϕ_{nm} represent the *micro-surface ratio* and *nano-surface ratio* respectively. As the AFM analysis showed in Chapter 4, these kind of surfaces exhibit, at the nanoscale, an irregular profile with several grooves and peaks. Moreover, a further scale exists: the particle/grain size. This is difficult to access (except by using a TEM) when the elemental constituents of the surface are amorphous, but become apparent when crystallization is induced by thermal treatment. In one case, we showed how an increasing grain size yields a diminishing contact angle. For these reasons the *nano surface ratio* considered above should be much smaller than one and this brings to very low *hierarchical surface* ratio. Actually, it would be more correct to talk about different *nanoscales* and different nano-surface ratios. Assuming that this kind of surfaces exhibit a quasi self-similarity[50], ϕ_{nm} may be expressed as:

$$\phi_{nm} = \prod_{i=0}^{M_{min}} \phi_i \tag{5.3}$$

where M_{min} denotes the lowest scale, in the sub-micrometric range, at which it is possible to define a surface ratio ϕ_i. As can be seen from Equation 5.3, the higher is the number of roughness scales which a surface exhibit, the lower is the *nano surface ratio*. For example, considering again the 60 Pa 0.15 μm, which exhibits a $\phi_{\mu m}$ of 0.98, and assuming a ϕ_i of 0.3 at four different scales, the *hierarchical surface ratio* ϕ_h is 0.0079. This value is of the same order of magnitude of 0.0019, which is the ϕ_s value predicted in the previous example (pag. 82). The same calculations on 60 Pa 1.9 μm gives a *hierarchical surface ratio* of 0.006, which is very close to the predicted value in the previous example (pag 82.).

Even if these considerations represents just an attempt to investigate the relationships between wettability phenomena and surface morphologies, they highlight the importance of multiscale roughness to achieve superhydrophobic behavior. Moreover they suggest that further investigations are required in

order to properly quantify the surface ratios at different scales (Figure 5.7) and, by combining the results with fractal models, compare the experimental data with theoretical models [11], [62].

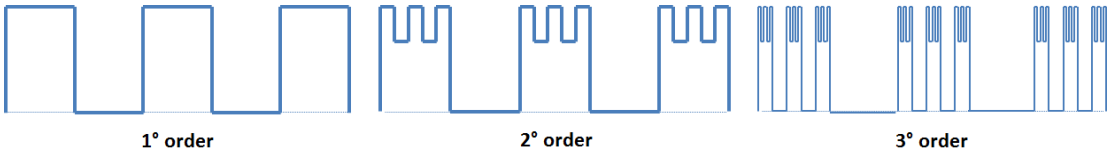

Figure 5.7 *Three levels of roughness scales of a flat-top pillars surface topography*

5.2 Outlook

Wettability studies have been performed on TiO_2 superhydrophobic surfaces sensitized by perfluorononanoic acid solution. By changing the fabrication process, that means pressure deposition, thickness film and dipping time of sensitization process, different behavior have been observed, as show the wide range of measured contact angles. More precisely:

- samples fabricated at 10 Pa and 20 Pa deposition pressure exhibit hydrophobic behavior;
- samples fabricated at 40 Pa deposition pressure exhibit superhydrophobic behavior;
- Samples fabricated at 60 Pa deposition pressure exhibit an ultrahydrophobic behavior with contact angles higher than 175°.

Also dynamic contact angles and roll-off angle have been measured. Only the 60 Pa samples exhibit roll-off while for the other pressure samples water droplets are strongly adherent also at tilting of 180°. From the SEM image analysis finds out that a fundamental request to achieve ultrahydrophobic behavior is the nano-trees collapse and island organization. In order to better characterize the surfaces, static contact angles have been performed also with different liquid than water, demonstrating an amphiphobic behavior.

UV-Vis spectroscopy measurements have shown good optical properties only for the thinnest sample. However, even if the best sample (from a wettability point of view) is the 60 Pa thickest sample also the thinnest one exhibit contact angle higher than 170°.

Surface analysis have been performed. From SEM image processing, surface ratios have been calculated for all the sample fabricated in the experiments. Measurements find out that:

- the higher is the deposition pressure the lower is the surface ratio;
- the higher is the film thickness the lower is the surface ratio.

In order to investigate the effect of nano-roughness also AFM image analysis have been performed (only for 3 μm samples 10 Pa, 20 Pa, 40 Pa and 60 Pa and 15 μm 60 Pa). The results show that by increasing the nano-roughness, the contact angle values increase. This trend is confirmed also by experiments conducted on samples annealed at different temperature: the higher is the grain size the lower is the measured contact angle. However the most important effect on wettability behavior is given by the island organization. For these reason the parameter which better describes the superhydrophobic behavior of surfaces considered in this work is the surface ratio.

Finally some preliminary considerations on the role of multiscale roughness in quasi self-similar surfaces have been proposed, highlighting the necessity of new calculations of surface ratios at different magnification scales in order to properly quantify each singular contribution to surface ratio given

Appendix A

SEM image analysis

Most of the surface analysis have been done by considering SEM images. The images taken by FE-SEM retrieve information, not only about morphology but also about surface ratio and islands area (see Chapter 4). In order to do this, images from top view have been processed. Firstly, the SEM image (1024 × 768 pixels) is converted in a black and white image, as shown in Figure A.1

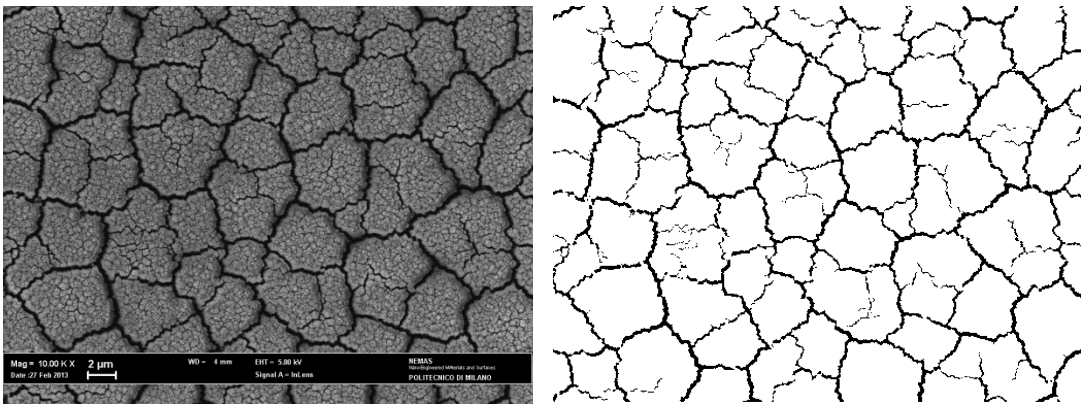

Figure A.1 *(a) SEM image of a TiO2 nanostructured film (b) The same image converted in black and white*

Then, the black and white image is converted in a binary matrix. The island surface to total area ratio is given by dividing the total number of white pixels (elements 1 of the matrix) by the total number of pixels (786432).

Moreover, when the surfaces exhibit a well defined islands with a clear contour (Figure A.2 (a)), image processing get information also about the island area distribution.

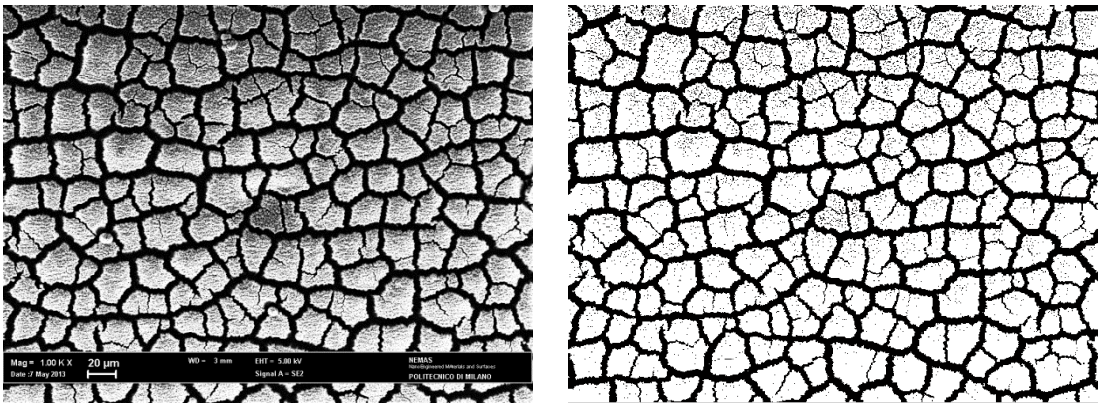

Figure A.2 *(a) SEM image of a TiO2 nanostructured film with clear island (b) The same image converted in black and white*

As shown in Figure A.2(b), sometimes the conversion to black and white set some pixels black even tough they are inside island area. In order to properly include this points in the statistics counting, holes have to be filled, as shown in Figure A.3(a). Finally islands are label and numbered (Figure A.3(b))and statistically analized. In order to properly compare all the samples, all SEM images for analysis have been selected at the same scale magnification (5000x)

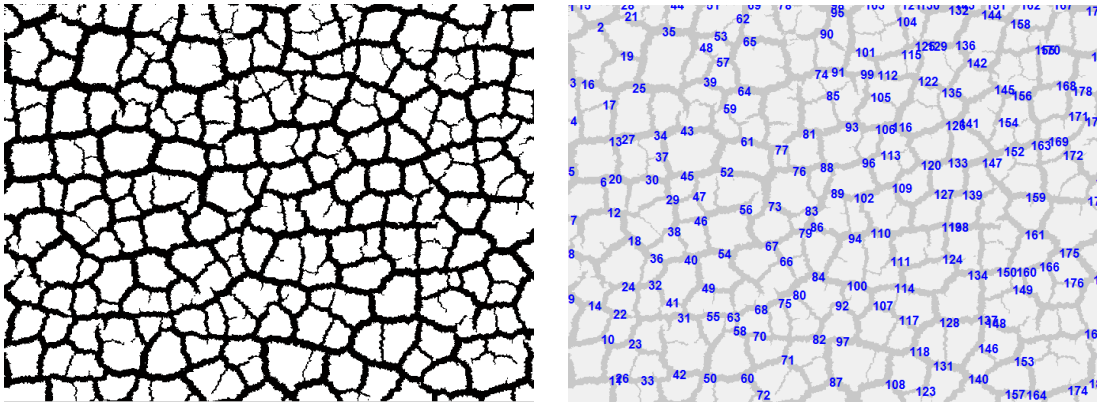

Figure A.3 *(a)SEM image converted in black and white with holes filled (b)Label islands and numbering*

All the calculations have been performed with a code implemented in Matlab® exploiting dedicated functions of Image Analysis Tool Box. The code is here reported:

```
%conversion table sem image mag. to pixelsize%
```

```
%scala 1kx->1pixel=344.83nm=0.34483um/////areatot=93512um^2%
%scala 2.5kx->1pixel=138.88nm=0.13889um/////areatot=15170um^2%
%scala 5kx->1pixel=71.43nm=0.07143um/////areatot=4012um^2%
%scala 10kx-
>1pixel=344.83nm=0.034483um/////areatot=935.12um^2%
%scala 25kx-
>1pixel=13.888nm=0.013889um/////areatot=151.70um^2%
%scala 100kx-
>1pixel=3.4483nm=0.0034483um/////areatot=9.3512um^2%
%scala 200kx->pixel=1.72415nm=
0.00172415um/////areatot=2.33782um^2%

%insert mag sem image%pixel sizeinserisci la dimensione del
pixel%

scale=input('enter mag image:');


if (scale==2500)
    pixelsize=0.13889;
    area_image=15170;
end;
if (scale==25000)
    pixelsize=0.013889;
    area_image=151.70;
end;
if (scale==1000)
    pixelsize=0.34483;
    area_image=93512;
end;
if (scale==10000)
    pixelsize=0.034483;
    area_image=935.12;
end;
if (scale==100000)
    pixelsize=0.0034483;
    area_image=9.3512;
end;
if (scale==200000)
    pixelsize=0.00172415;
    area_image=2.33782;
end;

%insert treshold for minimum dimension area counting%
pixel_threshold=input('enter pixel treshold:');

%insert the image to analyze and convert in pixels matrix%
```

```
a=imread('10_10.jpg');
%conversion to binary matrix%
d=im2bw(a);
figure, imshow(d),title('BW');
%fill the holes in macroregions%
e=imfill(d,'holes');
figure, imshow(e), title('Holes Filled');
%labels each of recognized region%
f=bwlabel(e);
%determine all the properties%
g=regionprops(f,'all');
%gives the properties included in []%
filledarea=[g.FilledArea];
%set the treshold for region elimination%
idx=find((pixel_threshold<=filledarea));
%labels again the macroregion, after new treshold%
h=ismember(f,idx);
figure, imshow(h);
%visualize complete and correct map of recognized region%
vislabels(h),title('Corrected Image')

%properties calculation after error eliminations"
u=regionprops(h,'all');
area=[u.Area];
b_box=[u.BoundingBox];
centr=[u.Centroid];
ecc=[u.Eccentricity];
eq_diameter=[u.EquivDiameter];

% Conversion in terms of pizels sizes%
areapixel=pixelsize^2;
area_um=[u.Area]*areapixel;
eq_diameter_um=[u.EquivDiameter]*pixelsize;



%mean area calculation%
in=numel(area);
amu=sum(area_um)/in;
%mean equivalent diameter calculation%
edmu=sum(eq_diameter_um)/in;
%surface ratio calculation%
phi=sum(area_um)/area_image;
```

Appendix B

AFM image analysis

All the AFM images have been processed and analyzed with the use of Gwyddion [81], an Open Source software for data analysis and visualization.

Since the data obtained from AFM microscopes are very often not leveled at all, before to measure roughness factor, all the images analyzed must be corrected. The simple way for data leveling is to set the set the average height of the data to put the minimum to zero.

Moreover, profiles taken in the fast scanning axis (usually x-axis) can be mutually shifted by some amount or have slightly different slopes. The basic line correction functions deal with this type of discrepancy. For the samples analyzed in this work , a *Match Line Correction* function has been used. This function align rows of the data field to minimize certain line difference function that gives more weight to flat areas and less weight to areas with large slopes.

For all the samples, both *Average Arithmetic Roughness* R_a and *Root Mean Square Roughness* R_q have been measured. The *Average Arithmetic Roughness* R_a is defined as the average deviation of all points roughness profile from a mean line over the evaluation length:

$$R_a = \frac{1}{N} \sum_{j=1}^{N} |r_j| \qquad (2.1)$$

The *Root Mean Square Roughness* R_{rms} is instead defined as the average of the measured height deviations taken within the evaluation length and measured from the mean line:

$$R_{rms} = \sqrt{\frac{1}{N} \sum_{j=1}^{N} r_j^2} \quad (2.2)$$

For statistical measurements, R_q values are the preferred measures. Different surface areas (100×100, 150×150, 200×200, 250×250, 300×300, 350×350, 400×400, 450×450, 500×500, 550×550 and 600×600 nm^2) have been sampled on each sample, in order to find the scales with the lowest standard deviations. Both Average Arithmetic Roughness R_a and the Root Mean Square Roughness R_q have been evaluated as an average of nine measurements carried out on different sample spots.

Bibliography

[1] Y. Y. Yan, N. Gao, and W. Barthlott, "Mimicking natural superhydrophobic surfaces and grasping the wetting process: a review on recent progress in preparing superhydrophobic surfaces.," *Advances in colloid and interface science*, vol. 169, no. 2, pp. 80-105, Dec. 2011.

[2] P. Roach, N. J. Shirtcliffe, and M. I. Newton, "Progess in superhydrophobic surface development," *Soft Matter*, vol. 4, no. 2007, pp. 224-240, 2008.

[3] B. L. Feng et al., "Super-Hydrophobic Surfaces : From Natural to Artificial," *Advanced materials*, vol. 14, no. 24, pp. 1857-1860, 2002.

[4] L. Cao, A. K. Jones, V. K. Sikka, J. Wu, and D. Gao, "Anti-Icing Superhydrophobic Coatings," vol. 25, no. 17, pp. 12444-12448, 2009.

[5] A. J. Meuler, J. D. Smith, K. K. Varanasi, J. M. Mabry, G. H. Mckinley, and R. E. Cohen, "Relationships between Water Wettability and Ice Adhesion," *Applied Materials and Interfaces*, vol. 2, no. 11, 2010.

[6] W. Barthlott, C. Neinhuis, and C. L. Schott, "Purity of the sacred lotus , or escape from contamination in biological surfaces," *Angewandte Botanik*, pp. 1-8, 1997.

[7] Z. Guo and W. Liu, "Biomimic from the superhydrophobic plant leaves in nature: Binary structure and unitary structure," *Plant Science*, vol. 172, no. 6, pp. 1103-1112, Jun. 2007.

[8] H. Rathgen, "Superhydrophobic Surfaces : from Fluid Mechanics to Optics," University Of Twente, 2008.

[9] T. Young, "An Essay on the Cohesion of Fluids," *Phil. Trans. R. Soc.*, p. 95:96, 1805.

[10] R. N. Wenzel, "Surface Roughness and Contact Angle," *The Journal of Physical Chemistry*, vol. 25, p. 400, Jun. 1949.

[11] B. D. Cassie, "Wettability of porous surfaces," *Transactions of the Faraday Society*, vol. 40, pp. 546-551, 1944.

[12] M. Reyssat, J. M. Yeomans, and D. Quéré, "Impalement of fakir drops," *EPL (Europhysics Letters)*, vol. 81, no. 2, p. 26006, Jan. 2008.

[13] M. Callies and D. Quéré, "On water repellency," *Soft Matter*, vol. 1, no. 1, p. 55, 2005.

[14] L. Gao and T. J. McCarthy, "Contact angle hysteresis explained.," *Langmuir : the ACS journal of surfaces and colloids*, vol. 22, no. 14, pp. 6234-7, Jul. 2006.

[15] M. Hikita, K. Tanaka, T. Nakamura, T. Kajiyama, and A. Takahara, "Super-liquid-repellent surfaces prepared by colloidal silica nanoparticles covered with fluoroalkyl groups.," *Langmuir : the ACS journal of surfaces and colloids*, vol. 21, no. 16, pp. 7299-302, Aug. 2005.

[16] V. Bahadur, L. Mishchenko, B. Hatton, J. A. Taylor, J. Aizenberg, and T. Krupenkin, "Predictive Model for Ice Formation on Superhydrophobic Surfaces," pp. 14143-14150, 2011.

[17] K. K. Varanasi, T. Deng, J. D. Smith, M. Hsu, and N. Bhate, "Frost formation and ice adhesion on superhydrophobic surfaces," *Applied Physics Letters*, vol. 97, p. 234102, 2010.

[18] M. Nosonovsky, "Multiscale roughness and stability of superhydrophobic biomimetic interfaces.," *Langmuir : the ACS journal of surfaces and colloids*, vol. 23, no. 6, pp. 3157-61, Mar. 2007.

[19] L. Barbieri, E. Wagner, and P. Hoffmann, "Water wetting transition parameters of perfluorinated substrates with periodically distributed flat-top microscale obstacles.," *Langmuir : the ACS journal of surfaces and colloids*, vol. 23, no. 4, pp. 1723-34, Feb. 2007.

[20] H. Search, C. Journals, A. Contact, M. Iopscience, and I. P. Address, "Roughness-induced non-wetting," vol. 165, 2000.

[21] J. F. Joanny and P. G. de Gennes, "A model for contact angle hysteresis," *The Journal of Chemical Physics*, vol. 81, no. 1, p. 552, 1984.

[22] N. A. Patankar, "On the Modeling of Hydrophobic Contact Angles on Rough Surfaces," *Society*, pp. 1249-1253, 2003.

[23] M. T. Khorasani, H. Mirzadeh, and Z. Kermani, "Wettability of porous polydimethylsiloxane surface: morphology study," *Applied Surface Science*, vol. 242, no. 3-4, pp. 339-345, Apr. 2005.

[24] N. Zhao, Q. Xie, and L. Weng, "Superhydrophobic Surface from Vapor-Induced Phase Separation of Copolymer Micellar Solution," *Society*, vol. 1, pp. 8996-8999, 2005.

[25] G. C. R. M. Ma, Y. Mao, M. Gupta, K.K. Gleason, "Superhydrophobic fabrics produced by electrospinning and chemical vapor deposition," *Macromolecules*, vol. 38, pp. 9742-9748, 2005.

[26] H. Yabu and M. Shimomura, "Single-Step Fabrication of Transparent Superhydrophobic Porous Polymer Films," *Communications*, vol. 11, no. 4, pp. 5231-5234, 2005.

[27] X. Lu, C. Zhang, and Y. Han, "Low-Density Polyethylene Superhydrophobic Surface by Control of Its Crystallization Behavior," *Macromolecular Rapid Communications*, vol. 25, no. 18, pp. 1606-1610, Sep. 2004.

[28] L. Jiang, Y. Zhao, and J. Zhai, "A lotus-leaf-like superhydrophobic surface: a porous microsphere/nanofiber composite film prepared by electrohydrodynamics.," *Angewandte Chemie (International ed. in English)*, vol. 43, no. 33, pp. 4338-41, Aug. 2004.

[29] T. Fabrication and N. Films, "The Fabrication and Switchable Superhydrophobicity of TiO 2 Nanorod Films," pp. 5115-5118, 2005.

[30] X. Feng, L. Feng, M. Jin, J. Zhai, L. Jiang, and D. Zhu, "Reversible Super-hydrophobicity to Super-hydrophilicity Transition of Aligned ZnO Nanorod Films," pp. 62-63, 2004.

[31] and B.-L. S. Zhi-Guang Guo1, Wei-Min Liu2, "A stable lotus-leaf-like water-repellent copper," *Applied Physics Letters*, vol. 92, no. 6, p. 063104, 2008.

[32] J. Wanga, H. Jiangb, Q.Guoc, L. Liud, J. Songe, "High-Temperature Joining of Carbon/Carbon Composites by an Organic Resin Adhesive," *Journal of Adhesion Science and Technology*, vol. 23, pp. 115-123, 2009.

[33] X. J. Feng and L. Jiang, "Design and Creation of Superwetting/Antiwetting Surfaces," *Advanced Materials*, vol. 18, no. 23, pp. 3063-3078, Dec. 2006.

[34] M. Qu, B. Zhang, S. Song, L. Chen, J. Zhang, and X. Cao, "Fabrication of Superhydrophobic Surfaces on Engineering Materials by a Solution-Immersion Process," *Advanced Functional Materials*, vol. 17, no. 4, pp. 593-596, Mar. 2007.

[35] S. Wang, Y. Song, and L. Jiang, "Microscale and nanoscale hierarchical structured mesh films with superhydrophobic and superoleophilic properties induced by long-chain fatty acids," *Nanotechnology*, vol. 18, no. 1, p. 015103, Jan. 2007.

[36] S. A. Kulinich and M. Farzaneh, "How Wetting Hysteresis Influences Ice Adhesion Strength on Superhydrophobic Surfaces," vol. 25, no. 24, pp. 8854-8856, 2009.

[37] G. Palasantzas and J. T. M. de Hosson, "Wetting on rough surfaces," *Acta Materialia*, vol. 49, no. 17, pp. 3533-3538, Oct. 2001.

[38] Y. Li et al., "Two-dimensional hierarchical porous silica film and its tunable superhydrophobicity," *Nanotechnology*, vol. 17, no. 1, pp. 238-243, Jan. 2006.

[39] E. Martines, K. Seunarine, H. Morgan, N. Gadegaard, C. D. W. Wilkinson, and M. O. Riehle, "Superhydrophobicity and Superhydrophilicity of Regular Nanopatterns," *Nano*, vol. 3, no. 1, pp. 1-7, 2005.

[40] Y. F. and X. W. B. Liu, Y. He, "Fabricating Super-Hydrophobic Lotus-Leaf-Like Surfaces through Soft-Lithographic Imprinting," *Macromolecular Rapid Communications*, vol. 27, pp. 1859–1864, 2006.

[41] R. P. Garrod et al., "Mimicking a Stenocara beetle's back for microcondensation using plasmachemical patterned superhydrophobic-superhydrophilic surfaces.," *Langmuir : the ACS journal of surfaces and colloids*, vol. 23, no. 2, pp. 689-93, Jan. 2007.

[42] L. Cao, H.-hua Hu, and D. Gao, "Design and Fabrication of Micro-textures for Inducing a Superhydrophobic Behavior on Hydrophilic Materials," *Society*, no. 8, pp. 4310-4314, 2007.

[43] J. K. W. L. Hench, "The Sol-Gel Process," *Chemical Reviews*, vol. 90, pp. 33-72, 1990.

[44] W. Hou and Q. Wang, "From superhydrophilicity to superhydrophobicity: the wetting behavior of a methylsilicone/phenolic resin/silica composite surface.," *Langmuir : the ACS journal of surfaces and colloids*, vol. 23, no. 19, pp. 9695-8, Sep. 2007.

[45] N. J. Shirtcliffe, G. McHale, M. I. Newton, C. C. Perry, and P. Roach, "Porous materials show superhydrophobic to superhydrophilic switching.," *Chemical communications (Cambridge, England)*, no. 25, pp. 3135-7, Jul. 2005.

[46] F. D. Angelis et al., "Breaking the diffusion limit with super-hydrophobic delivery of molecules to plasmonic nanofocusing SERS structures," vol. 5, no. September, pp. 2-7, 2011.

[47] A. M. Michaels, M. Nirmal, and L. E. Brus, "Surface Enhanced Raman Spectroscopy of Individual Rhodamine 6G Molecules on Large Ag Nanocrystals," *Most*, no. 16, pp. 9932-9939, 1999.

[48] A. . . Smith, H.M. Turner, "Vacuum Deposited Thin Films Using Ruby Laser," *Apllied Optics*, vol. 4, p. 147, 1965.

[49] H. M. Christen and G. Eres, "Recent advances in pulsed-laser deposition of complex oxides," *Materials Science and Technology*, vol. 264005, 2008.

[50] M. Fusi, "Titanium oxide nanostructured surfaces for biotechnology applications," 2009.

[51] A. L. B. M. Fusi, F. Di Fonzo, C.S. Casari, E. Maccalini, T. Caruso, R.G. Agostino, C.E. Bottani, "Island Organization of TiO2 Hierarchical Nanostructures Induced by Surface and Drying," *Langmuir*, vol. 27, pp. 1935-1941, 2011.

[52] R. Mioltello, A. Kelly, *Pulsed Laser Deposition of Thin Film*. Wiley, 1994.

[53] D. B. Geohegan, *Diagnostics and Characteristics of Laser-Produced Plasmas*. New York: Wiley, 1994.

[54] R. B. A. Sambri, S. Amoruso, X. Wang, M. Radovic', F. Miletto Granozio, "Substrate heating influence on plume propagation during pulsed laser deposition of oxidese," *Applied Physics Letters*, vol. 91, p. 151501, 2007.

[55] C. L. C. S. K. Hau, K. H. Wong, P. W. Chan, "Intrinsic resputtering in pulsed-laser deposition of lead-zirconate-titanate thin films," *Applied Physics Letters*, vol. 66, no. 2, p. 245, 1995.

[56] S. Dash, "Characterization of ultrahydrophobic hierarchical surfaces fabricated using a single-step fabrication methodology," *Journal of Micromechanics and Microengineering*, vol. 21, p. 105012, 2011.

[57] X. Zhang, F. Shi, J. Niu, Y. Jiang, and Z. Wang, "Superhydrophobic surfaces: from structural control to functional application," *Journal of Materials Chemistry*, vol. 18, no. 6, p. 621, 2008.

[58] C. F. Q. G. Binning, "Atomic Force Microscope," *Phisical Review Letter*, vol. 56, pp. 930-933, 1986.

[59] B. Cappella and G. Dietler, *Force-distance curves by atomic force microscopy*, vol. 34, no. 1-3. 1999, pp. 1-104.

[60] L. J. S. Wang, L. Feng, "One-Step Solution-Immersion Process for the Fabrication of Stable Bionic Superhydrophobic Surfaces," *Advanced materials*, vol. 18, no. 6, pp. 767-770, 2006.

[61] W. Y. Zhu Y, Hu D, Wan M X, Jiang L, "Conducting and superhydrophobic rambutan-like hollow spheres of polyaniline," *Advanced materials*, vol. 19, pp. 2092-2096, 2007.

[62] E. Bittoun and A. Marmur, "The role of multiscale roughness in the Lotus effect: is it essential for super-hydrophobicity?," *Langmuir : the ACS journal of surfaces and colloids*, vol. 28, no. 39, pp. 13933-42, Oct. 2012.

[63] C. Dorrer and J. Rühe, "Some thoughts on superhydrophobic wetting," *Soft Matter*, vol. 5, no. 1, p. 51, 2009.

[64] G. Camarda, "MICROSCOPIA A FORZA ATOMICA DI FILM NANOSTRUTTURATI PRODOTTI PER ABLAZIONE LASER PULSATA: MORFOLOGIA E REGIMI DI CRESCITA," 2008.

[65] F. D. Fonzo, D. T. A. Li, B. C. S. Casari, M. G. B. C. E. Bottani, D. G. P. Vena, and R. Contro, "Growth regimes in pulsed laser deposition of aluminum oxide films," *Thin Films*, vol. 93, pp. 765-769, 2008.

[66] B. Bhushan and Y. C. Jung, "Natural and biomimetic artificial surfaces for superhydrophobicity, self-cleaning, low adhesion, and drag reduction," *Progress in Materials Science*, vol. 56, no. 1, pp. 1-108, Jan. 2011.

[67] D. Quéré, "Non-sticking drops," *Reports on Progress in Physics*, vol. 68, no. 11, pp. 2495-2532, Nov. 2005.

[68] P. Kim, T.-sing Wong, J. Alvarenga, M. J. Kreder, W. E. Adorno-martinez, and K. I. M. E. T. Al, "Liquid-Infused Nanostructured Surfaces with Extreme Anti-Ice and Anti-Frost Performance," no. 8, pp. 6569-6577, 2012.

[69] X. Hong, X. Gao, and L. Jiang, "Application of superhydrophobic surface with high adhesive force in no lost transport of superparamagnetic microdroplet.," *Journal of the American Chemical Society*, vol. 129, no. 6, pp. 1478-9, Feb. 2007.

[70] W. A. Fox, H. W. Zisman, "The spreading of liquids on low-surface energy surfaces," *Journal of Colloids Science*, vol. 7, pp. 109-121, 1952.

[71] F. M. Fowkes, "Donor-acceptor interactions in Adhesion," *The Journal of Adhesion*, vol. 4, pp. 155-159, 1972.

[72] S. Wu, "Polar and Nonpolar Interactions in Adhesion," *The Journal of Adhesion*, vol. 5, pp. 39-55, 1973.

[73] A. W. Neumann, "A reformulation of the equation of state for interfacial tensions," *Journal of Colloid and Interface Science*, vol. 137, pp. 304-307, 1990.

[74] D. K. Owens, "Estimation of the surface free energy of polymers," *Journal of Applied Polymer Science*, vol. 13, pp. 1741-1747, 1969.

[75] R. K. Wang, K. Günthner, M. Motz, G. Flinn, B. D. Bordia, "Control of Surface Energy of Silicon Oxynitride Films," *Langmuir*, vol. 29, pp. 2889-2896, 2013.

[76] D. H. Kaelble, "Dispersion-Polar Surface Tension Properties of Organic Solids," *The Journal of Adhesion*, vol. 2, pp. 66-81, 1970.

[77] C. R. Wiggins, M. D. Nelson, M. C. Aita, "Crystallization kinetics of rutile formation from amorphous titania films," *THERMODYNAMICS AND KINETICS OF PHASE TRANSFORMATIONS*, vol. 398, pp. 381-386, 1996.

[78] C. R. Wiggins, M. D. Nelson, M. C. Aita, "Phase development in sputter deposited titanium dioxide," *J. Vac. Sci. Technol. A-Vac. Surf. Films*, vol. 14, pp. 772-776, 1996.

[79] B.-B. Wu, F.-M. Pan, and Y.-E. Yang, "Annealing Effect of Pulsed Laser Deposited Transparent Conductive Ta-Doped Titanium Oxide Films," *Chinese Physics Letters*, vol. 28, no. 11, p. 118102, Nov. 2011.

[80] B. W. Koch K. , Bushan B., "Multifunctional surface structures of plants: an important ispiration for biomimetics," *Progress in Materials Science*, vol. 54, pp. 137-138, 2008.

[81] P. Klapetek, D. Neˇ, and C. Anderson, *Gwyddion user guide*. 2004.

List of Figures

Chapter 1

Chapter 2

Chapter 3

Chapter 4

Chapter 5

Appendix A